ETH
Eidgenössische Technische Hochschule Zürich
Swiss Federal Institute of Technology Zurich

Analog Quantum Simulation of Noise Assisted Transport in Light Harvesting Structures with Superconducting Circuits

Master Thesis

Arno Bargerbos

October 6th, 2016

Supervisor: Dr. Anton Potočnik
Group leader: Prof. Dr. Andreas Wallraff
Group: Quantum Device Lab, ETH Zürich

Abstract

Recent theoretical and experimental work has shown that photosynthetic structures exhibit remarkable transport efficiencies, potentially caused by an interplay between quantum effects and a structured noise environment. However, owing to their complex open quantum system dynamics, simulating these structures on a classical computer has proven very demanding. In this thesis we instead study such systems in an analog quantum simulation within the well established superconducting circuit architecture. In this framework we successfully fabricate and characterize a highly tunable three qubit network with a controllable noise environment. This has allowed us to study transport both in the presence of a white and a structured environment, with which we have shown the first experimental realization of noise assisted transport in a system of quantum mechanical elements. Finally, we have performed an experimental investigation into the mechanics underlying the assisted transport through the phonon antenna mechanism, providing further evidence that a structured environment might be a crucial ingredient of nature's efficient light harvesting capabilities.

Acknowledgements

Recent theoretical and experimental work has shown that photosynthetic structures exhibit remarkable transport efficiencies, potentially caused by an interplay between quantum effects and a structured noise environment. However, owing to their complex open quantum system dynamics, simulating these structures on a classical computer has proven very demanding. In this thesis we instead study such systems in an analog quantum simulation within the well established superconducting circuit architecture. In this framework we successfully fabricate and characterize a highly tunable three qubit network with a controllable noise environment. This has allowed us to study transport both in the presence of a white and a structured environment, with which we have shown the first experimental realization of noise assisted transport in a system of quantum mechanical elements. Finally, we have performed an experimental investigation into the mechanics underlying the assisted transport through the phonon antenna mechanism, providing further evidence that a structured environment might be a crucial ingredient of nature's efficient light harvesting capabilities.

Contents

Chapter 1

Introduction

Sunlight is the most abundant form of energy source available on Earth, and it has fueled the planet's biosphere for the vast majority of its evolution [1]. However, since the start of the industrial revolution humankind has differentiated itself from the rest of the ecological system in this regard by switching to other sources of fuel, and as of 2015 solar energy comprised less than 2.1% of the total human energy supply [2]. While these other sources of energy have been successful up to now, forecasts indicate that due to a dwindling fossil fuel supply, the cumulative nature of CO_2 emissions, and an ever increasing energy consumption, solar energy will again have to become a significant fraction of the energy supply during the next century [3]. It is for these reasons that a large body of research is dedicated to improving modern day light harvesting technologies, a significant part of which is the study of photosynthetic organisms, which have been successfully harvesting solar energy for several billions of years [4]. Exhibiting efficiencies surpassing all man made devices, research into their functioning can thus serve as a path to understanding, utilizing and potentially surpassing the capabilities of the organisms found in nature [5].

However, the study of biological systems is highly complex and often impenetrable with rigorous mathematical models [6]. Photosynthesis is no exception to this, with different organisms exhibiting strongly varying light-harvesting systems reflective of their different conditions and habitats [7]. Nevertheless, they all exhibit the same procedure: energy in the form of photons is absorbed by light-harvesting antennas in the form of an electronic excitation, and this excitation is then transported to a reaction center, where a charge separation event transforms it into a more stable form of energy [6]. One of the simplest and most well studied examples of such a light harvesting system is found in green sulfur bacteria, an organism that strictly depends on light as a source of energy [8]. It has a very large antenna complex made out of chlorosomes, allowing them to thrive in low light conditions. The antenna is connected to the reaction center via a specialized structure known as the Fenna-Matthews-Olson (FMO) complex [9].

Given its small size (on the order of several hundred nanometers) and its solubility in water, much research has been done on the structure and properties of FMO. Importantly, it was found to have close to 100% efficiency in transporting excitations from the antenna to the reaction center, despite of an excitation lifetime of less than a nanosecond [10]. This prompted further research into the mechanism underlying the efficient transport, a milestone in which was reached in 2007 when Fleming et al. found evidence for quantum coherences being present during the transport [11]. This kick-started the research of FMO in the context of quantum biology, with the aim of finding out whether the observed quantum effects could contribute to its high transport efficiency.

In order to understand how one can treat FMO in a quantum mechanical framework we first need to take a closer look at its structure. FMO is made up out of a trimer of negligibly coupled complexes, each consisting of eight bacteriochlorophyll molecules often referred to as pigments. These pigments are bound to a protein backbone, forming the noisy environment of the pigments as well as creating their energy landscape [12]. Excitations typically enter a single pigment via the antenna complex and are then transferred via the other pigments until they reach the reaction center. This structure is illustrated in figure 1.1, where the colors of the antenna and the reaction center show the analogy with FMO being a wire connecting an anode and a cathode.

The basic structure already provides a naive picture of how quantum coherences could contribute to the efficiency of FMO: instead of the excitation transferring from pigment to pigment sequentially, one could instead imagine that the wave function of the excitation enters a superposition of multiple pigments combined in order to traverse several paths at once, finding the shortest route from antenna to reaction center. While at first sight the notion of such quantum coherences occuring at room temperature is quite surprising, comparison of the relevant energy scales in FMO indicate that quantum effects could in fact have a relevant impact on the system [16].

A more rigorous theoretical treatment of FMO in the context of quantum mechanics can be found in two seminal works by Plenio & Huelga and Mohseni et al respectively [17, 18], where the FMO complex is considered as a quantum network of sites that can either have zero or one excitations present. Each of the sites is thus equivalent to a two level system, such as a spin-1/2 particle or a generic qubit. As described by Caruso et al [10], such a system can indeed lead to the delocalized transport behaviour hinted at above.

However, this picture does not touch upon one of the most crucial elements

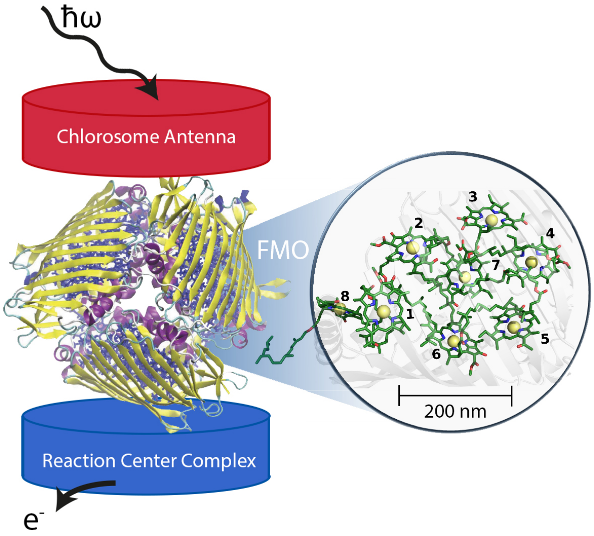

Figure 1.1: An illustration of the light-harvesting structure of green sulfur bacteria, consisting out of an antenna connected to a reaction center via the FMO complex. The FMO complex itself has a trimeric structure, of which each unit consists of 8 pigments held in place by a portein backbone. Image adapted from [13, 14, 15].

of the system: the environment of the pigments. Governed by the protein backbone of the FMO complex itself, it is thought that the surroundings of the pigments take the form of a strongly coupled vibrational environment of phononic modes [12]. The standard picture of quantum mechanics is that the fluctuations originating from this environment would cause any coherences present in the system to rapidly decay, resulting again in a system where excitations incoherently hop from pigment to pigment sequentially. Yet absorption and fluorescence measurements have shown that the fluctuations of the protein environment have significant structure, potentially promoting long lived coherences instead of destroying them [19]. This structured noise environment provides another obstacle for the study of FMO, as modeling an open quantum system of many interacting degrees of freedom is one of the main challenges in modern physics and chemistry [20]. Limited by exponentially increasing amounts of resources required, classical computational methods have not been able to provide solutions to these questions, and while universal quantum computers are conjectured to offer improvements in this area, they are not available yet.

Mostame *et al.* have instead proposed the design of an analog quantum simulator tailored to the model of interest, in which one can physically engineer the environment of the open system that is so challenging to study with classical computational methods [20]. More specifically they propose to build an FMO type structure using the superconducting circuit architecture, which can then be studied in a laboratory setting. The system studied in this thesis is a variant of the proposed simulator, in which we study the dynamics of energy transport in a network of transmon two level systems in the presence of an engineered noise environment.

1.1 Analog Quantum Simulation of FMO

In order to set up the system studied in this thesis we start from the proposal by Mostame *et al.* and indicate how our system deviates from this, highlighting the differences in implementation. They begin from a generic Hamiltonian governing the FMO network, given by

$$\hat{\mathcal{H}}_{Tot} = \hat{\mathcal{H}}_S + \hat{\mathcal{H}}_B + \hat{\mathcal{H}}_{S-B} \tag{1.1}$$

where $\hat{\mathcal{H}}_S$ is the Hamiltonian of the network of 8 coupled sites, $\hat{\mathcal{H}}_B$ is the Hamiltonian of the environmental bath created by the surrounding protein structure, and $\hat{\mathcal{H}}_{S-B}$ governs the interaction between these two systems. In line with the work of Plenio & Huelga and Mohseni, the Hamiltonian of a network of N FMO sites is given by [17, 18]

$$\hat{\mathcal{H}}_S = \frac{1}{2}\sum_{j=1}^{N}\left[\varepsilon_j \hat{\sigma}_{z,j} + \sum_{k>j} V_{jk}\left(\hat{\sigma}_j^{+}\hat{\sigma}_k + \hat{\sigma}_k^{+}\hat{\sigma}_j\right)\right] \tag{1.2}$$

where $\hat{\sigma}_{z,j}$ is the Pauli z operator of site j and $\hat{\sigma}_j^{+,-}$ creates or annihilates an excitation at site j. It describes a system of sites of energy ε_j through which excitations can travel via the (transition-dipole-dipole) couplings V_{jk}. Important is to note that the parameters of this Hamiltonian should be chosen in accordance with what is observed in FMO, where one finds that the sites form a ladder of energy levels decreasing from the site at which the excitation arrives from the antenna complex to where it leaves to the reaction center. There are thus significant energy mismatches $\Delta_{jk} = |\varepsilon_j - \varepsilon_k|$ between the sites where typically $\Delta_{jk} \geq V_{jk}$, suppressing coherent transport from site to site.

Mostame *et al.* propose to recreate this site Hamiltonian through a system of eight coupled superconducting flux qubits [21], the transition frequencies and couplings of which are determined in accordance with a mapping from experimentally determined FMO parameters to the superconducting circuit regime. It is this feature that highlights the power of the superconducting architecture, as it offers tremendous control over the fundamental system parameters such as the coupling rates, the energetic disorder, and the in and output coupling, a luxury not present in most other architectures. The proposed topology of the network is shown in in figure 1.2 where (in line with what is known about FMO) excitations enter the system at site eight (shown in green), from which they can then propagate through the coupled network and leave into the reaction center (the sink) at site 3 (shown in orange).

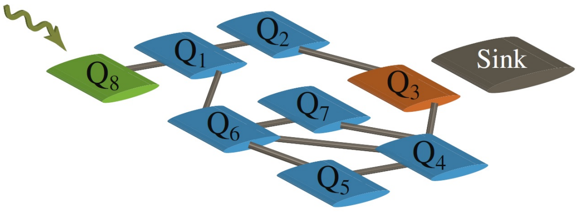

Figure 1.2: An illustration of the proposed network topology of the analog quantum simulator of FMO, where the site labels numbering is based on historic reasons. Image taken from [20].

In this thesis we choose not to work with flux qubits but with transmon qubits instead, which are extensively discussed in the next chapter. More importantly, we also choose not to look at the full system of eight coupled sites. While fabricating such a system should be possible in the near future, the experimental complications that come with the full characterization and control of eight qubits have motivated us to start our research in a reduced topology. In this thesis we therefore treat a system of three coupled transmon qubit, in which we can study the simplest toy model of an FMO type structure consisting of only two sites and its more complex variant of three sites.

We now move on to the description of the bath. Due to the vibrational nature of the protein environment, the bath $\hat{\mathcal{H}}_B$ is often described as being phononic: it consists of a network of displaced harmonic oscillators. Moreover, contrary to what one might expect due to the small dimensions of the system, research has shown that the bath of each site is largely uncorrelated with respect to other sites; each effectively has its own bath [22]. The Hamiltonian of the bath is therefore given by

$$\hat{\mathcal{H}}_B = \sum_{j=i}^{N} \hat{\mathcal{H}}_B^j = \sum_{j=i}^{N} \sum_{l} \hbar \omega_l^j \left(\hat{a}_l^{\dagger,j} + \hat{a}_l^j + 1/2 \right) \tag{1.3}$$

which takes the form of a generic harmonic oscillator Hamiltonian of size l, with ω_l^j being the frequency of the lth phonon coupled to site j and $\hat{a}_l^{\dagger,j}$ the creation operator of phonons in the lth bath mode of site j. Mostame *et al.* propose to create such a bath by connecting each site to a collection of damped quantum LC resonators, the implementation of which in the context of this thesis we will comment on shortly.

First we introduce the interaction between the bath and the sites themselves, which is often described by a linear coupling between the bath and the system. This is known as the perturbative coupling approximation or the Born approximation, the validity of which has been thoroughly researched in the context of FMO [6]. It results in an interaction term governed by the Hamiltonian

$$\hat{\mathcal{H}}_{S-B} = \sum_{j=1}^{N} H^{j}_{S-B} = \sum_{j=1}^{N} \hat{\sigma}_{z,j} \left[\sum_{l} \chi_{jl} \left(\hat{a}^{\dagger,j}_{l} + \hat{a}^{j}_{l} \right) \right] \tag{1.4}$$

where $\chi_{jl} = \hbar\omega^{j}_{l} d_{jl}$ is the coupling between the jth site and the lth phonon and d_{jl} is the dimensionless displacement between the minima of the ground and excitated state potentials of the lth phonon mode at site j. Note that the reorganization energy $\lambda_j = \sum_l \hbar\omega^{j}_{l} d^{2}_{jl}/2$ was implicitly included in the system Hamiltonian by defining $\varepsilon_j = \varepsilon_j + \lambda_j$ with ε_j being the true transition energy of site j in the absence of a bath [20].

Combining all of the above, $\hat{\mathcal{H}}_{Tot}$ is described by the well known independent boson model [23]. Following Mostame *et al.* we can write it in the site energy basis defined by $\hat{\mathcal{H}}_S |S\rangle = E_S |S\rangle$ and find that

$$\hat{\mathcal{H}}_{Tot} = \sum_{S} E_S |S\rangle \langle S| + \sum_{S,T,l} |S\rangle \langle T| K^{jl}_{ST} \left(\hat{a}^{\dagger,j}_{l} + \hat{a}^{j}_{l} \right) + \hat{\mathcal{H}}_B \tag{1.5}$$

where $K^{jl}_{ST} = \langle J| \, |S\rangle] \, \langle J| \, |T\rangle \, \chi_{jl}$. By writing the equation in this form we see that the system-bath coupling is off-diagonal and can thus lead to transitions between the sites.

However, the bath and its coupling to the sites studied in this thesis marks a significant departure from the proposal. This is due to experimental considerations: as written above Mostame *et al.* propose to couple each of the sites to a series of dampened quantum LC resonators, going as far as coupling each individual qubit to up to 15 different LC resonators with frequencies in the range of 100 MHz to 3 GHz in order to replicate the full FMO bath. While in principle the fabrication of such resonators is well developed in this research group [24], fabricating such an array of resonators is currently not technologically feasible due to the physical size they would take up on the chip.

An alternative to the above would be using a reduced number of resonators, leading to a reduction in the structure of the environment. Instead of doing so we choose to study the system in what is known as the classical noise approximation, where the quantum environment is replaced by time-dependent fluctuations of transition energies: this is known as the Haken-Strobl-Reineker (HSR) model [25]. In this model $\hat{\mathcal{H}}_{Tot}$ is replaced by the time dependent Hamiltonian

$$\hat{\mathcal{H}}(t) = \frac{1}{2}\sum_{j=1}^{N}\left[\left(\varepsilon_j + \delta\varepsilon_j(t)\right)\hat{\sigma}_{z,j} + \sum_{k>j} V_{jk}\left(\hat{\sigma}_j^{+}\hat{\sigma}_k + \hat{\sigma}_k^{+}\hat{\sigma}_j\right)\right] \tag{1.6}$$

where all of the bath dynamics are now contained in the (classical) fluctuating transition energy term $\delta\varepsilon_j(t)$. At first sight this Hamiltonian appears to contain much less structure than the originally proposed variant with the quantum bath. However, as we explicitly derive in appendix A the two can be made equivalent in the high temperature limit $n(\omega) \gg 1$ by choice of the proper time varying signal governing $\delta\varepsilon_j(t)$. Here $n(\omega)$ is the Bose-Einstein distribution defined in appendix A and for the FMO parameters listed in the proposal by Mostame *et al.* we find that $n(\omega) \approx 7$ for the relevant phononic frequencies at 300 K. This shows that the classical noise approximation can be used to gain significant insight into the physics governing FMO without the explicit need for a quantum bath [22, 26].

With this we have described the basics of the system studied in this thesis: we look at a system of three coupled two level systems in the presence of a noise environment contained in site dependent fluctuating transition energies. We then study how well energy is transported through the system as a function of the power of the noise environment. However, two crucial ingredients are missing at this stage: the FMO complex serves to transfer excitations from an antenna complex to a reaction center. As introduced in the next chapter, the role of the antenna will be played by a transmission line through which we can drive the system with a coherent microwave signal, and the reaction center will be mimicked with a resonator into which one of the sites can decay.

1.2 Theoretical Expectations

Before we begin a rigorous treatment of the elements used in our system in the next chapter, we first treat what is expected from the two and three site networks based on theory. The transport of excitations in the two site model in the presence of a classical memoryless (white noise) bath $\delta\varepsilon_j(t)$ is discussed in work by Rebentrost *et al.* [27], where they illustrate a simple example of noise assisted transport.

They begin by treating the system of two sites $|1\rangle$ and $|2\rangle$ that can each host only a signle excitation with the Hamiltonian

$$\hat{\mathcal{H}} = \frac{\Delta}{2}\left(|1\rangle\langle 1| - |2\rangle\langle 2|\right) + V/2\left(|1\rangle\langle 2| + |2\rangle\langle 1|\right) \tag{1.7}$$

where Δ is the energy mismatch between the sites and V is the coupling strength. In the absence of a noise environment such a system evolves coherently: starting from an excitation at site one, one can treat the system on the

Bloch sphere as rotating about the z-axis by an angle $\theta = \sin^{-1}\left(\frac{V}{\hbar\Omega}\right)$ where $\hbar\Omega = \sqrt{\Delta^2 + V^2}$ is the well known Larmor frequency. Given the above, the maximum probability of finding the excitation initially located at site 1 at site 2 is given by $\sin^2(2\theta)$ while the average probability is $\sin^2(\theta)$; one finds that for $\Delta \gg V$ the excitation remains localized at site 1. In the literature this vanishing-to-weak noise regime is therefore known as the quantum localization regime. Its analysis can be be generalized to a system of many energy mismatched sites such as FMO, where the general picture is that an excitation starting from an initial site evolves into a superposition of energy eigenstates with a vanishing overlap of the excitation being at other sites; in the absence of noise such a network thus has a low transport efficiency.

One then introduces the noise environment. As derived in appendix A, for white noise such an environment can be fully characterized by a Lindblad master equation containing a pure dephasing rate γ_ϕ, which we will here assume to be equal for sites 1 and 2. In this scenario the system obeys the well known optical Bloch equations [28], from which one finds that instead of remaining localized at site 1 the excitation now gradually diffuses over the two sites, ending up in a fully mixed state with a 50% chance of being found at either site. This diffusion process can be thought of as a random walk on the Bloch sphere with a step size equal to θ taken every γ_ϕ^{-1}; the system must thus perform approximately $\left(\frac{\pi}{\theta}\right)^2 \frac{1}{\gamma_\phi}$ steps to reach the final mixed state. This is one of the simplest instances of environment-assisted quantum transport (ENAQT), as the system has gone from a quantum localization regime to a state in which site 2 can now be reached with the assistance of the noise environment. While for a system with more than two sites the analysis is more complicated, the general picture should still hold. One can think about this in terms of interferences: in the quantum regime, the paths leading from the initial site to the target site destructively interfere. When the noise causes the coherences of the system to decay so does the destructive interference, lifting the localization and allowing for an increased transport to the target site.

However, this analysis no longer holds in the limit of strong noise and large dephasing rates. When $\gamma_\phi > \Delta$ the angle the system precesses before being fully decohered is approximately given by $\phi = \frac{\Delta}{\gamma_\phi}$, and the probability of remaining at site 1 is thus given by $\cos^2(\phi) \approx 1 - \left(\frac{\Delta}{\gamma_\phi}\right)^2$. The system thus essentially performs a biased random walk of step size ϕ with an average step time $\frac{\gamma_\phi}{\Delta^2}$, and in a time t the the system diffuses by an angle $\Delta^2 t^{1/2} \gamma_\phi^{-3/2}$; this is derived in [27]. While such a system will still converge to the aforementioned mixed state, it will do so in a much longer and ultimately irrelevant timescale as the transport rate is suppressed by a polynomial in γ_ϕ. While again more complicated, this analysis is also expected to hold for larger systems. In the literature it is described using the quantum Zeno effect (QZE): a high dephasing rate γ_ϕ is equivalent to the excitation continuously being measure in the site basis, freezing its evolution and trapping the excitation at its initial site. This then suppresses any transport away from the initial site.

Figure 1.3 illustrates the three phases of quantum localization, noise asissted transport, and the quantum Zeno effect for a classical and digital simulation of FMO in the presence of a classical white noise bath [27]. We observe the suggested initial increase in efficiency (here defined as the number of excitations that leave the system via the sink per unit time) with increasing noise powers attributed to the lifting of quantum localization, where it can be seen to reach a maximum and then decrease in accordance with the QZE effect. Note that in this plot γ_ϕ is in units of inverse wavelength, which can be thought of as a frequency.

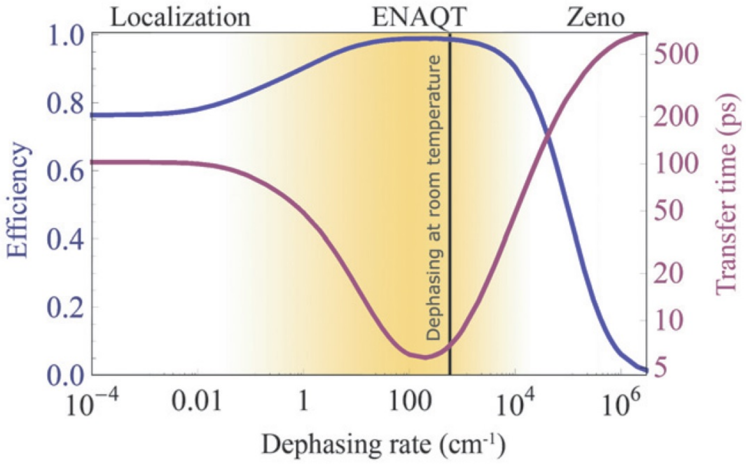

Figure 1.3: The efficiency (blue) and transfer time (red) as a function of dephasing rate γ_ϕ as simulated for the FMO complex in the presence of a white noise bath. The three dephasing regimes can be observed, being the initial quantum localization, environment-assisted quantum transport, and the quantum Zeno effect. Picture taken from [27].

While the above scenario of a white bath will be the starting point for studying FMO type structures in the presence of noise in this thesis, it fully neglects the structure of the bath. Yet as previously discussed it is exactly this structure that is thought to be crucial for the long lived coherences observed in FMO [19]. It is for this reason that we also study the system in the presence of a more structured environment, in the form of noise with Lorentzian power spectral densities with a variable center frequency and amplitude. This is based on a concept known as the phonon antenna mechanism [29, 30]: given that the environment of an FMO-type system has an environmental spectral density that is peaked around certain frequencies, it is hypothesized that the system sets up its energy mismatches to coincide with these peaks, making use of otherwise detrimental noise and thereby optimizing transport between the sites. The split site energy levels thus effectively act as an antenna for the environmental modes, leading to another instance of noise assisted transport.

Although such a mechanism has been proposed to be related to biological olfactory processes [30], it also has significant applications to FMO: the phononic modes of the protein environment lead exactly to such peaked power spectral densities. This is illustrated by figure 1.4, which depicts the experimentally determined power spectral density of the FMO environment [20, 19]. Note that this power spectral density is largely fixed by factors such as temperature, while recent research indicates that the structure of the protein helices encapsulating the pigments can effectively be used to tune their relative energy mismatches [12]. This has led researchers to believe that the structure of FMO has evolved into its current form of mismatched sites in order to make optimal use of the environmental noise available, maximizing its transport efficiency [12].

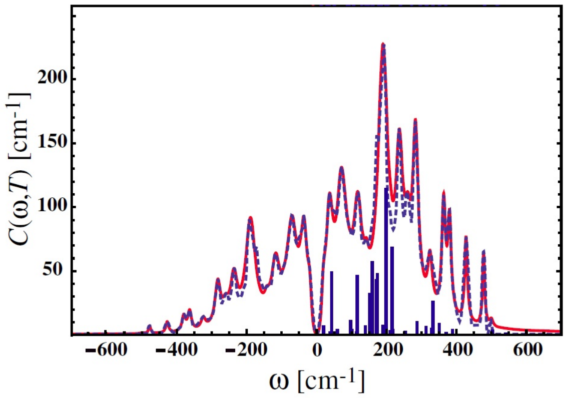

Figure 1.4: The temperature-dependent power spectral density as experimentally observed for FMO at 77 K. The blue bars indicate the energy mismatches of the FMO complex. Note that the dashed blue lines indicate the actual observed PSD, while the red lines indicate the spectrum obtained if one were to pursue the proposal of Mostame et al. by coupling the pigment network to LC resonators. Figure taken from [20].

While the previously discussed white noise bath is readily described with a master equation in Lindblad form and a pure dephasing rate γ_ϕ, the scenario of the phonon antenna is already more challenging to treat theoretically as one can no longer assume the bath to be memoryless. Some of its properties can still be characterized within a modified Redfield approach; the interested reader is referred to the supplementary information of [30] as its treatment is beyond the scope of this thesis. However, this scenario is readily realised in the system studied in this thesis: we will therefore thoroughly investigate its dynamics in both the two and three site setup in order to experimentally verify its role in noise assisted transport.

1.3 Previous Experimental Efforts

Up to this stage all of the discussed models were purely theoretical, in addition to a proposed experimental setup. However at this time, to our best knowledge, four experimental verifications of noise assisted transport in an FMO-type network exist, all of which were done in a fully classical system. We will discuss two of these; the other two can be found in [31, 32].

The first experiment we discuss is by Biggerstaff et al (cite), in which they used a network of four coupled laser-written waveguides to create a four site network Hamiltonian. They used broadbanding of the input illumination as a source of controllable dephasing by averaging over the result from an array illuminated at many different wavelengths. Although each individual wavelength propagates through the system coherently, the dephasing is achieved by using a single intensity measurement at the output that does not resolve wavelength, effectively seen as dephasing by a memoryless bath. In this system they observed an increased transport efficiency compared to the case of narrowband illumination, indicative of the phase between quantum localization and noise assisted transport. However, in this experiment no maximum efficiency was reached and the subsequent quantum Zeno phase was thus not observed, as only moderate dephasing rates could be achieved.

The second experimental work is by Viciani *et al.* [33], in which they mimicked a four site network using a Mach-Zehnder type setup with an optical cavity placed in each of its two arms combined with two fiber optic couplers, coupling laser light into and out of the system. These couplers thus effectively serve as the sites located next to the antenna and the reaction center respectively. The environment is then simulated by tuning the cavity frequency mismatch $\Delta = |\omega_1 - \omega_2|$. Starting from $\Delta = 0$ as a zero noise environment, they then measured the transmission of the system for a set of different mismatches which can be related to static and dynamic disorder in the system. The latter can then be related to an effective dephasing rate. In this experiment all three phases of the transport efficiency were observed, with an initial increase from the quantum localization regime to a maximum at moderate dephasing rates, before observing a decreased efficiency at even higher dephasing rates due to the quantum Zeno effect.

While the above two experiments have shown behaviour in line with what is expected from theory, they have done so in a completely classical setting. This meant that they were impervious to mechanics such as lifetime effects of the to be simulated excitations, along with other properties associated with two level systems such as photon blockade, related to how each site can only host one excitation at a time. In addition to this the classical systems are fundamentally incapable of hosting the quantum coherences observed in FMO, and its potential effect is thus not present. The system studied in this thesis aims to improve on this by offering the first experimental realization of noise assisted transport in a fully quantum mechanical architecture, intrinsically including lifetime effects, superpositions and potential coherent transport, creating a closer analogue to the true FMO complex found in nature.

In addition to the above the superconducting architecture offers tremendous control over the fundamental system parameters such as the coupling rates, the energetic disorder, the input and output coupling and the driving rate of the system, allowing us to create a system with properties closer to FMO than feasible in the two classical scenarios. In contrast to the waveguide experiment we can also generate noise environments with amplitudes that can be varied over orders of magnitude, allowing us to investigate all stages of noise assisted transport. Moreover, we are able to do this with effectively arbitrary noise power spectral densities, allowing us to investigate the potential effect of a structured environment completely absent in the previous experimental realizations. Finally, while not performed in the context of this thesis, our architecture also readily allows for a number of follow up experiments that are much more difficult to perform in a classical setting such as recreating the ultra low light environments of the green sulfur bacteria with single photon excitations and studying the effect of variable input photon statistics such as incoherent light.

Chapter 2

Theory of the Superconducting Architecture

As introduced in the previous chapter, the goal of this thesis is to perform an analog quantum simulation of a light harvesting structure in the presence of noise using the superconducting circuits architecture. More specifically, we aim to do so using a system of coplanar waveguides and transmon qubits subjected to an artifically generated noise environment. In this chapter we will first introduce the theory governing each of these circuit elements on their own, before combining all of them into a single system and studying their interactions.

2.1 Transmon Qubits

As discussed in chapter 1, our choice of two level system used to model the sites of the FMO-type complex is the superconducting transmon qubit. Being the fundamental building block of our system, it is a natural starting point for our theoretical treatment.

The transmon is often referred to as an artifical atom. However, at first sight it does not resemble the atoms found in nature; it is an electrical circuit consisting of countless atoms that only functions properly at cryogenic temperatures. The comparison is derived from an important shared property: their anharmonic energy spectrum. Denoting that the energy spacing between different levels of the system are not equal, such anharmonicity is found in every atom. An example of this is the famous spectrum of the hydrogen atom

$$E_n = -\frac{e^4 m_e}{32\pi^2 \varepsilon_0^2 \hbar^2}\left(\frac{1}{n^2}\right) \tag{2.1}$$

where n denotes the principal quantum number, m_e is the electron mass, e is the elementary charge, ε_0 is the electric permitivity of free space and $\hbar$

is the reduced Planck constant [34]. Due to the $1/n^2$ dependence on the principal quantum number, the spacing between adjacent energy levels of the hydrogen atom is not a constant but a function of the levels themselves; the spectrum is thus anharmonic. In this section we will show that the energy level spacing of the transmons shares this property, hence justifying its classification as artifical atom. Note that such anharmonicity is essential in order for the transmon to be used as a two level system; if the spectrum was harmonic one could not drive transitions between a specific pair of levels and one would not have a qubit.

2.1.1 LC Circuits

Curiously enough, we begin our description of the transmon from a system with exactly such a harmonic spectrum: the LC circuit. The most elementary circuit the transmon is related to, the LC circuit consists of a capacitor with capacitance C and an inductor with inductance L connected in series as shown in figure 2.1. One can show that it has the ability to store electrostatic energy in the capacitor given by $\frac{CV^2}{2}$ where V is the voltage, and magnetic energy in the inductor given by $\frac{LI^2}{2}$ where I is the current. Moreover, one can use Kirchhoff's current and voltage laws and the constitutive relations of the individual elements to show that $V = \frac{Q}{C} = -L\dot{\Phi}$ where Q is the charge across the capacitor and Φ is the magnetic flux in the inductor, offering an alternative basis of coordinates to describe the system. Regardless of the choice of coordinates, one can show that the energy stored in the circuit is then converted between the two elements in an oscillatory fashion with frequency $\omega_0 = \frac{1}{\sqrt{LC}}$; it is a harmonic oscillator, just like the mass-spring system [35].

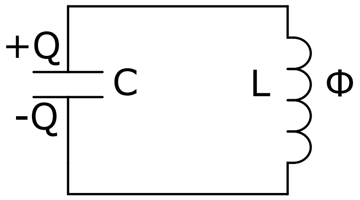

Figure 2.1: The LC circuit with capacitance C, inductance L, charge Q and flux Φ.

The above describes the circuit in terms of classical physics as known from Maxwell's equations. We now depart from this picture and describe the system in the context of circuit quantum electrodynamics (circuit QED), where we can treat the system in terms of single excitations. To do so we start from the Lagrangian of the system. The Lagrangian in terms of the flux is given by

$$\mathcal{L} = \frac{C\dot{\Phi}^2}{2} - \frac{\Phi^2}{2L} \tag{2.2}$$

in accordance with the kinetic and potential energy of the system. Defining the canonical conjugate momentum $\frac{\partial \mathcal{L}}{\partial \dot{\Phi}} = C\dot{\Phi} = Q$, we can use a Legendre transformation $\mathcal{H} = \dot{\Phi}Q - \mathcal{L}$ to write the Hamiltonian

$$\mathcal{H} = \frac{Q^2}{2C} + \frac{\Phi^2}{2L} \tag{2.3}$$

which is in line with the energies referenced above. In the next step we elevate the charge and flux coordinates to quantum mechanical operators by enforcing the canonical commutation relation $\left[\hat{Q}, \hat{\Phi}\right] = -i\hbar$, allowing us to introduce the creation and annihilation operators of the second quantization formalism

$$\hat{a}^\dagger = \frac{1}{\sqrt{2\hbar Z_C}} \left(Z_C \hat{Q}^\dagger - i\hat{\Phi}^\dagger \right) \tag{2.4}$$

$$\hat{a} = \frac{1}{\sqrt{2\hbar Z_C}} \left(Z_C \hat{Q} + i\hat{\Phi} \right) \tag{2.5}$$

where $Z_C = \sqrt{\frac{L}{C}}$ is the characteristic impedance of the LC circuit and where $\left[\hat{a}, \hat{a}^\dagger\right] = 1$ [35]. With the above, one can write the Hamiltonian of the circuit as

$$\hat{\mathcal{H}} = \hbar\omega_0 \left(\hat{a}^\dagger \hat{a} + \frac{1}{2} \right) \tag{2.6}$$

where once again $\omega_0 = \frac{1}{\sqrt{LC}}$. Studying the system in the Fock (number) basis, one finds that $\hat{\mathcal{H}} \left|n\right\rangle = \hbar\omega_0 n \left|n\right\rangle = E_n \left|n\right\rangle$: the energy of the n-excitation state is linearly proportional to the number of excitations, and the separation between the different energy levels is constant. The spectrum of the quantum mechanical LC oscillator is therefore harmonic [35].

2.1.2 Nonlinear Circuits

As written above the transmon has an anharmonic spectrum, as opposed to the LC circuit. In order to depart from the harmonic spectrum we therefore introduce a nonlinear element to the circuit: the Josephson junction. A nonlinear, dissipationless inductive element, the Josephson junction consists of two superconducting layers separated by a weak link such as a thin insulating barrier [36]; chapter 3 contains more details on the fabrication process itself. Predicted in 1962 by David Josephson [37], the behaviour of the junction is governed by two important equations: the Josephson DC and AC relations

$$\hat{I} = I_0 \sin \hat{\delta} \tag{2.7}$$

$$\hat{V} = \frac{\Phi_0}{2\pi}\dot{\hat{\delta}} \tag{2.8}$$

where I_0 is the temperature and material dependent critical current of the junction, $\hat{\delta}$ is the quantized phase difference of the order parameter on each side of the junction [**?**], and $\Phi_0 = \frac{h}{2e}$ is the magnetic flux quantum. Relating this to the relationship between the current and the voltage across an inductor $V = -L\dot{I}$ one finds that

$$V = \frac{\Phi_0}{2\pi I_0}\frac{1}{\cos\hat{\delta}}\dot{I} = L_{J0}\frac{1}{\cos\hat{\delta}}\dot{I} \tag{2.9}$$

The Josephson junction thus has an effective nonlinear inductance, where $L_{J0} = \frac{\Phi_0}{2\pi I_0}$ is essentially fixed after fabrication. As with a linear inductor, one can describe the energy stored in the junction as

$$E_{Josephson} = \int dtVI = \int dt\frac{\Phi_0}{2\pi}\dot{\hat{\delta}}I_0\sin\hat{\delta} = -E_J\cos\hat{\delta} \tag{2.10}$$

with $E_J = \frac{\Phi_0 I_0}{2\pi}$ being the maximal energy stored in the junction.

One can then envision replacing the inductor of the LC circuit of figure 2.1 with such a Josephson junction. The cooper pair box (CPB) is such a circuit; it is the textbook example of an anharmonic system based on superconducting circuits. In figure 2.2 we show its slightly more complex relative in black: the split cooper pair box. It has not one but two Josephson junctions connected in parallel (denoted by crossed boxes), known as a superconducting quantum interference device (SQUID). It can be shown that the SQUID obeys the same relationships as the Josephson junction with the substitution $I_0 \rightarrow 2I_0|\cos\left(\pi\frac{\Phi}{\Phi_0}\right)|$; it acts as a Josephson junction with a critical current tunable by an external magnetic flux Φ [38]. From here on out we therefore write E_J as $E_J(\Phi)$ to denote that the system contains a SQUID instead of a single junction.

Returning to the split CPB containing a SQUID, its Hamiltonian is analogous to that of the LC circuit [35]:

$$\mathcal{H} = \frac{Q^2}{2C_\Sigma} - E_J(\Phi)\cos\delta \tag{2.11}$$

where $C_\Sigma = C_G + 2C_J$ as the junctions also have some relatively small capacitance C_J. While such a Hamiltonian contains the physics of the system in a rather general form, one can go into more detail as discussed in [35].

As illustrated in figure 2.2 the split CPB essentially consists of a superconducting island of $N = \frac{Q}{2e}$ Cooper pairs connected to a reservoir via the SQUID, as well as to a capacitance to ground C_G. If one then connects the circuit to a voltage source V (shown in gray in figure 2.2) one can effectively

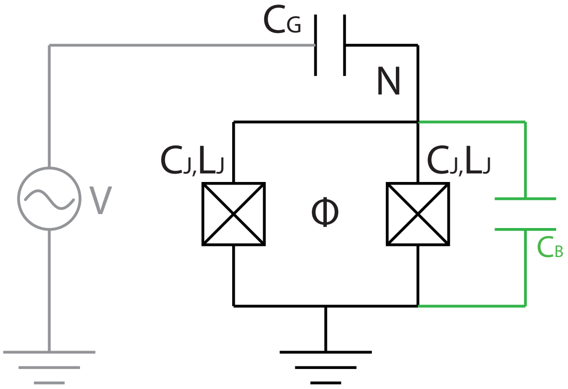

Figure 2.2: The cooper pair box (black) and transmon (black and green) circuits of N Cooper pairs containing two identical Josephson junctions of capacitance C_J and effective inductance L_J capacitively coupled to a a voltage source V (gray) with capacitance C_G in the presence of an external magnetic flux Φ. The transmon circuit contains an additional capacitance C_B.

tune the charge of the split CPB by changing the number of Cooper pairs on the island: the charge is then given by $Q^2 = (2e(N - n_g))^2$, where $n_g = \frac{C_G V_G}{2e}$ is the polarization charge on the capacitor C_G . Note that n_g is continuous, in contrast to N. As the number of cooper pairs is quantized, one can elevate it to a quantum operator such that the Hamiltonian of the split CPB is then given by

$$\hat{\mathcal{H}} = 4E_C(\hat{N} - n_g)^2 - E_J(\Phi)\cos\hat{\delta} \tag{2.12}$$

where $E_C = \frac{e^2}{2C_\Sigma}$ is known as the charging energy. In this basis the Hamiltonian does not have an exact solution; one has to truncate the phase up to a certain amount of Cooper pairs N and use numerical methods to solve for the energy level structure. However, as the number of Cooper pairs $\hat{N}$ and the phase $\hat{\delta}$ are conjugate variables ($\left[\hat{\delta}, \hat{N}\right] = i$) the above Hamiltonian can thus also be written in the phase basis, where it takes the form

$$\hat{\mathcal{H}} = E_C\left(-i\frac{\partial}{\partial\hat{\delta}} - n_g\right)^2 - E_J(\Phi)\cos\hat{\delta} \tag{2.13}$$

In this basis one can solve for the energy levels of the system exactly using Mathieu's functions [39]. The result is indeed an anharmonic energy spectrum, with its general anharmonicity a function of both n_g and $\frac{E_J}{E_C}$ (where we omit the Φ dependence for brevity), as shown in figure 2.3. More explicitly, the figure shows the first three eigenvalues ($n = 0, 1, 2$) of the Hamiltonian in units of the first transition energy $E_{01} = E_1 - E_0$ evaluated at $n_g = 1/2$. Note that for the CPB panel (a) is the most relevant, as originally it is operated in the $\frac{E_J}{E_C} \approx 1$ regime [40, 41]. One can observe that here there is significant variation of the energy level structure with respect to n_g (referred to as its charge dispersion), which makes it prone to noise in this parameter. Traditionally the CPB is therefore operated at its so called sweet spot, denoted by the dashed lines in panel (a). Here the transition frequency is insensitive to noise in n_g to first order and the level structure is strongly anharmonic [42].

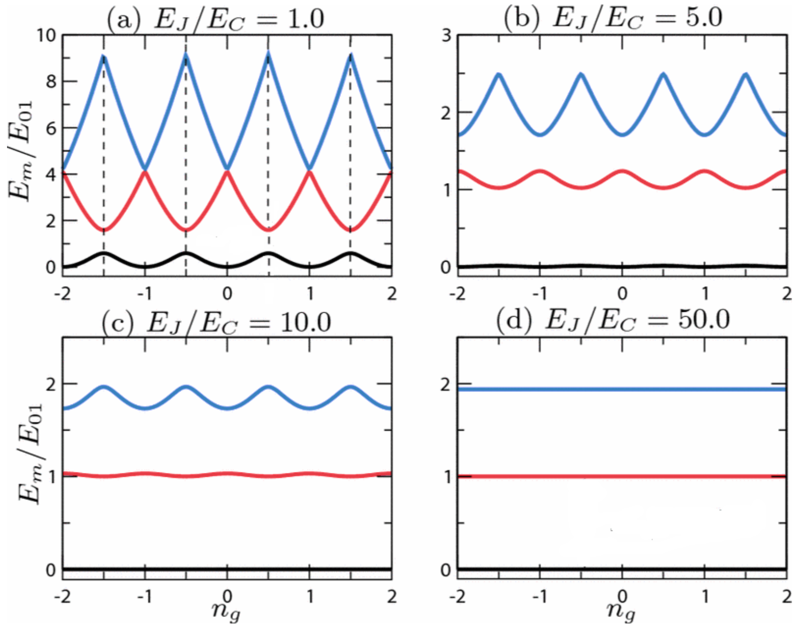

Figure 2.3: Eigenenergies E_m of the CPB Hamiltonian (equation 2.13) for the first three energy levels ($m = 0, 1, 2$) as a function of the polarization charge n_g for different ratios E_J/E_C. Note that the energies are normalized by the transition energy E_{01} evaluated at the degeneracy point $n_g = 1/2$, indicated by vertical dashed lines in panel (a). Figure taken from [39].

2.1.3 The Transmon regime

While operating at the sweet spot mitigates some of the influence of noise in n_g, jumps and drifts in the offset charge will still affect the qubit and induce decoherence. This is where the transmon distinguishes itself from the CPB: by adding a large shunting capacitor C_B between the island and the reservoir (the green part of figure 2.2) one increases C_Σ, which in turn reduces E_C and thus increases $\frac{E_J}{E_C}$ [39]. As shown in the panels of figure 2.3 this strongly reduces the sensitivity to n_g, improving the coherence time of the system with respect to the CPB. As the panels also show this is not without a disadvantage, as the anharmonicity of the levels reduces when increasing $\frac{E_J}{E_C}$ into the regime of tens to several hundreds. However, this is the key point of the transmon system: increasing the ratio $\frac{E_J}{E_C}$ causes an exponential decrease in the charge sensitivity, but only an algebraic decrease in the anharmonicity [39]. The transmon is therefore designed with this interplay in mind, operating in the regime where the anharmonicity is still sufficient to perform qubit experiments while improving coherence times.

In its full form the Hamiltonian of the transmon takes on the same form as that of the split CPB, given by equation 2.12 with an adjusted E_C. As written above, this can be solved analytically in the phase basis using Mathieu's functions. However as apparent from figure 2.3(d) and detailed in [39], the transmon is essentially a weakly anharmonic harmonic oscillator; in the limit of $\frac{E_J}{E_C} \gg 1$ one can approximate the eigenvalues of the Hamiltonian by those of the Duffing oscillator

$$E_n \approx -E_J(\Phi) + \sqrt{8E_C E_J(\Phi)}\left(n + \frac{1}{2}\right) - \frac{E_C}{12}\left(6n^2 + 6n + 3\right) \tag{2.14}$$

This allows one to quantify a number of useful concepts, such as the transition frequency between the ground state g and the first excited state e:

$$\hbar\omega_{eg}(\Phi) = (E_1 - E_0) \approx \sqrt{8E_C E_J \left|\cos\left(\pi\frac{\Phi}{\Phi_0}\right)\right|} - E_C \tag{2.15}$$

This expression will be the basis for the operation of the qubits in this thesis: in almost all scenario's discussed we restrict our system to its lowest two levels so that the Hamiltonian is given by that of a typical qubit with transition frequency ω_{eg}

$$\hat{\mathcal{H}} = \frac{\hbar\omega_{eg}(\Phi)\hat{\sigma}_z}{2} \tag{2.16}$$

where $\hat{\sigma}_z$ is the Pauli z matrix. This is exactly of the form of the (uncoupled) pigment sites discussed in chapter 1.

In order to operate our system in the regime where this holds we need to be mindful of the absolute and relative anharmonicity between the first excited state and second excited state (f state) so that we do not leave our desired subspace. For the transmon these quantities are denoted by α and α_r respectively and approximately given by [39]

$$\alpha \approx -E_C,\ \alpha_r \approx -\left(\frac{8E_J(\Phi)}{E_C}\right)^{-1/2} \tag{2.17}$$

It is interesting to note that the anharmonicity is negative; in contrast to the split CPB operated at its sweet spot (figure 2.3a) the energy difference between the e and the f state is smaller than between g and e.

While we have set up the framework governing the qubit system of interest in this thesis, we have not yet developed the tools used to interact with the device. In order to probe the system one needs to be able to send signals into the qubits as well as detect the photons output by the system, and in addition to that one might be interested in the interaction between the photons and the system itself. This relates back to the concepts of the antenna and the reaction center, which serve as the input and output of the FMO-type system. In the next section we develop the theory governing the elements used for this.

2.2 Coplanar Waveguides

In the superconducting circuit architecture the primary structure used to interact with the transmons is the coplanar waveguide (CPW): the two dimensional analog of the coaxial cable. It is a planar structure built up out of a centre conducting strip separated from ground planes on both sides, essentially making it a slotline with a third conductor centered in the slot region as schematically depicted in figure 2.4. Due to this geometry it functions as a transmission line, supporting even or odd quasi-TEM modes depending on the relative direction of the electric field in the two slots as described by transmission line theory [43].

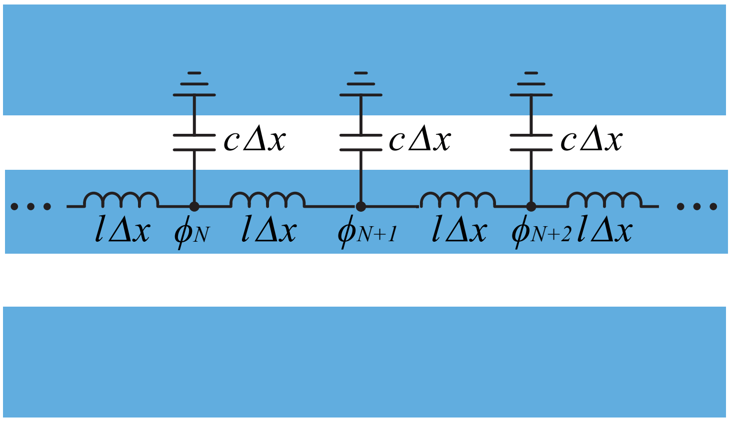

Figure 2.4: A schematic depiction of a coplanar waveguide. Figure adapted from [44].

As also depicted in figure 2.4, one can instead choose to model the system using a distributed element representation as detailed in [45]. In this framework one describes the system of length d as an infinite chain of capacitances and inductances per unit length, c and l respectively, spaced at an interval

Δx with fluxnodes ϕ_i. The system is therefore essentially a chain of coupled LC oscillators, which facilitates its quantization. We again begin with the Lagrangian of the system, starting from a discrete representation of N segments of length Δx:

$$\mathcal{L} = \sum_{i=1}^{N} \frac{c\Delta x}{2}\dot{\phi}_i^2 - \sum_{i=1}^{N-1} \frac{(\phi_{i+1} - \phi_i)^2}{2l\Delta x} \tag{2.18}$$

In the continuum limit of $N \to \infty$ and $\Delta x \to 0$ the above becomes the integral [45]

$$\mathcal{L} = \int_0^d dx \frac{c\dot{\phi(x,t)}_i^2}{2} - \frac{1}{2l}\left(\frac{\partial\phi(x,t)}{\partial x}\right)^2 \tag{2.19}$$

where $\phi(x,t)$ is now a flux density. Before moving on to the Hamiltonian description of the system we first look at the Euler-Lagrange equation of the system, which turns out to have the form of the wave equation

$$\frac{\partial^2\phi}{\partial t^2} - v^2\frac{\partial^2\phi}{\partial x^2} = 0 \tag{2.20}$$

with $v = \frac{1}{\sqrt{lc}}$; the speed of light in the waveguide is thus set by c and l. This equation has the general solution

$$\phi(x,t) = \sum_{n=1}^{\infty} A_n \cos\left(k_n x + \alpha_n\right)\cos\left(k_n v t + \beta_n\right) \tag{2.21}$$

where A_n, k_n, α_n and β_n all depend on the boundary conditions of the system. In this thesis we are mostly concerned with open boundaries at $x = 0$ and $x = d$, for which the derivative has to vanish at the boundaries and thus $\alpha_n = 0$ and $k_n = \frac{n\pi}{d}$, whereas the other two constants are determined by the initial conditions [45]. More importantly, substituting the solution to the wave equation with these conditions and integrating over space results in

$$\mathcal{L} = \sum_{n=1}^{\infty} \frac{C_n}{2}\dot{\phi}_n^2 - \frac{\phi_n^2}{2L_n} \tag{2.22}$$

where $\phi_n = A_n \cos\left(k_n v t + \beta_n\right)$, $C_n = \frac{cd}{2}$ and $L_n = \frac{2ld}{n^2\pi^2}$ Comparing equation 2.22 to the Lagrangian of the LC oscillator (equation 2.2) shows that the coplanar waveguide is thus essentially an infinite chain of uncoupled LC oscillators [45]; its second quantization form Hamiltonian is thus given by

$$\hat{\mathcal{H}} = \sum_{n=1}^{\infty} \hbar\omega_n\left(\hat{a}_n^\dagger\hat{a}_n + \frac{1}{2}\right) \tag{2.23}$$

with $\omega_n = \frac{1}{\sqrt{L_N C_N}} = \frac{n\pi}{d}\frac{1}{\sqrt{lc}}$. From this one can also calculate the effective characteristic impedance of mode n, given by $Z_n = \sqrt{\frac{L_n}{C_n}} = \frac{2}{\pi n}\sqrt{\frac{l}{c}}$.

The above equation has two regimes relevant for this thesis. The first is for long waveguides with large length d; here the spacing between the modes is very small and essentially every mode is supported. We use such coplanar waveguides as transmission lines for the transmons, capable of transporting photons in and out of the system at virtually any frequency. One can therefore see it as the antenna complex of FMO, introducing excitations to the pigment sites.

Its Hamiltonian can be derived from equation 2.23 by assuming that the CPW essentially has infinite length (or equivalently no boundary conditions), resulting in

$$\hat{\mathcal{H}} = \int_0^\infty d\omega\hbar\omega \left(\hat{a}_n^\dagger \hat{a}_n + \frac{1}{2}\right) \tag{2.24}$$

However, as noted in the introduction of this section the coplanar waveguide has two slots, essentially limiting the modes to travel either to the left or to the right. The above can therefore also be written as [46]

$$\hat{\mathcal{H}} = \int_0^\infty d\omega\hbar\omega \left(\hat{a}_R^\dagger \hat{a}_R + \hat{a}_L^\dagger \hat{a}_L\right) \tag{2.25}$$

where $\hat{a}^\dagger_{\{R,L\}}$ denote right and left propagating modes respectively and where we have dropped the zero field offset for convenience. Moreover, in the above two Hamiltonians the dimensions of the creation and annihilation operators have been redefined to incorporate $d \rightarrow \infty$, reflected in the apparent change of units of in the overall Hamiltonian.

The other regime is for d at an intermediate value, such that the energy level spacing is large enough that we can essentially reduce the above Hamiltonian to a single harmonic resonator of fundamental frequency $\omega_r = \frac{\pi}{d}\frac{1}{\sqrt{lc}}$:

$$\hat{\mathcal{H}} = \hbar\omega_r \hat{a}^\dagger \hat{a} \tag{2.26}$$

Such CPWs are known as coplanar waveguide resonators. As they follows the same physics as the LC circuit, we treat them as such in the theory that follows. Their fabrication and functioning is extensively documented in [24], of which some of the details are contained in chapter 3. For now it is sufficient to know that they are essentially a segment of coplanar waveguide separated from CPW transmission lines at each end by a gap, which causes a capacitive coupling and essentially functions as mirrors of the Fabry-Perrot cavity. While such resonators allow for a wide range of applications in circuit QED (such as qubit control and dispersive readout), in this thesis we mostly use them to induce decay of the qubit excitations via the Purcell effect [39] as detailed in the next section. They thus function as the systems reaction center, irreversibly transferring excitations out of the pigment sites.

With this we have treated the relevant theory of individual coplanar waveguides. However, it is important to point out that in order for the above quantum description to hold the CPW needs to have low losses in order to preserve coherences. For this reason the CPWs in this thesis are made out of superconducting materials such as niobium, as outlined in chapter 3.

2.3 Interactions Between the Elements

In the previous sections we have introduced three distinct elements: transmon qubits, coplanar waveguide transmission lines, and coplanar waveguide resonators. While we have discussed the functioning of each element by itself, we have yet to introduce the interactions between the individual elements and the behavior of the system as a whole. This is the purpose of this section, starting off with a general circuit picture capturing the entire system and the focusing on the interactions between the individual elements one by one.

The system studied in this thesis is shown in figure 2.5. The top component is a CPW transmission line with capacitance and inductance per unit length c and l, shown in purple. We then have three transmon qubits (Q1, Q2 and Q3) with capacitances C_i and Josephson energies E_{Ji}, shown in red, blue, and green respectively. Finally we have a CPW resonator with effective capacitance and inductance C_r and L_r shown in orange; as discussed in the previous section these depend on the resonator length and the energy level.

A number of these elements are capacitively coupled to each other: qubits 1 and 2 are designed to capacitively couple to the transmission line via $C_{t\{1,2\}}$, while qubit 3 couples to the resonator with C_{3r}. In addition to this, there is a strong coupling C_{12} between qubits 1 and 2, and a weaker coupling C_{23} between qubits 2 and 3. In addition to this, the diagram depicts potential stray couplings between the other elements in gray. Finally it is important to note that this design deviates from the standard floating transmons; instead all components share a common ground to reduce the stray capacitance C_{13} as much as possible.

In order to solve the Hamiltonian of this system we adopt the same approach as used before, first setting up the Lagrangian of the system and then applying the Hamiltonian and second quantization formalisms in correspondence with the techniques described in the respective sections of each element. We again start off with a Lagrangian in terms of the flux coordinates of each

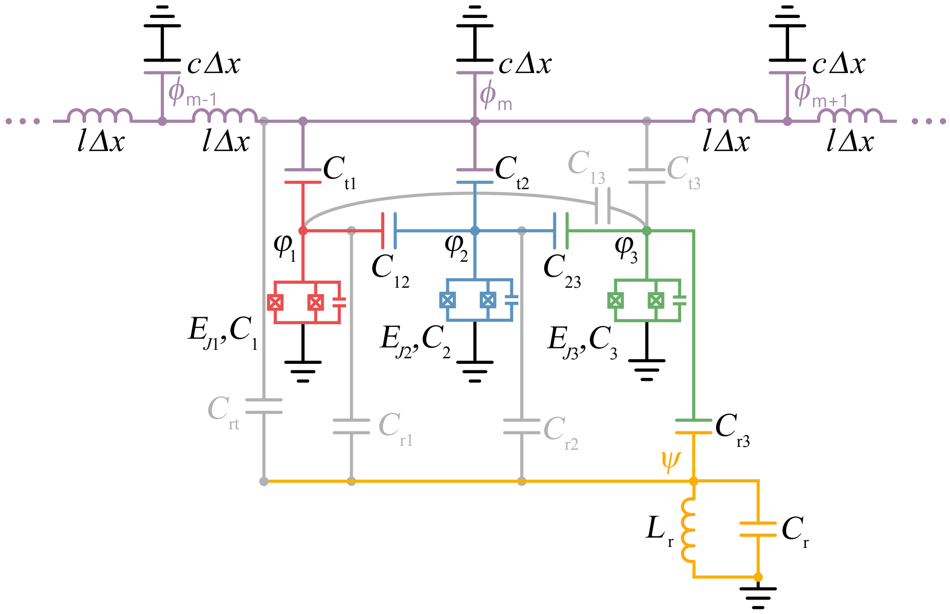

Figure 2.5: Circuit diagram of the system studied in this thesis. It consists of a CPW transmission line (purple), three transmon qubits (red, blue, green) and a CPW resonator. Designed couplings are shown in the color of the involved elements, while stray couplings are shown in gray. The flux coordinates of these elements are also denoted, with ϕ_m *being the transmission line flux coordinate,* φ_j *the coordinate of transmon* j *and* Ψ *the coordinate of the CPW resonator.*

component

$$\mathcal{L} = \sum_{m=1}^{N} \frac{c\Delta x}{2}\dot{\phi}_m^2 - \sum_{m=1}^{N-1} \frac{\{\phi_{m+1} - \phi_m\}^2}{2l\Delta x} + \sum_{j=1}^{3} \left\{ \frac{C_{tj}}{2}[\dot{\phi}_m - \dot{\varphi}_j]^2 + \sum_{i<j} \frac{C_{ij}}{2}[\dot{\varphi}_i - \dot{\varphi}_j]^2 \right.$$

$$\left. + \left[\frac{C_j}{2}\dot{\varphi}_j^2 + E_{Jj}\cos\left(\frac{2\pi}{\Phi_0}\varphi_j\right)\right]^2 + \frac{C_{rj}}{2}[\dot{\psi} - \dot{\varphi}_j]^2 \right\} + \frac{C_r}{2}\dot{\psi}^2 - \frac{\psi^2}{2L_r}, \tag{2.27}$$

where ϕ_m, φ_j and ψ are the generalized fluxes of the transmission line, the qubits and the resonator respectively, $\frac{2\pi}{\Phi_0}\varphi_j = \delta_j$ and Δx is again the unit length of the discretized transmission line. Moreover, we have implicitly assumed that the qubits couple to the transmission line at the same position $x = x_m$; this can be justified by noting that the wavelength of the microwave photons relevant for transmons is much larger than the size of the structure.

In order to obtain the Hamiltonian it is convenient to rewrite the Lagrangian in matrix form

$$\mathcal{L} = \dot{\Phi}^{\mathrm{T}}\underline{C}\dot{\Phi} - \Phi^{\mathrm{T}}\underline{L}^{-1}\Phi, \tag{2.28}$$

where $\dot{\Phi}^{\mathrm{T}} = [\dot{\phi}_1, \dot{\phi}_2, \cdots, \dot{\phi}_N, \dot{\varphi}_1, \dot{\varphi}_2, \dot{\varphi}_3, \dot{\psi}]$, $\underline{L}$ is a matrix of inductances and $\underline{C}$ a matrix of capacitances. We can now employ the definition of the canonical conjugate momentum $q_i \equiv \frac{\partial \mathcal{L}}{\partial \dot{\phi}_i} = C_{ij}\dot{\phi}_j$ for each of the coordinates and obtain a Hamiltonian in matrix form

$$\mathcal{H} = \frac{1}{2} Q^T \underline{C}^{-1} Q + \frac{1}{2} \Phi^T \underline{L}^{-1} \Phi \tag{2.29}$$

where we define $Q^{\mathrm{T}} = [p_1, p_2, \cdots, p_N, q_1, q_2, q_3, r]$, which is a vector of conjugate momenta. Next we elevate our coordinates to operators through the enforcement of the canonical commutation relations and finally transform the Hamiltonian to the second quantization formalism as done in the previous sections. Our final Hamiltonian is then given by

$$\hat{\mathcal{H}} = \hat{\mathcal{H}}_{\mathrm{T}} + \hat{\mathcal{H}}_{\mathrm{R}} + \hat{\mathcal{H}}_{\mathrm{A}} + \hat{\mathcal{H}}_{\mathrm{T-A}} + \hat{\mathcal{H}}_{\mathrm{T-R}} + \hat{\mathcal{H}}_{\mathrm{A-A}} + \hat{\mathcal{H}}_{\mathrm{A-R}} \tag{2.30}$$

denoting the different parts of the system: A for transmon artifical atom or qubit, T for CPW transmission line and R for CPW resonator.

The first three parts of the system Hamiltonian have already been derived in their respective sections. Furthermore, we assume that $\hat{\mathcal{H}}_{\mathrm{T-R}}$ can be neglected altogether; there should be virtually no coupling between these elements. The other interaction Hamiltonians are of interest, and we treat them in more detail in the next sections. Note that in these sections we will not explicitly derive expressions for the relevant parameters in terms of the above matrices $\underline{C}$ and $\underline{L}$; this is done in appendix B.

2.3.1 Transmon-Transmon Coupling

The first interaction of interest is between the transmons themselves. The three transmon system is described by the combined Hamiltonian $\hat{\mathcal{H}}_{\mathrm{AA}} = \hat{\mathcal{H}}_{\mathrm{A}} + \hat{\mathcal{H}}_{\mathrm{A-A}}$ given by

$$\hat{\mathcal{H}}_{\mathrm{AA}}/\hbar = \sum_{j=1}^{3} \left[\frac{\omega_j}{2} \hat{\sigma}_{z,j} + \sum_{k<j} J_{kj} (\hat{\sigma}_k^+ + \hat{\sigma}_k^-)(\hat{\sigma}_j^+ + \hat{\sigma}_j^-) \right] \tag{2.31}$$

where $\hat{\sigma}_j^{\{+,-\}}$ are the raising and lowering operators of the qubits given by $\hat{\sigma}_{x,j} = \hat{\sigma}_j^+ + \hat{\sigma}_j^-$ and J_{jk} denotes the coupling between the qubits. It is proportional to the coupling capacitance $C_j k$ as given in B.

This Hamiltonian contains terms where qubits exchange an excitation proportional to $\hat{\sigma}_k^{\pm}\hat{\sigma}_j^{\mp}$, as well as terms where both qubits gain and lose an excitation simultaneously proportional to $\hat{\sigma}_k^{\pm}\hat{\sigma}_j^{\pm}$. For the scenarios of interest the latter terms can be dropped in the so called rotating wave approximation (RWA) [47] in order to obtain the simplified Hamiltonian

$$\hat{\mathcal{H}}_{\mathrm{AA}}/\hbar = \sum_{j=1}^{3} \left[\frac{\omega_j}{2} \hat{\sigma}_{z,j} + \sum_{k<j} J_{kj} \left(\hat{\sigma}_k^+ \hat{\sigma}_j^- + \hat{\sigma}_j^+ \hat{\sigma}_k^- \right) \right] \tag{2.32}$$

Depending on the relative values of the parameters, the Hamiltonian has several regimes of interest. The main regime studied in this report is when qubits 1 and 2 are on resonance: $\omega_1 = \omega_2 = \omega_a$. For illustration purposes we first leave out the third qubit and write

$$\hat{\mathcal{H}}_{\mathrm{AA}}/\hbar = \frac{\omega_a}{2}\hat{\sigma}_{z,1} + \frac{\omega_a}{2}\hat{\sigma}_{z,2} + J_{12}\left(\hat{\sigma}_1^+\hat{\sigma}_2^- + \hat{\sigma}_2^+\hat{\sigma}_1^-\right) \tag{2.33}$$

We can then diagonalize this Hamiltonian by introducing two new modes B and D for which $\hat{\sigma}^{\pm}_{B,D} = \frac{1}{\sqrt{2}}\left(\hat{\sigma}_1^{\pm} \pm \hat{\sigma}_2^{\pm}\right)$ and analogous expressions for the other operators. Substituting this into the Hamiltonian gives

$$\hat{\mathcal{H}}_{\mathrm{AA}}/\hbar = \frac{\omega_B}{2}\hat{\sigma}_{z,B} + \frac{\omega_D}{2}\hat{\sigma}_{z,D} \tag{2.34}$$

where $\omega_{B,D} = (\omega_a \pm J_{12})$. The resulting Hamiltonian is thus one of two uncoupled qubits, which are often referred to as the symmetric and the antisymmetric mode or the bright and the dark mode. While the first name simply refers to the phase relation between the two qubits, the terms bright and dark refer to how these modes interact with the waveguide they are coupled to; this is derived in the section governing the interaction between the qubits and the waveguide itself.

It is also of interest to apply the previously introduced transformation to the Hamiltonian of the three coupled qubits. We start from equation 2.32, set the frequencies of the first two qubits equal to ω_a and apply the transformations:

$$\hat{\mathcal{H}}_{\mathrm{AA}}/\hbar = \sum_{j=\{B,D,3\}}\frac{\omega_j}{2}\hat{\sigma}_{z,j} + J_{B3}\left(\hat{\sigma}_B^+\hat{\sigma}_3^- + \hat{\sigma}_3^+\hat{\sigma}_B^-\right) + J_{D3}\left(\hat{\sigma}_D^+\hat{\sigma}_3^- + \hat{\sigma}_3^+\hat{\sigma}_D^-\right) \tag{2.35}$$

where $J_{\{B,D\}3} = \frac{1}{\sqrt{2}}(J_{13} \pm J_{23})$; the coupling between the dark mode and qubit 3 and the bright mode and qubit 3 is not equal if none of the individual qubit couplings are nonzero, which might be relevant in the presence of finite (parasitic) capacitance C_{13}.

2.3.2 Transmon-Resonator Coupling

The second interaction we look at is between the transmons and the CPW resonator; a subset of an entire research field known as cavity quantum electrodynamics (cQED). An extensive review can be found in [48]; here we only cover the basics of the interactions and the results relevant for the thesis.

The Hamiltonian of the combined three qubit resonator system $\hat{\mathcal{H}}_{\mathrm{AR}} = \hat{\mathcal{H}}_{\mathrm{A}} + \hat{\mathcal{H}}_{\mathrm{R}} + \hat{\mathcal{H}}_{\mathrm{A-R}}$ is given by

$$\hat{\mathcal{H}}_{\mathrm{AR}}/\hbar = \omega_r\hat{a}^\dagger\hat{a} + \sum_{i=1}^{3}\frac{\omega_j}{2}\hat{\sigma}_{z,j} + g_{ir}\left(\hat{a}^\dagger + \hat{a}\right)\left(\hat{\sigma}_i^+ + \hat{\sigma}_i^-\right) \tag{2.36}$$

where g_{ir} is the term that dictates the coupling strength. It is proportional to C_{ri} and explicitly defined in B. If one then again applies the RWA, one can drop the terms corresponding to $\hat{a}^\dagger\hat{\sigma}_i^+$ and $\hat{a}\hat{\sigma}_i^-$ and obtain the famous Jaynes-Cummings Hamiltonian [49]

$$\hat{\mathcal{H}}_{\mathrm{AR}}/\hbar = \omega_r \hat{a}^\dagger \hat{a} + \sum_{j=1}^{3} \left[\frac{\omega_j}{2}\hat{\sigma}_{z,j} + g_{jr}\left(\hat{a}^\dagger\hat{\sigma}_j^- + \hat{\sigma}_j^+\hat{a}\right)\right] \tag{2.37}$$

governing the relevant interactions between the qubits and the resonator.

In the context of circuit QED one typically studies the interactions between the resonator and the qubits in the dispersive regime, where the parameter hierarchy

$$\Delta^2 = \left(\omega_{eg} - \omega_r\right)^2 \gg g^2 \tag{2.38}$$

allows one to further approximate the above Hamiltonian. However, in this thesis qubit 3 (which is the only qubit that couples to the resonator, neglecting parasitic capacitances) is in the $\Delta \approx g$ regime, meaning that such approximations do not hold. While crucial for techniques such as quantum non-demolition (QND) readout, in our experiments the resonator plays a very different role altogether; we use it to reduce the lifetime of the qubits through the Purcell effect.

Discovered in 1946 by Edward Mills Purcell [50], the Purcell effect describes how a system coupled to a resonator has its decay rate Γ altered. This also holds for the transmon, where each of its excited states will have an altered decay rate when coupled to a resonator. While relatively simple expressions for this alteration can be obtained for a dispersively coupled transmon [39], we require the expressions valid in the full regime, as is derived in [51]. There one finds that the decay rate due to the Purcell effect is given by

$$\Gamma = \frac{\kappa}{2} - \frac{\sqrt{2}}{2}\sqrt{-A + \sqrt{A^2 + (\kappa\Delta)^2}} \tag{2.39}$$

with

$$A = \Delta^2 + 4g^2 - \frac{\kappa^2}{4} \tag{2.40}$$

where κ is the decay rate of the resonator. Equation 2.39 obeys the two standard limits: for $\Delta \to 0$ we have that $\Gamma \to \frac{\kappa}{2}$; the two systems fully hybridize into two new modes. For $\Delta^2 \gg g^2$ one can derive the standard dispersive expression $\Gamma = \kappa\left(\frac{g}{\Delta}\right)^2$ [39, 51].

Note that formally speaking the decay rate has two contributions: $\Gamma = \gamma_r + \gamma_{nr}$ where γ_r is radiative decay in the form of photons and γ_{nr} is nonradiative decay through a number of other channels, which is typically a small contribution in transmons. The Purcell effect is a radiative decay channel, and for the regimes encountered in this thesis it can therefore be assumed that the decay rate of qubit 3 Γ_3 is dominated by radiative decay γ_{r3} into the resonator. It is this process that can be seen as mimicking the reaction center of FMO, with qubit 3 playing the role of the pigment site closest to the reaction center into which it irreversibly transfers its excitations.

2.3.3 Transmon-Transmission Line Coupling

The final interaction Hamiltonian that is to be covered is $\hat{\mathcal{H}}_{\mathrm{T-A}}$, the interaction between the transmission line and the transmons. These interactions have gained much interest in recent times [46, 52] because the CPW transmission line is essentially a one dimensional system: the reduced dimensionality offers advantages in the context of strong light-matter interactions due to an increased interaction strength compared to open three dimensional systems [53]. While these strong interactions are not of specific interest in this thesis, we will draw from recent work in this area to cover the interactions between the transmons and the waveguide, using [46] as a guide.

Neglecting the potential parasitic coupling to qubit 3 (given by C_{t3}), we now treat the interaction between qubits 1 and 2 and the transmission line governed by $\hat{\mathcal{H}}_{\mathrm{TA}} = \hat{\mathcal{H}}_{\mathrm{T}} + \hat{\mathcal{H}}_{\mathrm{A}} + \hat{\mathcal{H}}_{\mathrm{T-A}}$. Following [46] the interaction Hamiltonian takes the form

$$\hat{\mathcal{H}}_{\mathrm{T-A}}/\hbar = \sum_{j=1}^{2} b_j \left(\hat{\Xi}_j^\dagger + \hat{\Xi}_j \right) \hat{\sigma}_{x,j} \tag{2.41}$$

where b_{jt} is the coupling strength between the transmons and the transmission line; it is generally denoted by g_{jt} but here it has been renamed in order to avoid confusion with the resonator transmon coupling. It is proportional to C_{tj} as given in B. Moreover, $\hat{\Xi}_j$ is related to the electric field at location x_j of the jth transmon and is given by

$$\hat{\Xi}_j = -i \int_0^\infty d\omega \sqrt{\omega} \left[\hat{a}_L e^{-i\omega x_j/v} + \hat{a}_R e^{i\omega x_j/v} \right] \tag{2.42}$$

where $v = \frac{1}{\sqrt{lc}}$ is the phase velocity in the transmission line. As $\hat{\sigma}_{x,j} = \hat{\sigma}_j^+ + \hat{\sigma}_j^-$ one can see that this form of the interaction only involves transitions between adjacent states of the qubits.

Solving the above interaction is rather complex, as it involves a continuum of modes travelling in both directions. However, as shown in [46] one can solve the Heisenberg equations of motion for the field modes $\hat{a}_{\{L,R\}}$ and express $\hat{\Xi}_j$ in terms of an incoming field and a time dependent coupling to the atom in order to simplify the situation. Following [44] we make the Markov, long-time, and rotating wave approximations while absorbing Lamb shifts into the qubit energies, allowing us to trace out the transmission line field degrees of freedom. The two qubit-waveguide system can then be expressed in terms of a master equation

$$\dot{\rho} = \mathcal{L}(\rho) \tag{2.43}$$

where ρ is the density matrix and $\mathcal{L}(\rho)$ is known as the Liouvillian superoperator of the system; it maps operators to operators. Given the approximations mentioned above it takes on the so called Lindblad form

$$\mathcal{L}(\rho) = -\frac{i}{\hbar}\left[\hat{\mathcal{H}}, \rho\right] + \sum_{j=1}^{N} h_j \left(L_j \rho \hat{L}^{\dagger} - \frac{1}{2}\{L_j^{\dagger} L_j, \rho\} \right) \tag{2.44}$$

where L_j is known as a Lindblad superoperator, h_j is a constant and $\{\hat{a}, \hat{b}\}$ denotes the anti-commutator of operators $\hat{a}$ and $\hat{b}$.

For the interactions induced by the transmission line the Liovillian is given by

$$\mathcal{L}(\rho) = -\frac{i}{\hbar}\left[\hat{\mathcal{H}}_{\text{TA}}, \rho\right] + \sum_{j=1}^{2} \Gamma_j \left[\hat{\sigma}_j^- \rho \hat{\sigma}_j^+ - \frac{1}{2}\left(\hat{\sigma}_j^+ \hat{\sigma}_j^- \rho + \rho \hat{\sigma}_j^+ \hat{\sigma}_j^- \right) \right] \tag{2.45}$$

and the Hamiltonian is given by

$$\hat{\mathcal{H}}_{\text{TA}}/\hbar = \sum_{j=1}^{2} \left[\frac{\omega_j}{2} \hat{\sigma}_{z,j} + d_j(t) \hat{\sigma}_{x,j} \right] \tag{2.46}$$

while $d_j(t)$ is an effective drive term of the transmon qubits, its form dependent on the signal input into the transmission line. Formally equation 2.46 also contains a waveguide mediated qubit interaction term $J_{12,T}$, but this is expected to be significantly smaller than the designed capacitive J_{12} for two qubits separated by much less than one wavelength [46]. We thus treat this as a small perturbation and absorb it into the coupling J_{12} defined previously.

Before looking into the form of $d_j(t)$ we first note that equation 2.43 contains the aforementioned decay rate Γ_j encountered in the context of the Purcell effect. As noted before it consists of two contributions: $\Gamma_j = \gamma_{rj} + \gamma_{nrj}$ being the radiative and non-radiative decay. However, as qubits 1 and 2 do not couple to the resonator (up to parasitic coupling) they are not subject to the Purcell effect and γ_r thus has no contribution from that. Instead in tracing out the field degrees of freedom the waveguide adds a significant contribution to the radiative decay $\gamma_{rj} \propto C_{tj}$ such that for qubits 1 and 2 one can also assume that Γ_j is dominated by radiative decay, this time into the transmission line.

Returning to the drive term $d_j(t)$, one can derive that for an input coherent field coming from the left (or right) side of the transmission line it is given by

$$d_j(t) = 2\sqrt{\frac{\Gamma_j}{2}}\sqrt{\frac{P}{\hbar\omega_j}}\sin\left(\omega_d t\right) \tag{2.47}$$

where P is the applied microwave power in Watts and ω_d is the frequency of the driving field. However, such time dependent Hamiltonians are often difficult to handle; by going into the rotating frame of the drive frequency one can transform equation 2.46 into the simplified form

$$\hat{\mathcal{H}}_{\mathrm{TA}}/\hbar = \sum_{j=1}^{2}\left[\frac{\omega_j}{2}\hat{\sigma}_{z,j} + \Omega_j\hat{\sigma}_{x,j}\right] \tag{2.48}$$

where $\Omega_j = 2\sqrt{\frac{\Gamma_j}{2}}\sqrt{\frac{P}{\hbar\omega_j}}$ is a time independent driving term. The above thus establishes the CPW transmission line as the antenna of the pigment system, introducing excitations into the system at a rate Ω_j.

While at this stage we have covered the interaction between the transmission line and uncoupled qubits, it is also interesting to look at the above for coupled transmons. Taking the coupling into account, equation 2.48 instead takes the form

$$\hat{\mathcal{H}}_{\mathrm{TAA}}/\hbar = \sum_{j=1}^{2}\left[\frac{\omega_j}{2}\hat{\sigma}_{z,j} + \Omega_j\hat{\sigma}_{x,j} + \sum_{k<j} J_{kj}\left(\hat{\sigma}_k^+\hat{\sigma}_j^- + \hat{\sigma}_j^+\hat{\sigma}_k^-\right)\right] \tag{2.49}$$

If we now again set the two qubit frequencies equal to ω_a and move into the bright/dark mode basis (as was done in equation 2.34) we find that

$$\hat{\mathcal{H}}_{\mathrm{TAA}}/\hbar = \sum_{k=\{B,D\}}\frac{\omega_k}{2}\hat{\sigma}_{z,k} + \Omega_k\hat{\sigma}_{x,k} \tag{2.50}$$

where $\Omega_{B,D} = \frac{1}{\sqrt{2}}\left(\Omega_1 \pm \Omega_2\right)$. We see that in the scenario where $\Omega_1 = \Omega_2$ the bright mode has an enhanced driving rate while the dark mode is not driven at all; it decouples from the transmission line. This is also seen in the correlated decay of the states, which in the bright/dark basis are given by [46]

$$\Gamma_{B,D} = \frac{\gamma_{r1} + \gamma_{r2}}{2} \pm \sqrt{\left(\frac{\gamma_{r1} - \gamma_{r2}}{2}\right)^2 + |\gamma_{12}|^2} \tag{2.51}$$

where

$$\gamma_{12} = \sqrt{\left(\gamma_{r1} - \gamma_{nr1}\right)\left(\gamma_{r2} - \gamma_{nr2}\right)} \tag{2.52}$$

is the correlated decay rate of the two qubits. Combining the two above equations for $\gamma_{nr1} = \gamma_{nr2} = \gamma_{nr} \ll \gamma_{r\{1,2\}}$ one finds that [46]

$$\Gamma_D = \gamma_{nr} \ll \Gamma_B = \gamma_{r1} + \gamma_{r2} - \gamma_{nr} \tag{2.53}$$

The above is an interesting result: in the ideal scenario where the two coupled qubits are identical and couple equally to the transmission line, they form two new modes. The first of these is short lived and radiates approximately twice as much as the individual qubits, whereas the other is long lived and does not radiate at all. This is the reason behind naming them the bright and the dark mode.

2.4 Classical Noise Environments

At this stage have covered the theory governing the physical elements of our setup and how they interact with one another. While the study of these interactions is of interest by itself, our motivation is more involved: as introduced in chapter 1, we want to study the interactions of the system in the presence of a classical noise environment. In appendix A we introduced several concepts related to such noise, being its probability distribution, its power spectral density and its effect on a qubit when it takes the form of a time-varying transition frequency $\delta\omega(t)$. In this section we quantify these concepts for the transmon qubits.

2.4.1 Flux Noise

In order to quantify the effect of a classical noise environment on the transmon qubits, we first need to establish what constitutes their environment. We do so for a single qubit, and the analysis can then be extended to any system size. A convenient starting point is the quantity that determines the evolution of a single transmon qubit, its Hamiltonian:

$$\mathcal{H}_0/\hbar = -\frac{\omega_0}{2}\hat{\sigma}_z \tag{2.54}$$

where we have derived that ω_0 is given by

$$\omega_0 = \sqrt{8E_C E_J \left|\cos\left(\pi\frac{\Phi}{\Phi_0}\right)\right|} - E_C \tag{2.55}$$

Looking back at this this equation we see that the transition frequency has three components: E_C, E_J and Φ. In section 2.1 we have previously established that the charging energy E_C and the Josephson energy E_J are assumed to be fixed for a fabricated transmon; the charging energy is determined by the total capacitance of the circuit C_Σ, and the Josephson energy is determined by the critical current of the junction I_0 which is a property of the materials and geometry used. At higher temperatures one can envision that these parameters might be subject to small fluctuations, but at the temperatures relevant for the operation of the transmon qubits this is negligible.

After fabrication the Hamiltonian of the transmon qubit is therefore purely parametrized by the external magnetic flux Φ, which is typically set to some working point value. However it is also affected by noise and can be written in the form $\Phi(t) = \Phi + \delta\Phi(t)$; it is what constitutes the noise environment of the transmons.

In order to quantify how such flux noise affects the Hamiltonian we express it in a Taylor series expansion about the working point value [54]

$$\mathcal{H} = \mathcal{H}_0 + \frac{d\mathcal{H}_0}{d\Phi}\delta\Phi(t) + \frac{1}{2!}\frac{d^2\mathcal{H}_0}{d\Phi^2}\delta\Phi(t)^2 + \mathcal{O}\left(\delta\Phi(t)^3\right) \tag{2.56}$$

If we subsequently assume that the deviations are small compared to the working point value we can omit the terms of order $\mathcal{O}(\delta\Phi(t)^2)$ and the resulting approximate Hamiltonian is given by

$$\mathcal{H}/\hbar = -\frac{1}{2}\left(\omega_0 + \frac{d\omega_0}{d\Phi}\delta\Phi(t)\right)\hat{\sigma}_z = -\frac{1}{2}\left(\omega_0 + \delta\omega(t)\right)\hat{\sigma}_z \tag{2.57}$$

where the derivative $\frac{d\omega_0}{d\Phi}$ is given by

$$\frac{d\omega_0}{d\Phi} = -\text{sgn}\left[\cos\left(\pi\frac{\Phi}{\Phi_0}\right)\right]\sqrt{\frac{2E_C E_J}{\left|\cos\left(\pi\frac{\Phi}{\Phi_0}\right)\right|}}\sin\left(\pi\frac{\Phi}{\Phi_0}\right)\frac{\pi}{\Phi_0} \tag{2.58}$$

We see that the flux noise $\delta\Phi(t)$ corresponds to a fluctuating transition frequency $\delta\omega(t)$, exactly like assumed for the noise environment of FMO in the Haken-Strobl-Reineker (HSR) model described by equation 1.6. In appendix A we derived that such a system is fully governed by the (exact) master equation

$$\dot{\rho} = -\frac{i}{2}\omega_0[\hat{\sigma}_z, \rho] + \frac{\gamma_\phi(t)}{2}\left(\hat{\sigma}_z\rho\hat{\sigma}_z - \rho\right) \tag{2.59}$$

where the pure dephasing $\gamma_\phi(t)$ is given by

$$\gamma_\phi(t) = \int_{-\infty}^{\infty} d\omega\, \frac{\sin(\omega t)}{\omega} S_X(\omega) \tag{2.60}$$

Note that for flux noise applied to the transmons $S_X(\omega)$ is given by $\left(\frac{d\omega_0}{d\Phi}\right)^2 S_\Phi(\omega)$ by virtue of equation 2.57. From this we find that in addition to the dependence on the flux noise power spectral density, the magnitude of the dephasing is also proportional to the derivative of the transition frequency.

We can now investigate the above for the two types of noise explored in this thesis: white noise with a constant power spectral density and noise with a Lorentzian power spectral density. It turns out that for the former the above picture can be strongly simplified: assuming that the flux noise is governed by white noise with a constant amplitude $S_\Phi(\omega) = A$ one can find that

$$\gamma_\phi(t) = A \left(\frac{d\omega_0}{d\Phi} \right)^2 \int_{-\infty}^{\infty} d\omega \, \frac{\sin(\omega t)}{\omega} = \pi A \left(\frac{d\omega_0}{d\Phi} \right)^2 \tag{2.61}$$

In this scenario the pure dephasing γ_ϕ is thus linearly proportional to the amplitude of the white noise and constant in time. This greatly reduces the complexity of the master equation, as in analogy with the Transmon-Transmission line coupling it is now given in terms of Lindblad superoperators. In terms of the evolution of the system, its coherences (given by the off diagonal elements of the density matrix) now simply decay exponentially on a timescale set by γ_ϕ.

For noise with a Lorentzian power spectral density

$$S_\Phi(\omega) = \frac{a}{1 + \left(\frac{\omega - b}{c} \right)^2} \tag{2.62}$$

the situation is more complex; here equation 2.60 evaluates to a complicated time dependent pure dephasing rate γ_ϕ. This scenario therefore does not necessarily lead to monotonically decaying coherences.

Finally it is interesting to note that given the above one can show that for the resonant coupled two qubit system of equal pure dephasing $\gamma_\phi(t)$ we find that $\gamma_{\phi\{B,D\}}(t) = \frac{\gamma_\phi(t)}{2}$ [52].

2.5 Theory of the Combined system

We have arrived at the stage where we can describe the entire system as a whole, governed by a single master equation. Including all of the concepts and approximations introduced in the previous sections, the master equation is given by $\dot{\rho} = \mathcal{L}(\rho)$ with

$$\mathcal{L}(\rho) = -\frac{i}{\hbar} \left[\hat{\mathcal{H}}, \rho \right] + \sum_{j=1}^{3} \left[\Gamma_j \left(\hat{\sigma}_j^- \rho \hat{\sigma}_j^+ - \frac{1}{2} \left[\hat{\sigma}_j^+ \hat{\sigma}_j^- \rho + \rho \hat{\sigma}_j^+ \hat{\sigma}_j^- \right] \right) + \frac{\gamma_{\phi j}(t)}{2} \left(\hat{\sigma}_{z,j} \rho \hat{\sigma}_{z,j} - \rho \right) \right] \tag{2.63}$$

where the Hamiltonian is given by

$$\hat{\mathcal{H}}/\hbar = \omega_r \hat{a}^\dagger \hat{a} + \sum_{j=1}^{3} \left[\frac{\omega_j}{2} \hat{\sigma}_{z,j} + \sum_{k<j} J_{kj} \left(\hat{\sigma}_k^+ \hat{\sigma}_j^- + \hat{\sigma}_j^+ \hat{\sigma}_k^- \right) \right] + g_{3r} \left(\hat{a}^\dagger \hat{\sigma}_3^- + \hat{\sigma}_3^+ \hat{a} \right) + \Omega_1 \hat{\sigma}_{x,1} + \Omega_2 \hat{\sigma}_{x,1} \tag{2.64}$$

and the pure dephasing rate $\gamma_{\phi j}(t)$ is given by equation 2.60. Note that here it is assumed that only qubits 1 and 2 couple to the waveguide, while only qubit 3 couples to the resonator. Moreover, the coupling between qubits 1 and 3 is not neglected; our experimental findings have shown that this parasitic coupling is significant enough to be included.

In the regime where the relevant approximations hold, the above equations govern the dynamics of the system when a coherent state is used as input. However we have not yet described what kind of field is output by the system, and how we can relate this to its internal properties. This is the topic of the next subsection, governing the input-output formalism.

2.5.1 Input-Output Theory

At its core input-output theory describes the statistical properties of light output by the system at port k given by $\hat{a}^{k}_{out}$, knowing the field input into the system at port j given by $\hat{a}^{j}_{in}$ as well as the systems Liouvillian governing its evolution $\mathcal{L}(\rho)$. Given that the main method of study in our experiments is indeed sending light into the system and observing what is output, input-output theory is our main tool of study: we use it to probe the system, gather information about its internal dynamics, and characterize the different system parameters. It can be used to define a number of useful concepts, among which the reflection and transmission coefficients of the system (also known as the scattering parameters):

$$|r|^2 = \left| \frac{\left\langle \hat{a}^{j,k}_{out} \right\rangle}{\left\langle \hat{a}^{j,k}_{in} \right\rangle} \right|^2 \tag{2.65}$$

$$|t|^2 = \left| \frac{\left\langle \hat{a}^{j,k}_{out} \right\rangle}{\left\langle \hat{a}^{k,j}_{in} \right\rangle} \right|^2 \tag{2.66}$$

for which $r + t = 1$ [55]. Note that the above holds for any combination of ports; in our thesis the relevant ports are the input and output of the transmission line and the input and output of the resonator, which share a port. With a system as intricate as ours a full theoretical evaluation of the above in any possible scenario is beyond the scope of this thesis; such calculations are best left to numerical approaches.

It is however instructive to look at a reduced picture, such as a single mode input into the transmission line from the right side of the transmission line $\hat{a}^{R}_{in}(\omega, t)$ that interacts with a single transmon qubit of transition frequency ω_0 at the center of the transmission line and leaves to the left as $\hat{a}^{L}_{out}(\omega, t)$. The theory governing this process is described in [44, 46] where one finds that

$$\hat{a}^L_{out}(\omega, t) = \hat{a}^R_{in}(\omega, t) + e^{-i\omega_0 t_0}\sqrt{\frac{\Gamma}{2}}\hat{\sigma}^-(t - t_0) \tag{2.67}$$

where t_0 is the time it takes for the input mode to reach the atom. This can then be used to solve for the above transmission and reflection coefficients by noting that the expectation operator $\langle\cdots\rangle$ is linear; one can thus write

$$\left\langle \hat{a}^L_{out}\right\rangle = \left\langle \hat{a}^R_{in}\right\rangle + \sqrt{\frac{\Gamma}{2}}\left\langle\hat{\sigma}^-\right\rangle \tag{2.68}$$

As the input field is generally known the only part that is to be determined is $\langle\hat{\sigma}^-\rangle$: the expectation value of the atomic lowering operator. It is given by solving the steady state of the system's master equation and calculating $\mathrm{Tr}\left[\rho\hat{\sigma}^-\right]$. This can be done exactly for a single two level system with decay rate Γ, driving rate Ω and dephasing rate γ_ϕ as detailed in [55]: it has a transmission coefficient given by

$$t = 1 - \eta\frac{\Gamma}{2\Gamma_2}\frac{1 - i\Delta/\Gamma_2}{1 + (\Delta/\Gamma_2)^2 + \Omega^2/\Gamma\Gamma_2} \tag{2.69}$$

where $\Gamma_2 = \frac{\Gamma}{2} + \gamma_\phi$, $\eta = \frac{\gamma_r}{\gamma_{nr}+\gamma_r}$ is the ratio of the radiative losses to the total losses and $\Delta = |\omega_0 - \omega_d|$ is the detuning between the qubit and the driving field. As can be seen, all of the major system parameters are contained in this expression and its measurement will therefore be crucial in characterizing our system.

Another expression of interest is the power spectral density of the system, given by the Fourier transform of the correlation function. In the context of quantum optics it can be derived using the quantum regression theorem to be given by [28]

$$G^{(1)}(\tau) = \left\langle \hat{a}^\dagger(t)\hat{a}(t+\tau)\right\rangle = \mathrm{Tr}\left[\hat{a}e^{\mathcal{L}\tau}\rho(t)\hat{a}^\dagger\right] \tag{2.70}$$

or by its more often employed normalized version

$$g^{(1)}(\tau) = \frac{\langle\hat{a}^\dagger(t)\hat{a}(t+\tau)\rangle}{\langle\hat{a}^\dagger(t)\rangle\langle\hat{a}\rangle} \tag{2.71}$$

In order to solve for this one thus again requires knowledge of the input and output field through input-output theory, as well as of the systems Liouvillian $\mathcal{L}$. Performing the Fourier transform of 2.71 then results in the power spectral density $S(\omega)$, containing information about any incoherent scattering of the system.

While for our complete system this also results in a complicated expression that should be solved with numerical methods, it is again instructive to restrict ourselves to a single two level system. When driving such a system on resonance ($\omega_0 = \omega_d$) the power spectral density is given by the famous Mollow Triplet, an approximate expression for which is given by [55]

$$S(\omega) = \frac{1}{2\pi}\frac{\hbar\omega\Gamma}{8}\left(\frac{\gamma_s}{(\Delta+\Omega)^2+\gamma_s^2} + \frac{2\gamma_c}{\Delta^2+\gamma_c^2} + \frac{\gamma_s}{(\Delta-\Omega)^2+\gamma_s^2}\right) \tag{2.72}$$

where $\gamma_s = (\Gamma + \Gamma_2)/2$ and $\gamma_c = \Gamma_2$. Note that this equation is valid only when the driving rate is strong compared to the loss rate: $\Omega_R^2 \gg \Gamma^2$. While exact expressions can also be derived [28], this specific form highlights that it results in a structure of three peaks separated by Ω. The Mollow triplet is therefore well suited for the determination of the driving rate.

Chapter 3

Design & Fabrication

In the previous chapter we introduced the theory governing transmission lines, resonators and transmon qubits, as well as of their coupling in the geometry illustrated in the circuit diagram of figure 2.5. In this section we now cover the design and fabrication of a chip realizing this geometry: first we discuss the design of chips containing just the waveguides and the resonator, and in a second stage we introduce the design of the qubits and incorporate them into the chip.

In addition to the physical components we also discussed flux noise and its effect on the transmon qubits. We found that ultimately the power spectral density and the probability distribution of the noise are what define the form of the interaction; after establishing the design of the chip we therefore also discuss the design of flux noise with arbitrary power spectral densities and probability distributions that can be applied to our chip.

3.1 Mask Design

We begin with the chip without the qubits. It is important to note that both the design and the fabrication of this chip was done by Dr. Anton Potočnik. We therefore only cover the basics of the process.

The chip design contains a number of elements: a coplanar waveguide transmission line for input and output to qubits 1 and 2, a coplanar waveguide resonator that serves as the output of qubit 3, and two additional elements: two flux bias lines. Essentially a line through which current can flow, their function is to provide a tunable flux source that couples predominantly to the qubits they are closest to. This allows one to tune the transition frequency of a single qubit without strongly perturbing other qubits. In addition to this the flux lines can also be used to generate individual noise environments for each of the qubits.

The design of such a chip is shown in figure 3.1, created using Mathematica. It contains all the aforementioned elements in addition to a qubit box that would contain the qubits, as well as airbridges (shown in red). They are crossover connections made between the ground planes that are interrupted by the structures to equalize potentials, but one has to take care that they do not facilitate the formation of ground loops. Moreover, the CPW resonator is capacitively coupled to the qubit box on one side and to a transmission line on the other side with a designed capacitance C_κ.

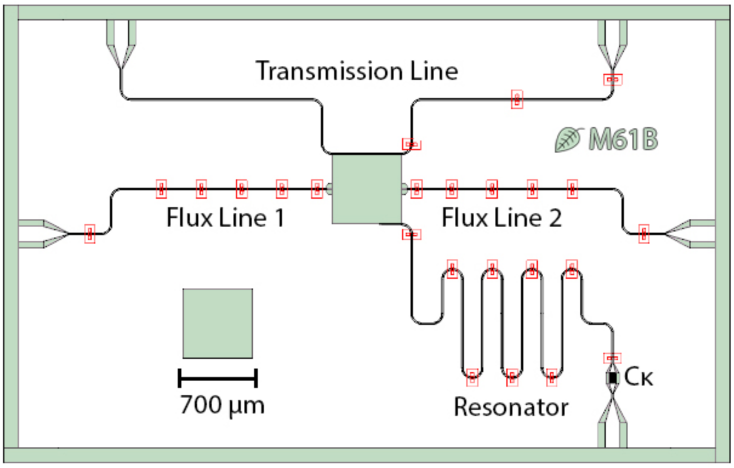

Figure 3.1: The design of the B chips of mask 61. It includes a transmission line, a qubit box, two flux lines, and a resonator with coupling capacitance C_κ. Shown in red are airbridges.

While the fabrication of a chip containing these elements is well established in this group [56], variations still occur between different iterations of fabrication, especially when it comes to the CPW resonator. Its resonance frequency is determined by the length of the CPW as well as its effective permitivity ε_{eff}, while its loss rate κ is mostly determined by the capacitance C_κ [57]. In order to get these quantities in the desired range it is therefore good practice to fabricate a number of chips with slightly different design parameters and choose the best one. This is done on a so called mask; a large wafer containing a number of identical copies of the chips with the different parameters. One then takes a copy of each of these for characterization, after which a remaining copy of the best version is selected for the qubit writing stage.

The chips studied in this thesis were fabricated from such a mask: mask 61. On this mask we only varied the aforementioned resonator properties, its resonance frequency and loss rate, by varying the resonator length and the coupling capacitance respectively. The designed parameters of the chips fabricated onto it are listed in table 3.1 where it should be noted that our aim was to have a fundamental resonance frequency between 5.5 and 6 GHz and a loss rate between 50 and 100 MHz.

Moreover, as denoted in the table the mask contains two types of chips: chips of the form shown in figure 3.1 referred to as the B chips, and well as chips without the qubit box and the flux lines referred to as the A chips. The goal of these chips is to investigate the source of potential cross coupling between the different elements through elimination of intermediate structures. For example, the A1 chip is the reduced version of the B3 chip and A2 is the reduced version of B1.

Chip	f_0 [GHz]	C_κ [fF]	κ [MHz]
A1	5.751	9.5	1.7
A2	5.531	55.2	48
A3	5.360	96.3	127
A4	6.242	9.5	2.1
B1	5.531	55.2	48
B2	6.012	50.1	51
B3	5.751	9.5	2
B4	5.360	96.3	127
B5	5.834	86.0	131

Table 3.1: The variable design parameters of the studied chips of mask 61: the fundamental frequency f_0, the coupling capacitance C_κ and the resulting loss rate κ.

In the fabrication process itself the structures are etched into a layer of niobium on top of a sapphire substrate using a photolithographic process [56] with respective thicknesses of 150 nm and 500 μm. The choice for niobium stems from the fact that it becomes superconducting at $T_c \simeq 8.6$ K, while our experiments are performed at sub liquid helium temperatures. The layer will thus be dissipationless and not contribute to resistance based losses. It is in this superconducting layer that one then constructs the different components by etching away the desired segments. Figure 3.2 shows a microscope image of one of the B chips fabricated in this manner, with the niobium layer shown in white and the underlying sapphire layer visible in green.

3.2 Qubit Design

In contrast to the design of the mask, the design of the qubits themselves was done during this thesis. It proceeded in several steps: first the capacitive pads were designed, governing the charging energies of the qubits E_C as well

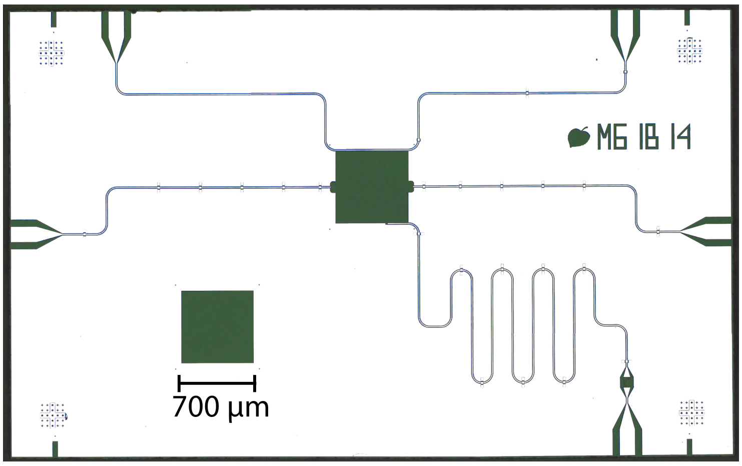

Figure 3.2: A false color microscope image of a fabricated B chip of mask 61.

as the coupling between the different elements such as J_{12} and g_{3r}. In the next stage the SQUIDs were introduced, their position determined based on the coupling to the nearby flux lines. Finally the qubits were fabricated onto the B5 chip discussed in the previous section by Dr. Simone Gasparinetti, with the target E_J based on the desired ω_{eg}. The choice for the B5 chip is motivated in chapter 5, where the characterization of mask 61 is discussed.

3.2.1 Capacitive Design

We begin with the capacitive design, for which an iterative approach was used. First the general design was drawn in Mathematica, after which capacitive simulations were performed with ANSYS Maxwell in order to estimate the different capacitances. These capacitances were then used to determine the different qubit parameters using the quantities derived in appendix B.

More explicitly, we begin with a design based on the geometry of the qubit box. It has a size of 700 by 700 μm etched into the niobium. It is onto this box that we draw the qubit capacitance pads out of Aluminum, which becomes superconducting at $T_c \simeq 1.2$ K, a temperature readily achieved in the experiments performed with the qubits. An example of the design of the pads is shown in figure 3.3, which highlights several considerations. The first of these is the difference between the first two qubits and qubit 3. Qubits 1 and 2 were designed with the possibility of introducing noise environments in mind. They are therefore located close to the flux lines, which are located in the middle of the qubit box themselves. The capacitance pads of qubits 1 and 2 are therefore set up so that one can write a SQUID in the large section of sapphire on the sides of the pads, as close to the flux lines as possible. Moreover, the capacitance pads of qubits 1 and 2 are an exact mirror image so as to make their qubit properties as equal as possible.

For qubit 3 the situation is different; it is designed to have its SQUID situated in the green rectangular area near the bottom center of the qubit box where the influence of the flux lines is expected to be negligible. This necessitates a slightly altered design for the pad of qubit 3, as reflected in the figure. Furthermore even though we use only 3 qubits in our experiments we chose to create a fourth pad in the bottom left corner, again the mirror image of qubit 3. No SQUID loop is to be connected to this pad; its role is to create an equal environment for all of the qubits, essentially achieved by making the capacitance matrix $\underline{C}$ of the qubit system symmetric.

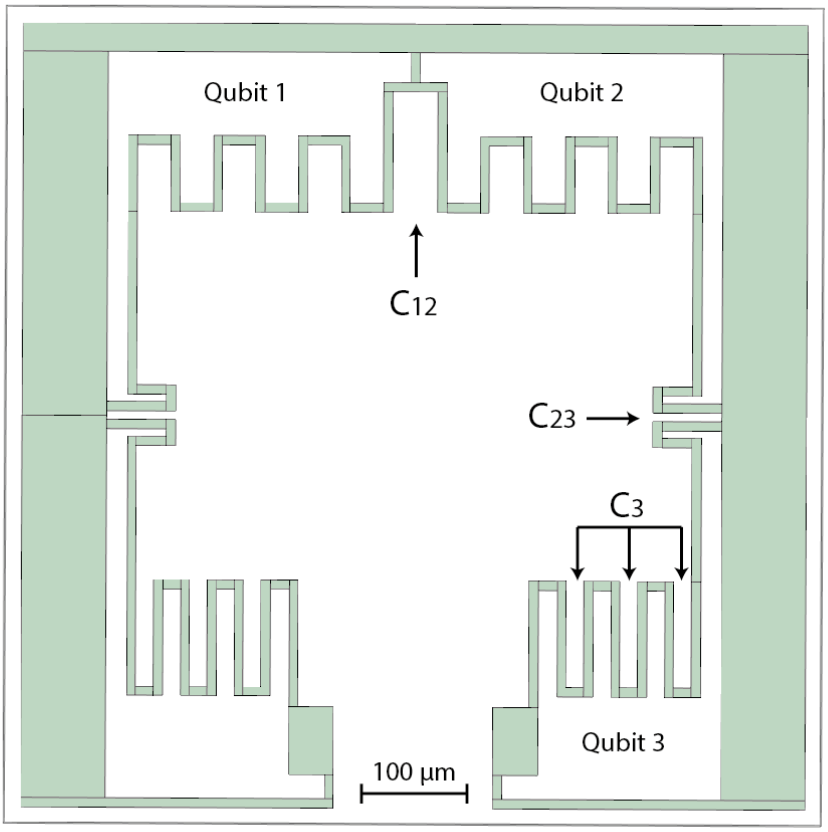

Figure 3.3: The design of the capacitive part of the qubits. Indicated are the gaps that predominantly define the different capacitances.

Figure 3.3 also highlights the features that determine the relevant capacitances. The capacitance pads themselves are periodic structure of multiple fingers, and their capacitance mainly comes from the area between the fingers. As the pad of qubit 3 is less wide than that of qubits 1 and 2 it therefore has longer fingers to compensate and maintain a similar E_C. Similarly, the gaps between the different pads determine the coupling capacitances, which are chosen in accordance with the desired parameter hierarchy.

Once an agreeable design is found we export it as a CAD file and import it into ANSYS Maxwell, where we have set up a section of the B5 chip centered around the qubit box. This is to include the capacitive coupling of the qubits to the transmission line and the resonator. The design is then integrated into the chip as shown in figure 3.4, where the dark areas indicate sapphire, the outer ground plane is niobium, and all other structures are aluminum.

Note that in the simulation we define the imported pads to consist out of a perfect conductor rather than aluminum to mimic its superconductivity. The same is done for the niobium surrounding the qubit box, which is joined with the aluminum into a single ground plane for purposes of calculation. Experimentally this is done by evaporating an overlapping region of aluminum onto the niobium as shown by the transparent section of figure 3.4.

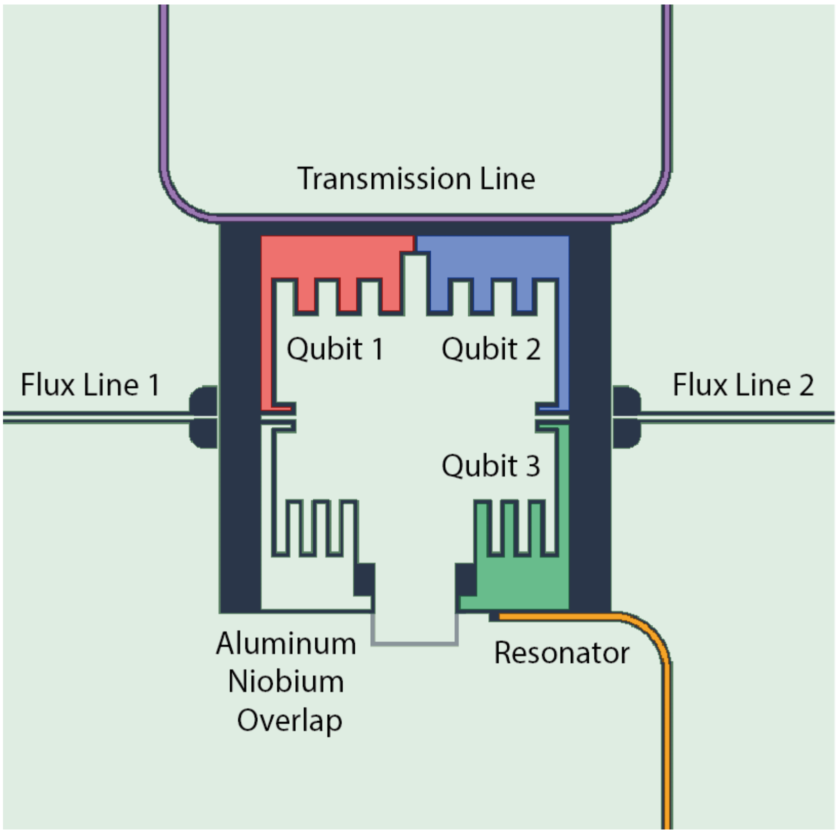

Figure 3.4: The capacitive part of the qubits defined in ANSYS Maxwell. Indicated are the different components of interest, as well as the (transparant) overlap between the aluminum and niobium ground plane.

In the next step we set up Maxwell for electrostatic solutions and assign a distinct excitation to each of the colored regions of figure 3.4. Note that this is also true for the fourth capacitance pad; it is set to a different potential than the ground plane which shares its color. Choosing a suitable number of passes and error percentage, Maxwell then simulates the capacitance matrix of the system consisting of the different sections using increasingly detailed meshes. We then export this matrix, analyze it using a Mathematica script based on the calculations detailed in B with an additional fourth qubit and a fixed E_J. We then look at the resulting Hamiltonian parameter table, and based on which parameters are not in the desired range we return to the initial stage of drawing the pads in Mathematica, make suitable adjustments to the design, and repeat the process until convergence.

3.2.2 Inductive Design

Once the capacitive components have been designed we move on to the inductive stage; the SQUID design. In the first stage we import the finalized capacitive design back into Mathematica and define the outlines of the SQUIDs onto this: we draw segments connecting a 10 by 12 micrometer SQUID box to the respective capacitance pad and the aluminum ground, as shown in figure 3.5a.

For qubit 3 we simply choose the SQUID box to be in the center of its designated segment, but for the positions of SQUID 1 and 2 we again resort to Maxwell, now in its Magnetostatic solution mode. Here we draw the SQUID loop in more detail as shown in figure 3.5b and assign currents to the SQUID and the flux line. From this Maxwell then calculates an inductance matrix, giving us an indication of the mutual inductance between the flux line and the SQUID. We then vary the x and y position of the SQUID box over a range of values and repeat the process, mapping out the inductance space in search for a maximum. Once this has been found we return to Mathematica and fix the SQUIDs of qubits 1 and 2 to these positions, where we found the maximum the be at two thirds of the upper flux line segment. The design of the actual SQUID inside its box is then done by Dr. Simone Gasparinetti based on considerations such as target E_J and flux sensitivity.

3.2.3 Fabrication and Parameter Estimates

The final stage of the qubit design is the fabrication, also done by Dr. Simone Gasparinetti. A detailed overview of the process can be found in [56], but the general concept is that the qubits are made by patterning their structure into a positive resist with electron-beam lithography, after which aluminum is depositied via shadow evaporation. Note that at some stage the evaporation is interrupted by a static oxidation in order to create the aluminum oxide

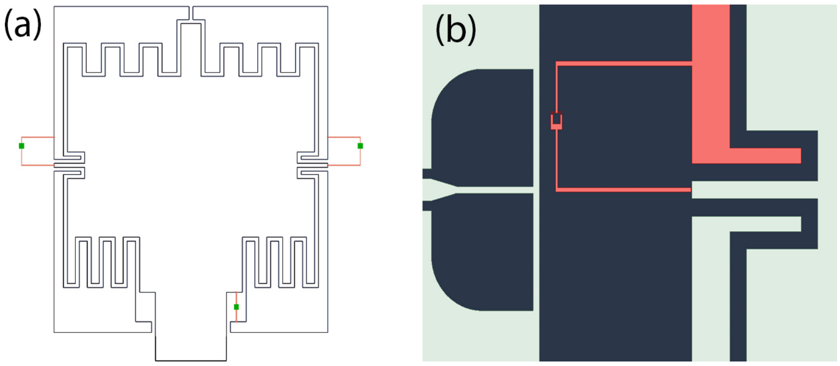

Figure 3.5: SQUID design for the qubits. Panel (a) shows how the general outlines of the SQUID are designed in Mathematica, whereas panel (b) shows how a more precise version of the SQUID can be drawn in Maxwell in order to simulate the mutual inductance with respect to the nearest flux line.

layer, the thickness of which determines the Josephson energy E_J together with the size of the junction [38].

Once all of the qubits have been fabricated onto the chip, it is bonded onto a copper printed circuit board (PCB) using aluminum wirebonds. The PCB itself has SMP jack launchers soldered onto it prior to this, which can be used to connect the necessary electronics to the PCB discussed in chapter 4.

The sample resulting from the above process is shown in figure 3.6; it is the main object of study in this thesis. Panel a shows the chip in its entirety, with the transmission line in purple connected to ports 1 and 2, flux line 1 in yellow connected to port 3, the CPW resonator in orange connected to port 4 and flux line 2 in pink connected to port 5. Panel b shows a zoom in of the qubit box itself, containing qubit 1 in red, qubit 2 in blue and qubit 3 in green.

While the exact properties of the sample are characterized in chapter 5, we can already formulate an estimate of the Hamiltonian parameters based on the simulated capacitances and the target qubit frequencies. These estimates are listed on table 3.2, and are in line with the parameters aimed for based on the proposal of Mostame *et al.* [20]. The only exception to this is J_{13}; ideally it would be equal to zero so that the bright and dark mode couple to the third qubit equally (see equation 2.35) but we could not reduce it below the simulated value without changing the size of the qubit box, which was unpractical given that the mask had already been fabricated prior to the qubit design.

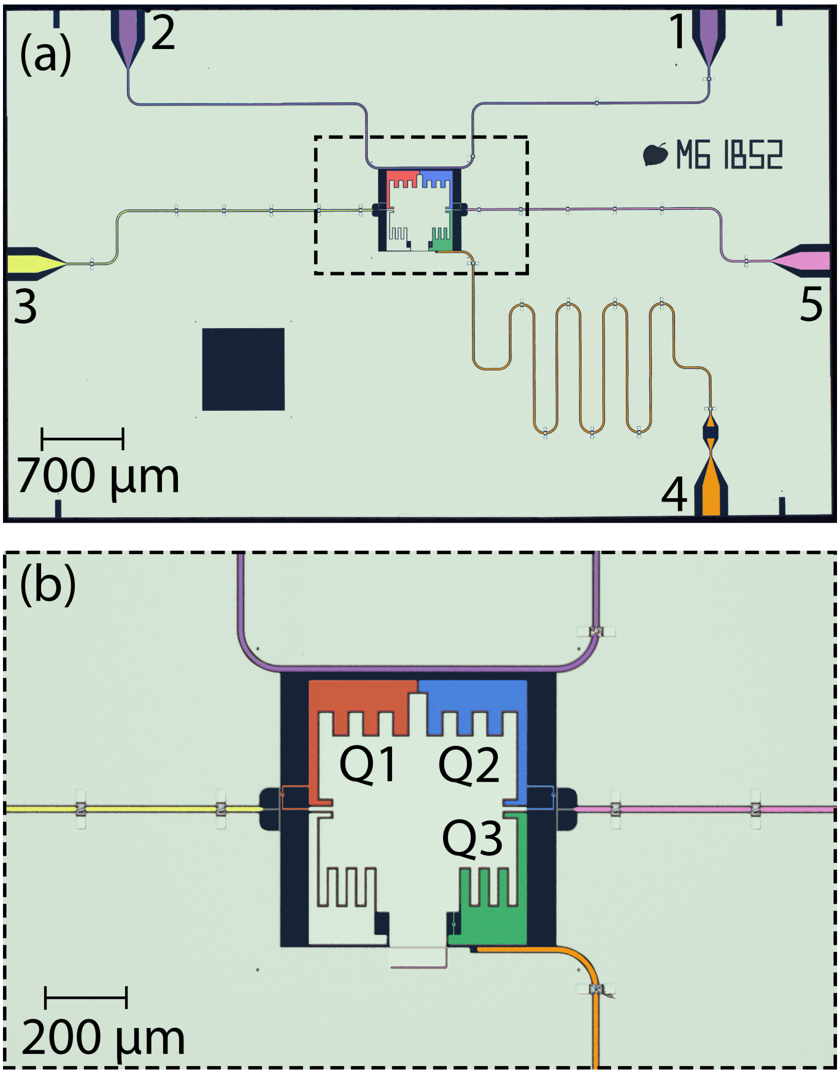

Figure 3.6: A false color microscope image of the sample used for the experiments in this thesis. Panel (a) shows the overall chip containing the transmission line, the two flux lines, the resonator and the qubits, while panel (b) offers a zoomed in picture of the qubit box.

3.3 Flux Noise Design

Now that we have covered the design and fabrication of the physical object of interest, we discuss how to generate the noise environment of the qubits. In chapter 2 we defined the qubit environment to be given by the magnetic flux $\Phi(t)$ in the form of in the form of a static working point value plus a small fluctuating contribution: $\Phi(t) = \Phi + \delta\Phi(t)$. Moreover, we defined this small fluctuation contribution to be the noise; its power spectral density and

Parameter	Designed value/$2\pi^*$
E_{C1}	121 MHz
E_{C2}	120 MHz
E_{C3}	121 MHz
$E_{J\{1,2,3\}}$	50 GHz
$\omega_{\{1,2,3\}}$	6.8 GHz
ω_r	5.834 GHz
J_{12}	120 MHz
J_{13}	3.7 MHz
J_{23}	38 MHz
g_{1r}	200 kHz
g_{2r}	1.4 MHz
g_{3r}	110 MHz

Table 3.2: Designed Hamiltonian parameters for all three qubits and the resonator, in addition to the designed E_C and E_J. Note that the reported values of E_C and E_J are not divided by 2π, as indicated by the asterisk.

probability distribution fully described the effect of the noise environment on the transmon qubits.

In this section we briefly describe how to design and physically implement a general flux noise term of the above form with an arbitrary power spectral density and probability distribution; the exact details of the process can be found in appendix C.

3.3.1 Digitally Generating Noise

As discussed in the appendix, we start the noise design by generating a discrete digital time series $y[t]$ with arbitrary power spectral density $S(f) = A(f)$. This is done by first generating white noise $x[t]$ with unit power spectral density $S(f) = 1$ by independently drawing from the Gaussian distribution with zero mean and unit standard deviation, which we then subsequently subject to the linear mapping of a filter with the transfer function $H(f) = \sqrt{A(f)}$ resulting in $S_Y(f) = A(f)$.

To illustrate the generation of noise with an arbitrary spectral density we generate and analyze the two different noise series studied in this thesis: white noise with a high frequency cutoff and noise with a Lorentzian power spectral density. The first has a power spectral density given by

$$S_X(f) = \frac{a}{1 + e^{\frac{f-b}{c}}} \tag{3.1}$$

which is a generalized version of the Fermi Dirac distribution. For the proper choice of parameters, it is essentially white noise of amplitude a up to an exponential cutoff at $f = b$ with steepness c. The reason for its finite bandwidth is that, as briefly noted in appendix C, infinite bandwidth white noise does not exist in nature; this would contain infinite energy. We therefore have to cut it off at some frequency, which we choose such that the noise covers all the relevant energy mismatches explored in our experiments. Moreover, we choose the Fermi-Dirac distribution (rather than for example a step function) due to its closed form expression and smooth properties.

We combine this power spectral density with the filtering method discussed in appendix A to generate a time series of length $n = 16 \times 10^6$ using $m = 2000$ impulse response function amplitudes $h[t]$, for which we set $a = 0.1$ V^2/Hz, $b = 400$ MHz, and $c = 10.8$ MHz. This corresponds to noise with a flat spectrum up to 350 MHz, dropping down to below 1% of a at 450 MHz. As shown in figure 3.7a this spectrum is reproduced with better than 1% accuracy in a subsequent fit, where we estimated the power spectral density of the time series using Welch's method, which is a windowed and averaged periodogram [58].

The second time series we generate has a Lorentzian power spectral density centered at some specific frequency. Its power spectral density is given by

$$S_X(f) = \frac{a}{1 + \left(\frac{f-b}{c}\right)^2} \tag{3.2}$$

which is a Lorentzian function of maximum amplitude a centered at frequency b with a full width at half maximum of $2c$. This type of power spectral density is studied in the context of the phonon antenna mechanism introduced in chapter 1. Figure 3.7b illustrates that this spectrum is also readily produced; the input parameters $a = 0.1$ V^2/Hz, $b = 100$ MHz and $c = 2$ MHz are again reproduced with better than 1% accuracy.

Note that the above power spectral densities are digital; the units reported are thus arbitrary. However we chose them in anticipation of the physical implementation of the noise, which is the subject of the next section.

3.3.2 Digital to Analog Conversion

As written at above, the digitally generated noise is now physically implemented. As discussed in appendix C, it takes the form of a voltage $U(t)$ with a power spectral density $S_U(f)$ and probability distribution $f_U(u)$ equal to that of the random variable X, and it is generated with an arbitrary waveform generator (AWG).

Figure 3.8(a) shows the power spectral density of a sample implementation of this: we digitally generated a Gaussian distributed time series with its

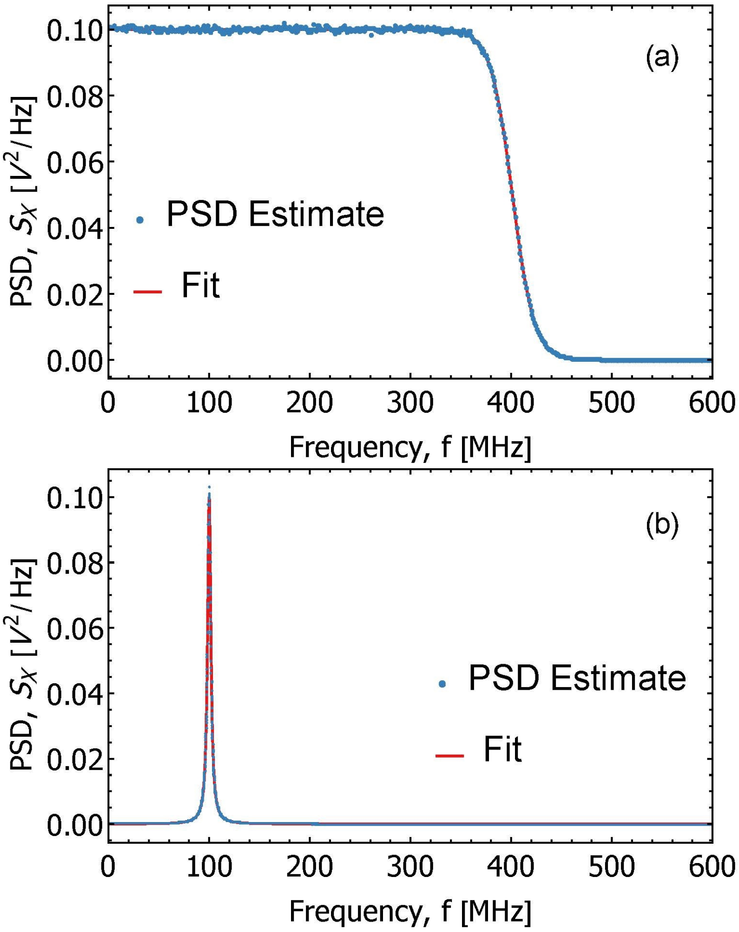

Figure 3.7: (a) The digitally generated time series with a Fermi-Dirac power spectral density, flat up to 350 MHz and exponentially decaying to zero at 450 MHz. (b) The digitally generated time series with a Lorentzian power spectral density with a center frequency of 100 MHz and a full width at half maximum of 4 MHz.

power spectral density governed by the Fermi Dirac distribution of equation 3.1, with $a = 0.1\ \mathrm{V}^2/\mathrm{Hz}$, $b = 325$ MHz, and $c = 5.44$ MHz; note that these parameters are different than the ones used for the digital white noise discussed above. We then exported this pattern to the AWG and measured its output with a spectrum analyzer, the result of which is shown in the figure along with a fit with equation 3.1.

From the figure we see that the recipe is effective in producing a spectrum with better than 1dBm flatness over the bandwidth of the signal; quantitatively we find that it reproduces the parameters with 99.8, 99.7 and 90% accuracy respectively. The fact that the exponential cutoff parameter is less accurate can be explained by the fact that it is very sensitive to small deviations.

However, based on figure 3.8(a), the cutoff is still implemented in a satisfactory fashion. Figure 3.8(b) shows a similar measurement for voltage noise with a Lorentzian power spectral density with amplitude $a = 0.1$ V^2/Hz, center frequency $b = 185$ MHz and full width half maximum $2c = 10$ MHz, where all three parameters were reproduced with better than 1% accuracy.

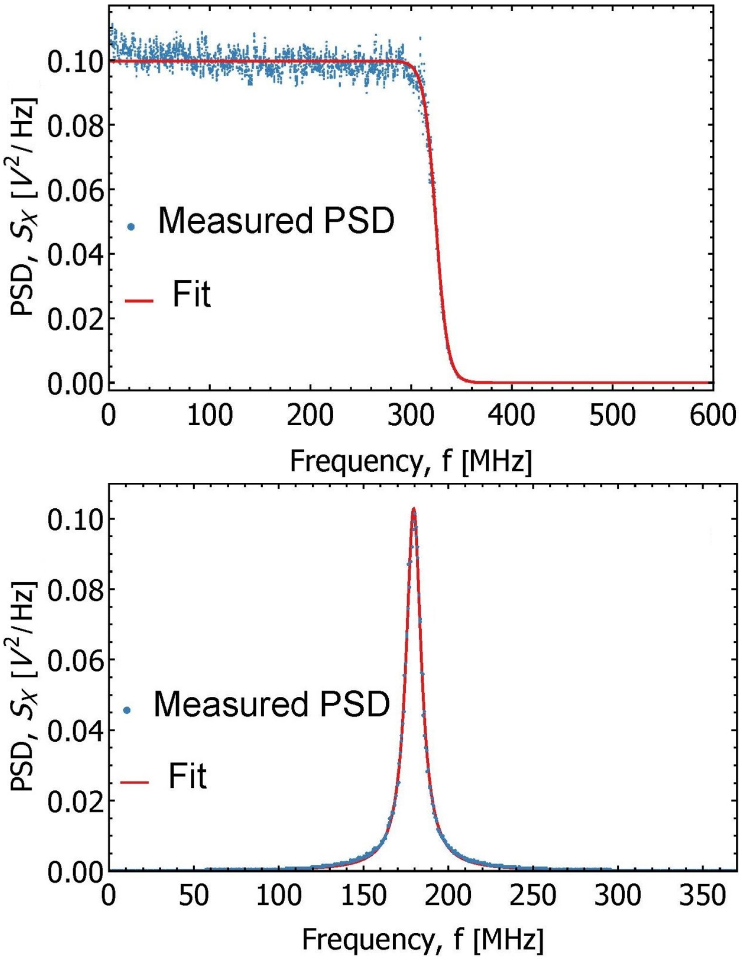

Figure 3.8: (a) The power spectral density of the generated white voltage noise as estimated by the spectrum analyzer, fit with equation 3.1. (b) The power spectral density of the generated white Lorentzian power spectral density voltage noise as estimated by the spectrum analyzer, fit with equation 3.2.

3.3.3 Voltage to Flux

The final step that remains is converting the generated voltage noise signal into a magnetic flux signal, and in turn relating $S_U(f)$ to $S_\Phi(f)$. In order to do so we send the voltage noise into the lines connected to the sample's flux lines (as treated in chapter 4), where the voltage passes through a series of attenuators. The attenuators cause a total voltage drop given by $\alpha = \Pi_{i=1}^{n-1}\alpha_i$ where α_i is the (voltage) attenuation of the ith attenuator. Rather than attenuating, the final (nth) attenuator in the chain effectively acts as a resistor R, resulting in a current I in accordance with Ohm's law. This current then ultimately passes through the flux line on the sample itself, resulting in a magnetic field $B(r) = g\frac{\mu_0 I}{2\pi r}$ where μ_0 is the magnetic permeability of free space, r is the radial distance from the flux line and g is a geometric factor close to 1. Finally, the magnetic field is related to the flux by $\Phi = BA\cos\theta$ where A is the area of the relevant surface (the SQUIDs) and θ is the angle between the magnetic field lines and the normal to the relevant surface. We combine all of these factors into a generalized mutual inductance M, which relates the voltage and the flux: $\Phi = MV$.

The above thus tells us that the relationship between the voltage U and the flux Φ is linear, given by

$$\Phi = \frac{\alpha g \mu_0 A \cos\theta}{2\pi r R} U = MU \tag{3.3}$$

If one assumes that these parameters are not subject to any significant fluctuations and have a flat frequency response, then there is also a linear relationship between $S_U(f)$ and $S_\Phi(f)$:

$$\begin{aligned} S_\Phi(f) &= \int_0^\infty dt\, \langle \Phi(0)\Phi(t)\rangle \cos(ft) && (3.4)\\ &= M^2 \int_0^\infty dt\, \langle U(0)U(t)\rangle \cos(ft) && (3.5)\\ &= M^2 S_U(f)\,. && (3.6) \end{aligned}$$

With this we have thus established how to generate flux noise in a specific flux line with an arbitrary power spectral density $S_\Phi(f)$.

Chapter 4

Experimental Setup

In this thesis we use several important experimental tools and techniques to characterize and measure our sample of interest. In the first stages of the experiments we used a so called dipstick submerged into liquid helium connected to a vector network analyzer (VNA) in order to characterize the mask the qubits were to be printed on. Conversely, the advanced measurements and characterization was done in a dilution refrigerator, providing the electrical and thermal environment of the sample. Instead of a VNA, the dilution refrigerator was connected to a more involved signal processing chain where the fields output by the sample were measured and processed consisting of down conversion, amplification and a field programmable gate array (FPGA). In this chapter we provide an overview of each of these tools to give insight into the measurement techniques used in chapters 5 and 6.

4.1 Dipstick Setup

As written above, the first stages of the experiments were performed using dipstick measurements; submerging the chip into a liquid helium dewar to cool them down to 4.2 K, which is below the chip's critical temperature for superconductivity T_c. At these temperatures one can then probe the properties of the chip using input-output theory. To do so, the chips themselves were individually placed onto the dipstick, and the other side of the dipstick was connected to the VNA using SMP connectors. The VNA then measured the relevant scattering parameters, such as the reflection and transmission coefficients introduced in chapter 2.

Different steps have to be taken in order to measure with the dipstick setup. To begin with one performs a calibration of the VNA and the SMP cables connected to the dipstick by connecting them only to the dipstick with no chip placed onto it. This is done to calibrate out any distortions caused by the cables. As the VNA has four ports while the chips used in this report have up to 5 relevant connections, one has to choose which scattering parameters are most relevant and connect the cables according to this, or instead perform several calibrations with the cables connected in different configurations. During the measurements the connectors of the chip that were not connected to the VNA were terminated with 50 Ω at room temperature.

The calibration of the VNA is done manually, using a specifically designed calibration kit containing four components: a short, a load, an open and a through connector. Guided by the VNA, one connects these components to the corresponding cable port on the dipstick one by one, after which the VNA gathers statistics for its calibration settings. It is important to note that the calibration is done at room temperature and not at liquid helium temperature, as one constantly has to change the calibration components on the bottom of the dipstick which would otherwise be submerged in the helium.

One should carefully pick the relevant measurement parameters of the VNA before performing the calibration, as changing them at a later stage might render the calibration invalid. The parameters used for calibration and measurement in this report are listed in table 4.1. Moreover, the calibration was done using the 'Qudev female connector' settings found on the VNA in the Quantum Device lab the thesis was performed in.

Parameter:	Setting:
Power	-8 dBm
IF Bandwidth	50 kHz
No. of Averages	40
No. of Points	6000
Frequency Range	1 GHz to 14 GHz

Table 4.1: VNA settings used for the calibration process.

Once the calibration has been completed, one can mount the chip and begin the submerging procedure. The dipstick is slowly placed into the helium dewar, continuously monitoring the pressure. While initially the pressure will vary only slightly, there is a certain point at which it increases much more rapidly. For safety reasons it is crucial to wait for the the pressure to drop before submerging the dipstick any further. Once the chip is sufficiently cooled down, superconductivity will occur and for example resonances of the resonator on the chip will become visible on the VNA. After this occurs one should still lower the device several centimeters further in order for the temperature of the device to equilibrate.

After completion of the submerging procedure one can start to operate the

VNA. As discussed in chapter 3 we expect the fundamental mode of the resonator around 5.5 GHz, and so the initial frequency range of 1 GHz to 14 GHz will contain this mode as well as one or more integer multiple modes. While at this stage all scattering parameters can already be viewed and exported, we also choose a subset of these resonances to zoom in on to capture in more detail. At this stage no further signal processing has to be done, as it is all performed internally by the VNA. When the relevant frequency ranges have been explored and exported, the measurement is completed and one can slowly take the dipstick out of the dewar again.

4.2 Cryogenic Setup

The more advanced experiments were performed in a cryostat, more specifically a dilution refrigerator. Essential to the operation of many experiments in the circuit QED architecture, it facilitates performing low temperature experiments where not only superconductivity needs to be achieved but thermal populations should also be strongly reduced in order to improve lifetimes and coherence rates of the quantum mechanical components. In addition to that the cryostat provides a large degree of shielding from the environment, reducing the influence of electromagnetic fields in the vicinity of the system. In these conditions the quantum properties of the circuits dominate and are well measurable, setting the stage for our experiments.

The specific dilution refigerator used in these experiments is the BlueFors BF-LD250 cryogen-free dilution refrigerator system, nicknamed the BlueFors1 in this lab. It can achieve temperatures as low as 10 mK using the heat of mixing of the two Helium isotopes, ^{3}He and ^{4}He. While the exact principles governing this mixing are beyond the scope of this thesis and can be found in [59], the basic concept is based on the fact that ^{4}He undergoes a phase transition from a normal fluid to a superfluid at 2.7 K, and that this temperature decreases when ^{4}He is mixed with ^{3}He. Below a certain temperature this mixture will then separate into two phases (a ^{3}He rich and poor phase known as the concentrated and the dilute phases), where at low temperatures the enthalpy of the latter is larger than of the former. Moving ^{3}He from the concentrated phase to the dilute phase therefore requires energy, cooling down the system to these low temperatures of around 10 mK. Before the above process begins the system first has to be precooled to 4.2 K temperatures, which is traditionally done by surrounding the cryostat by liquid ^{4}He which has to be refilled periodically. Instead of the above the Bluefors 1 utilizes a pulse tube system that delivers these initial low enough temperatures in such a way that the the cryogen handling circuit is closed, hence the name cryogen free.

However, in order to probe the system and measure its response it has to be connected to room temperature electronics (such as microwave generators) without compromising the cold environment of the chip. This is achieved by the cryostat having several temperature stages, slowly leading the lines through which the initially room temperature signals travel to the 10 mK stage. The Bluefors 1 has six such stages: the 300 K room temperature stage, the 70 K stage, the 4 K stage, the 1 K still stage, the 100 mK stage and finally the 10 mK base stage. The last four of these stages are depicted in figure 4.1, which shows the inside of the cryostat without its lower shields.

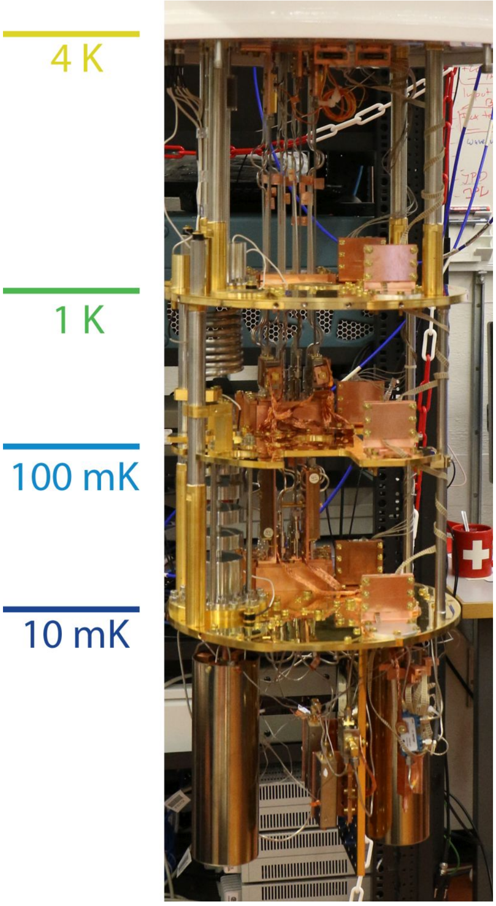

Figure 4.1: Photograph of a part of the inside of the Bluefors1 cryostat. The visible temperature stages are indicated.

As broadly visible in figure 4.1 the different stages contain various components, each of which plays their own role in sending and receiving signals from and to the chip located in the bottom stage. A more detailed picture of these components is given in figure 4.2, showing a diagram of the relevant lines running through the cryostat along with their port numbers on top of the cryostat. Moreover, each line is connected to a specific port of the chip and therefore has its own role; for example, line 8 provides the input modes for the transmission line, line 10 provides a flux for flux line 1, and line 2 contains the modes output by the resonator. The right most line is different from the others; it consists of superconducting DC wires in a twisted pair configuration, connected to a small superconducting coil connected to the bottom of the sample holder. Its role is to provide a global flux that couples to each qubit with roughly equal strength, allowing one to tune their resonance frequencies as detailed in chapter 2.

Looking at the lines in more detail from left to right, line 12 serves as a resonator input line. It is attenuated by 20 dB at three different stages in order to suppress the thermal population of the previous stage, making sure that only a small fraction of the room temperature thermal photons arrives at the sample. It is set up so that one can measure the resonator in reflection; a circulator at the base stage (offering 20dB isolation in the unwanted direction) sends the photons into the resonator, from which the output is routed into cable 2, the resonator output line. Here one has two isolators (consisting of 50 Ohm terminated circulators) at the base stage in order to suppress any photons coming back to the sample from the output line, and higher up one has a high-electron-mobility-transitor (HEMT). Essentially a high gain low noise amplifier that can operate at 4 K, the HEMT amplifies the signal coming from the resonator with 30 to 40 dB gain.

One then has two identical lines, 10 and 11, which serve to provide the flux for flux lines 1 and 2 respectively. They each contain a total of 23 dB attenuation of which the last 3 dB essentially serves as a resistor, transforming the input voltage into a current. In addition to this they have two low pass filters, allowing only DC to 780 MHz radiation to pass which serves to suppress potential flux noise at the qubit frequencies. One then has line 4, serving as the transmission line output. Similar to the resonator output line, it again contains a number of isolators and a HEMT. However, it also contains a 4 to 8 GHz bandpass filter which serves to suppress noise outside of the band of interest which would otherwise contribute to compressing the amplifier. Note that this argument would also apply to the resonator output line, but that this line was designed to function over a larger frequency range. The next line is line 8, the transmission line input. It is essentially identical to the resonator input line (line 12) containing a total of 60 dB attenuation to suppress the thermal population reaching the sample. Finally there is the aforementioned superconducting coil which contains a finite resistance low pass filter similar to the flux lines, which again serves to convert an input voltage into a current while suppressing noise at the qubit transition frequencies.

4.2.1 Room Temperature Components

While the previous section covered how signals are routed in and out of the cryogenic system, we have not covered what occurs at the room temperature stage. We begin with the signals input into the transmission line and the resonator: set up identically, lines 8 and 12 are simply connected to a (room temperature) Rhode-Schwartz SGS100A microwave generator that generates the coherent microwave signal input into the sample, known as the RF signal.[1] The output of lines 2 and 4 is handled in a more complex manner: as shown in figure 4.3a the output of these lines first enters an amplification board at room temperature before entering a down conversion board containing a mixer; the details of these two components are omitted for brevity.

While the amplification board increases the amplitude of the output signal further, the down conversion board is more complicated. It functions as a method of transferring the RF signal information from its carrier frequency to a fixed intermediate frequency (known as IF) while preserving phase and amplitude information. This is done so that subsequent signal processing equipment does not have to be designed to operate at the RF frequencies but instead can function in a fixed regime. In order to facilitate this mixing one requires a so called local oscillator (LO) input into the mixer alongside the RF signal, whose frequency is at a fixed distance of the RF such that $f_{IF} = |f_{RF} - f_{LO}|$. For the LO we use another Rhode-Schwartz SGS100A microwave generator, and unless stated otherwise we set it up so that $f_{IF} =$ 250 MHz. The IF signal is then routed into an analog to digital converters (ADC), after which it is fed into the Virtex 6 field programmable gate array (FPGA) for digital signal processing.

The details of the signal processing itself are rather involved and can be found in [60, 61]. Important for this thesis is that the Virtex 6 has a sampling rate of 1000 MHz and thus a Nyquist frequency of 500 MHz, meaning that it can record signals with a bandwidth of 500 MHz. When $f_{IF} = 250$ MHz the FPGA thus records a 250 MHz bandwidth around f_{IF}. The FPGA can then use a number of 'signal math' settings in order to calculate several statistical moments of the data $S(\tau)$ such as its amplitude $\langle S(\tau)\rangle$ and its autocovariance function $\langle S(0)^* S(\tau)\rangle$ from which quantities such as the reflection coefficient and the power spectral density can be calculated. Finally one has to note that in the setup used in this thesis only one mixer output is used, which causes the resulting IF signal to be symmetric around f_{IF}. Signals at $f = f_{IF} \pm \delta$ therefore cannot be distinguished.

One problem that one runs into with the above setup is that while it can be used to faithfully determine the amplitude of the signal output by the

---

[1] In our experiments only one pair of input and output lines was connected at the same time as they were not needed simultaneously.

sample, its phase shift cannot be. One can understand this by noting that the system only determines the phase of the signal output by the cryostat ϕ_{out}, whereas the phase difference accreditable to the sample $\Delta\phi = \phi_{in} - \phi_{out}$ also requires knowledge of the phase of the RF signal entering the cryostat ϕ_{in}. To circumvent this one can use a phase reference, which is essentially a branch of the input RF signal that does not traverse the cryostat. As shown in figure 4.3b this is accomplished by splitting the initial RF signal into two branches, one of which goes into the cryostat as mentioned above while the other is simply attenuated down to a level similar to the overall attenuation of the entire cryostat-sample system. Both branches then undergo their own warm amplification and down conversion, after which the FPGA performs the necessary signal processing in order to obtain $\Delta\phi$. Note that in this step the two signals are multiplied, essentially lowering the signals amplitude by its square and thus lowering the signal to noise ratio. We therefore only utilize the phase reference in the scenario's where the phase is essential, which is mentioned explicitly in the text.

The final room temperature components are the inputs of the two flux lines and the superconducting coil. Each of these is connected to a Stanford Research Systems voltage source (denoted by SRS), providing a DC voltage that can be related to a static flux at the sample used to vary the qubit transition frequency. While for the superconducting coil this DC voltage is directly connected to the DC wires shown in figure 4.2, the setup for the two flux lines is more complicated.

As discussed in chapters 2 and 3 we are interested in creating a noise environment for the qubits through their flux, related to the voltage applied to the flux lines. In order to do so we combine the voltage noise signal generated by a Tektronix AWG5000 arbitrary waveform generator (AWG) with the DC voltage in a bias tee. The bias tees used are specifically designed to have a relatively low lower end frequency cutoff of 3 kHz so as to not spoil the potential low frequency features of the noise. Moreover we intend to vary its amplitude in two distinct ways: we can tune the amplitude over a moderate range in small steps using the output amplitude of the AWG, and over a larger but more coarse range using attenuators, for which we attenuate the AWG output signal by switching between 3 dB or 8 dB.

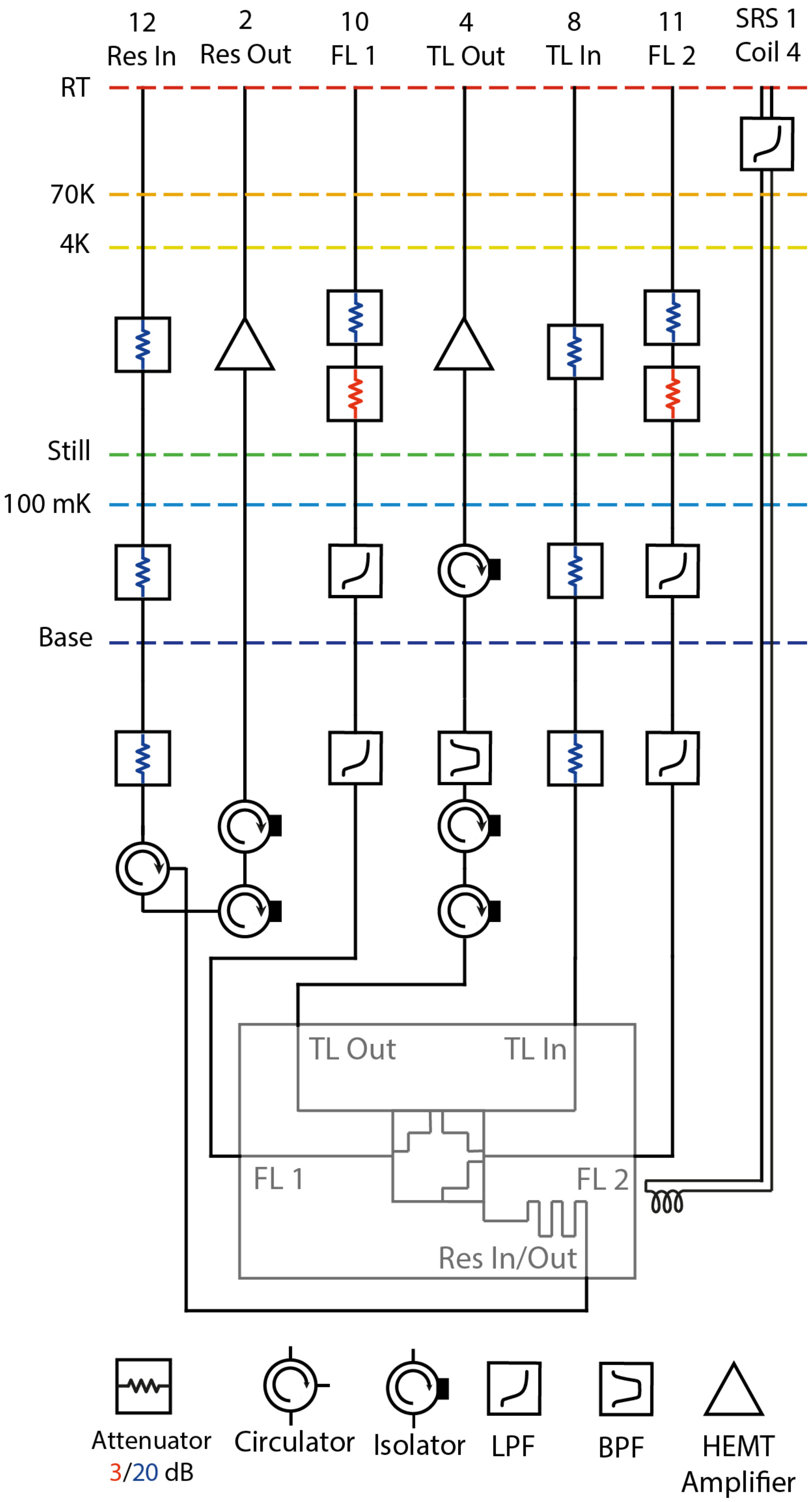

Figure 4.2: Cabling diagram of the lines used for the experiments in this thesis.

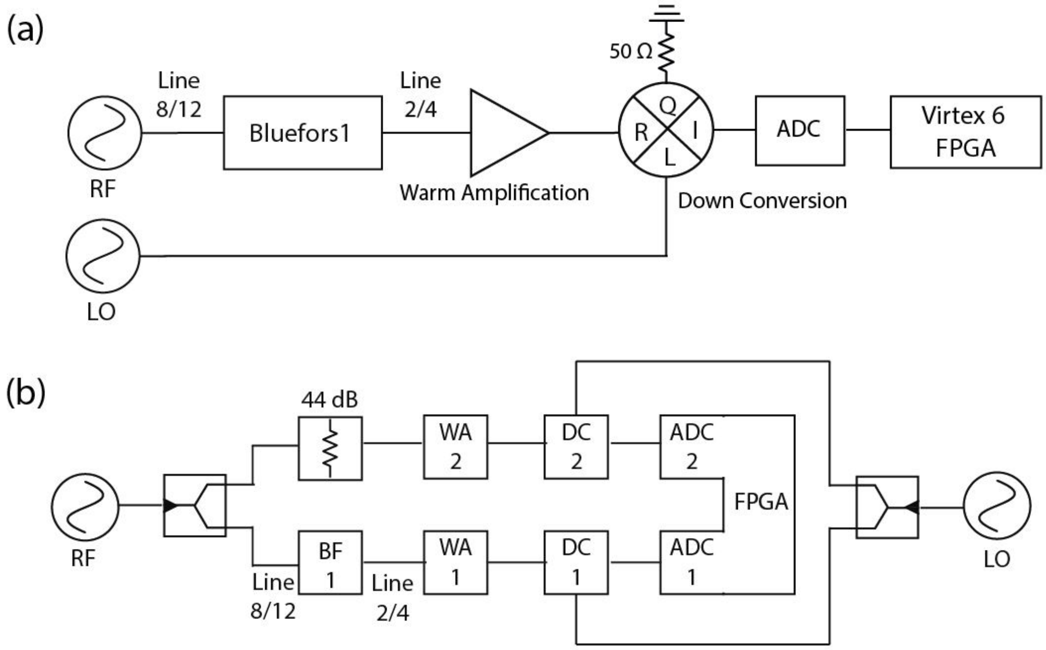

Figure 4.3: Schematic depiction of the input and output microwave signals and their subsequent routing through room temperature components. Panel a shows how the output signal is amplified, down converted and then input into the FPGA where it is amplitude is processed, whereas panel b shows how the previous scheme can be adapted to include phase information in addition to the amplitude.

Chapter 5

Characterization of the System

We have now covered the design and fabrication of the sample of interest (chapter 3) as well as how to connect it to the relevant setup to enable measurement of its behavior (chapter 4). However, at this stage the sample essentially functions as a black box; while we know the type of components it is made out of and how they interact, their exact properties (introduced in chapter 2 are not known. In this chapter we therefore aim to characterize these properties.

Chronologically this characterization occurred in two steps: we first characterized the properties of mask 61 using dipstick measurements as discussed in section 5.1. Based on this we chose what chip to fabricate the qubits on, and thus chip was then characterized in the Bluefors setup as discussed in section 5.2.

5.1 Mask 61

We begin with the characterize the chips of mask 61. As discussed in chapter 3 the mask contains two types of chips: the A and the B chips. Shown again in figure 5.1 for convenience, the B chips contain the transmission line, both flux lines, the resonator and the qubit box. The A chips are a reduced version of the above, containing only the resonator and the transmission line in order for us to study the effect of the absence or presence of the different elements. In addition to this distinction between the two types we also vary two parameters in the individual chips, being the resonator frequency and its loss rate. Varied through the resonator length l and the coupling C_κ, characterizing these quantities was the main goal of this study; based on its outcome we decided which B chip was most suited to fabricate the qubits onto.

In order to perform the characterization of the chips we employ the dip-

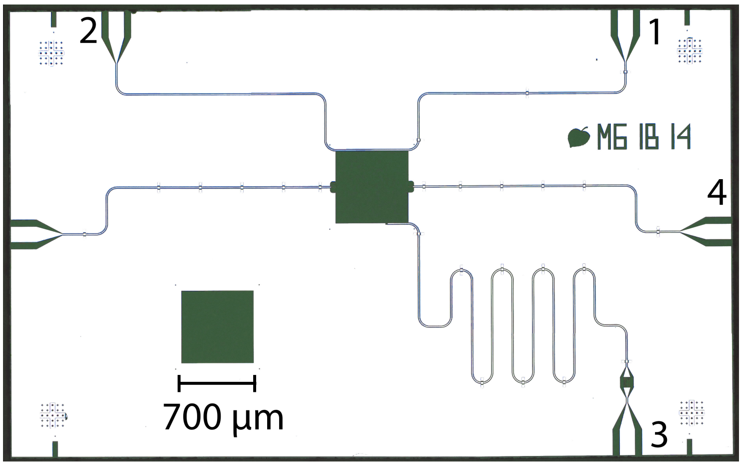

Figure 5.1: False color microscope image of a B chip of mask 61 with the port numbers indicating how the different VNA ports were connected.

stick setup detailed in chapter 4, connecting the 4 available VNA ports as shown in 5.1 and operating the VNA using the settings detailed in table 4.1. The VNA is then used to obtain the scattering parameters of the system S_{xy}, containing the information about the aforementioned resonance frequencies and coupling of the resonator. We extract these parameters using a Lorentzian lineshape model developed for transmission line resonators [62]. It directly fits the scattering parameters with a fundamental resonance frequency f_0 as well as loaded and external quality factors Q_L and Q_E. In turn these parameters tell us about the internal quality factor Q_I through $\frac{1}{Q_L} = \frac{1}{Q_I} + \frac{1}{Q_E}$ and the loss rate of the resonator given by $\kappa = \frac{f_0}{Q_L}$. Depending on whether we measure in transmission or reflection, the exact form of the Lorentzian is given by

$$S_{11} = 1 - \frac{Q_L/Q_E e^{i\phi}}{1 + 2iQ_L\frac{f-f_0}{f_0}} \tag{5.1}$$

$$S_{21} = \frac{Q_L/Q_E e^{i\phi}}{1 + 2iQ_L\frac{f-f_0}{f_0}} \tag{5.2}$$

where the angle ϕ accounts for a potential asymmetry in the lineshape as detailed in [62].

5.1.1 Resonator Spectra

With the above we now discuss the measured spectra of the resonators. To begin we look at the absolute reflection parameters obtained from measuring the resonator of the B32 chip; $|S_{33}(f)|$. Shown in figure 5.2, we can observe the reflection parameter over the full frequency range that was calibrated. We observe two resonances: one at 5.5 GHz and another at the first integer multiple of the fundamental frequency, 11 GHz. Note that there are also some unexpected features in the reflection spectrum; these features originate from the fact that the VNA is not calibrated with the sample placed onto the dipstick, as they can also be seen at room temperature. However, they cannot be fully taken out using a high temperature data set as their exact features are slightly altered by temperature; we therefore ignore them as they do not hinder the characterization.

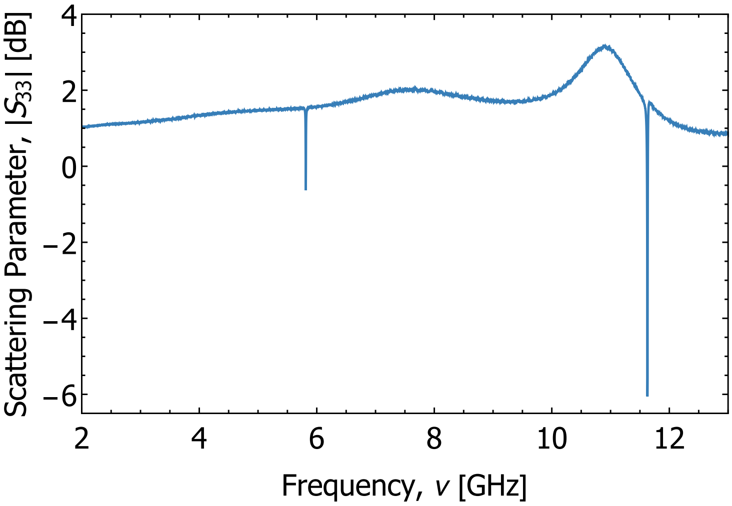

Figure 5.2: The reflection spectrum of the resonator of the B32 chip over the full calibrated frequency range.

We subsequently investigated the resonances in more detail by zooming in on the relevant frequency ranges as shown in the two panels of figure 5.3. Plotted over the data (blue) is the fitted Lorentzian lineshape of equation 5.1 (red). From these fits we extract that the exact resonance frequencies are given by $f_0 = 5.814$ GHz and $f_1 = 11.63$ GHz, with linewidths $\kappa_0 = 6.051$ MHz and $\kappa_1 = 11.99$ MHz respectively.

The measured values for the fundamental mode of all of the other the other A and B chips are listed in table 5.1, as this is the mode the relevant mode for our chip. While the fundamental frequency of all the designed A chips is within 1% of the designed value, the B chips are up to 3% higher than designed. The direct comparison between the A11 and the B32 chip gives some insight into this: we see that the fundamental frequency of the B32 resonator is around 15 MHz higher than the fundamental frequency of the A11 chip, while both resonators are fabricated using the same design parameters. As the A11 chip does not contain the qubit box and the flux lines we therefore attribute the frequency shift to the fact that the qubit box lowers the effective capacitance of the resonator. Larger discrepancies can be seen between the designed and measured κ_0, which has been attributed to the fact that the computation of κ_0 from the designed C_κ can still be further refined.

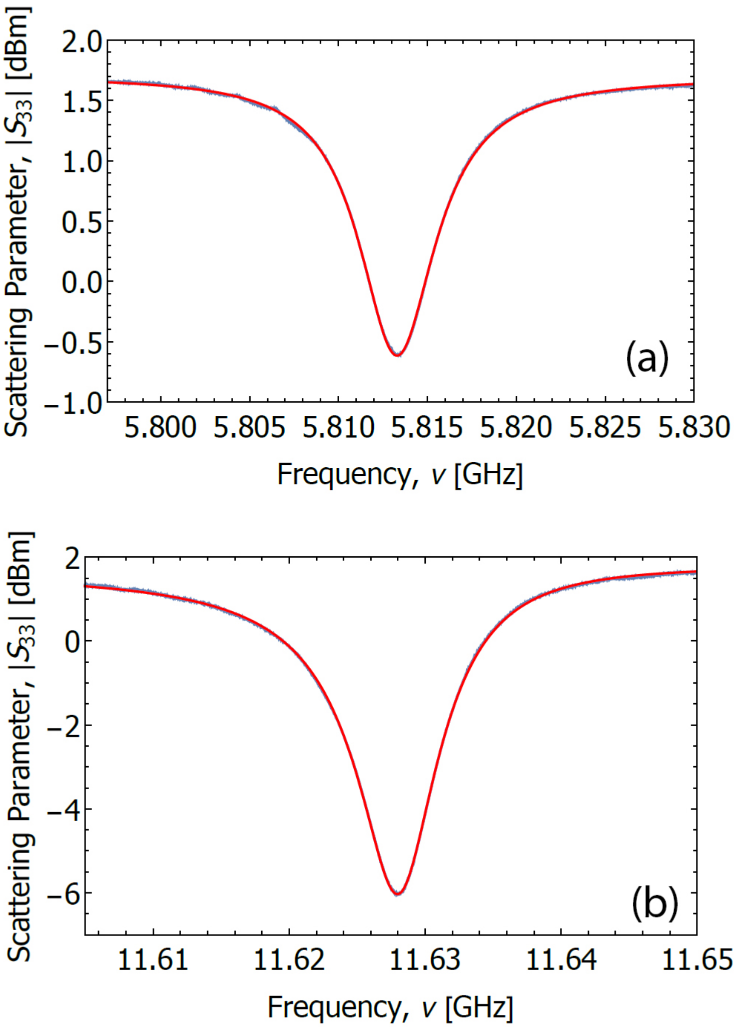

Figure 5.3: Panel (a) shows a fit of the fundamental resonance of the resonator of the B32 chip, while panel (b) shows the fit of the first higher order mode.

5.1.2 Cross Coupling

We now discuss the scattering parameters obtained from measuring the transmission between the different elements: through the transmission line itself, between the transmission line and the resonator, between the trans-

Chip	Designed f_0 (GHz)	f_0 (GHz)	Designed κ_0 (MHz)	κ_0 (MHz)	Q_{L_0} (MHz)
A11	5.751	5.794	9.5	6.00	965
A42	6.242	6.282	9.5	6.87	915
B14	5.530	5.655	55.2	25.5	222
B21	6.011	6.152	50.1	36.3	170
B32	5.751	5.812	9.5	6.04	962
B44	5.360	5.533	96.3	70.7	78.3
B51	5.833	6.017	86	85.5	70.4

Table 5.1: The determined fundamental frequencies f_0, loaded quality factors Q_{L0} and linewidths $\kappa_0 = \frac{Q_{L0}}{f_n}$ of the resonators of the measured A and B chips compared to their designed parameter values.

mission line and the flux line, and between the resonator and the flux line. Given that the geometry of each of the B chips is equal we only performed these measurements for the B32 chip, the general behaviour of which should cover that of all the chips.

Figure 5.4a shows all the scattering parameters of the transmission line itself for the B32 chip. We do not observe the presence of the 5.5 GHz mode, indicating that the transmission line is well decoupled from the resonator. There are however some higher frequency features in reflection (for example at 10.4 GHz), albeit not centered at the resonators; their origin is not known. Moreover, one can observe that the transmission spectrum is not flat; such trends will have to be adjusted for in transmission line measurements involving the qubits.

Additionaly, figure 5.4b shows the scattering parameters of the transmission between the resonator and the transmission line, where we chose to use port 1 for the transmission line as this port will be used as the input during the qubit experiments. Here we do observe that there is weak transmission at both 5.5 GHz and 11 GHz of -50 and -21 dB respectively, indicative of some coupling between the transmission line and the resonator. It is however small enough that it should not influence our experiments as it can always be calibrated out when relevant. Moreover, investigation of the A chips shows that this coupling is only present in the presence of the qubit box, meaning that it is the qubit box that mediates the coupling.

Finally we discuss the transmission between the transmission line and the flux line and the resonator and the flux line, again for the B32 chip. No intended connection or coupling between the transmission line and the flux line is fabricated, and as shown in figure 5.5(a) we also do not observe any,

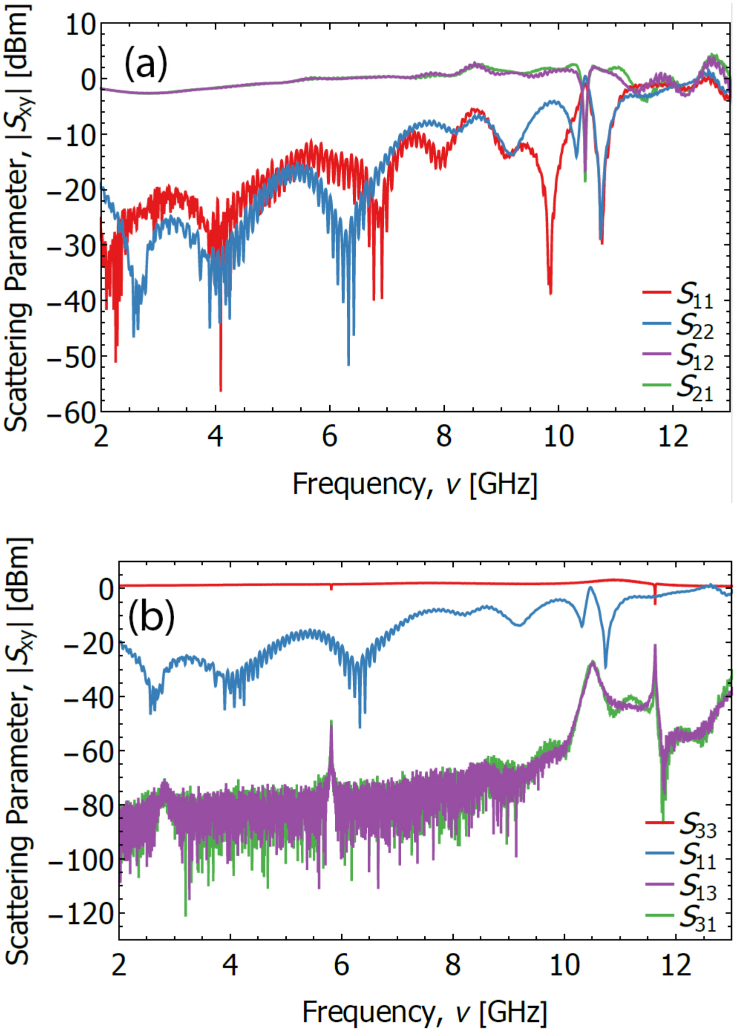

Figure 5.4: Panel (a) shows the scattering parameters of the transmission line (ports 1 and 2), while panel (b) shows the scattering parameters for the combined system of the resonator (port 3) and the transmission line (port 1).

indicating that the two elements are well decoupled. The same scenario exhibits different behaviour for the transmission between the resonator and the flux line; here we do observe a small transmission of -52 dB between the flux line and the resonator at 5.5 GHz as shown in figure 5.5(b), although no such transmission is present at 11 GHz in contrast to what was observed for the transmission line-resonator coupling. Importantly the coupling at 5.5 GHz is again small enough that it can be neglected in our experiments, especially when considering that neither of these elements will be strongly driven.

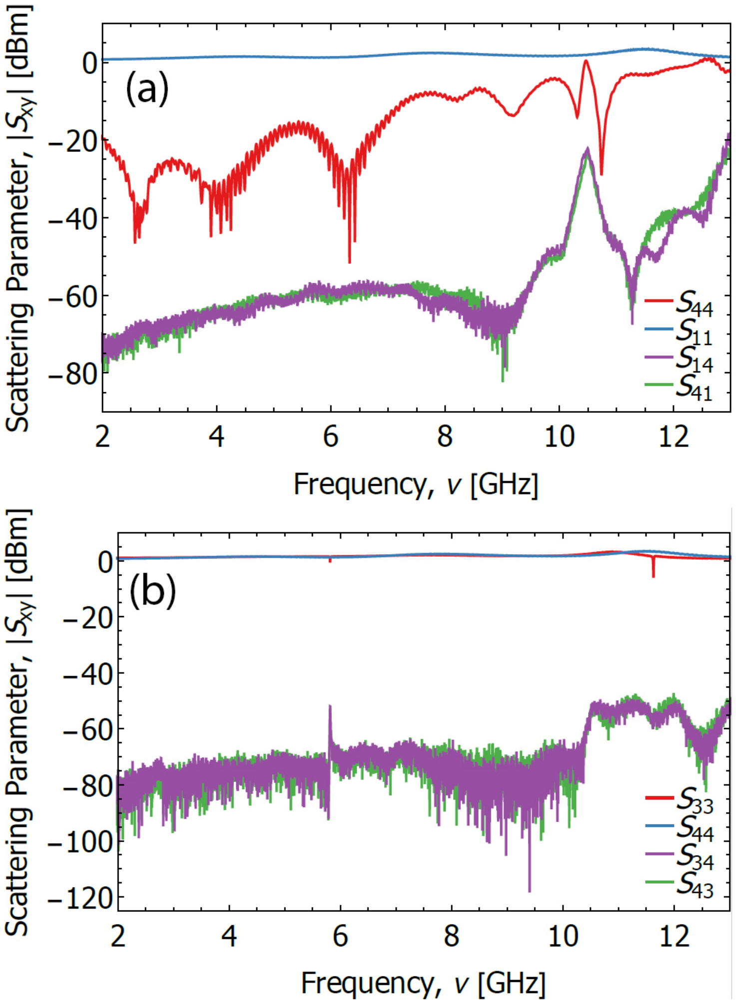

Figure 5.5: Panel (a) shows the scattering parameters of the transmission line (port 1) and the flux line (port 4) system for chip B32, while panel (b) shows the scattering parameters of the the resonator (port 2) and the flux line (port 4) system, also for chip B32.

5.1.3 Chip B5

Based on the characterization discussed in the previous section we decided that the B5 chips would be most suitable to use for our experiments involving the qubits. It has a center frequency around 1 GHz below the designed qubit frequencies as well as a loss rate of 85 MHz, allowing us to tune the decay rate of qubit 3 over a wide range of values via the Purcell effect discussed in chapter 2. In addition to this the B chips have been shown to exhibit negligible cross couplings between the different components and do not have any unexpected spectral features in the frequency ranges relevant for the qubits, establishing that they are suitable for our experiments.

5.2 Qubit System

At this stage the base chip has been chosen and the qubits have been designed and fabricated onto the sample, resulting in the chip shown in figure 5.6 which is repeated for convenience. In this section we treat the characterization of its properties using the cryogenic Bluefors1 setup, determining quantities such as the transition frequencies, driving rates, loss rates and charging energies for each element. This is done using a number of different tools introduced in chapter 2, such as magnetic flux dependence of the qubit frequencies, scattering parameters, and power spectral densities, using each of the lines connected to the sample.

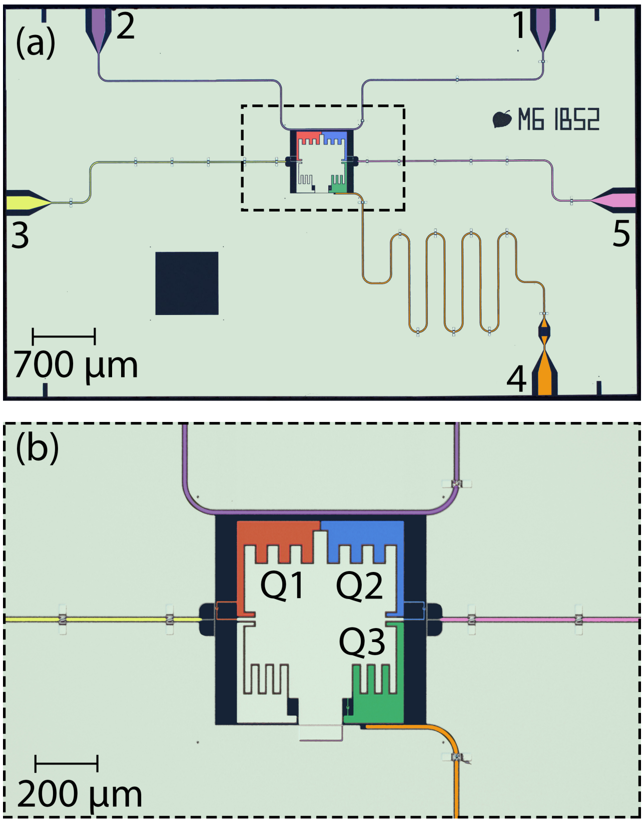

Figure 5.6: A false color microscope image of the sample used for the experiments in this thesis. Panel (a) shows the overall chip containing the transmission line, the two flux lines, the resonator and the qubits, while panel (b) offers a zoomed in picture of the qubit box.

5.2.1 Magnetic Flux Dependence

We begin by determining the parameters of the undriven three qubit resonator system, ignoring the presence of noise and the losses induced by the transmission line. As discussed in chapter 2, this system is governed by the Hamiltonian

$$\frac{\hat{\mathcal{H}}}{\hbar} = \omega_r \hat{a}^\dagger \hat{a} + \sum_{j=1}^{3} \left[\frac{\omega_j}{2} \hat{\sigma}_{z,j} + g_{jr} \left(\hat{a}^\dagger \hat{\sigma}_j^- + \hat{\sigma}_j^+ \hat{a} \right) + \sum_{k<j} J_{kj} \left(\hat{\sigma}_k^+ \hat{\sigma}_j^- + \hat{\sigma}_j^+ \hat{\sigma}_k^- \right) \right] \tag{5.3}$$

where we have included all potential parasitic couplings between the elements. We initially focus on the determination of ω_i, J_{ij} and g_{ir}; the transition frequencies and the coupling of the different elements. Determining these parameters can be done using the magnetic flux dependence of the qubit transition frequency. Assuming that the qubits are not completely identical, performing spectroscopy of their resonance frequency as a function of flux will lead to distinct signatures for each qubit in the systems transmission and reflection coefficients (equations 2.65 and 2.66).

To perform the spectroscopy we make use of three distinct sources of flux present in our system that can all be varied individually. These are the small superconducting coil, which is expected to act on all of the qubits in a rather uniform fashion, and the two flux bias lines which act primarily on the qubit they are nearest to. In practice each qubit will be affected by the flux of any of these elements due to finite cross-coupling, and one wishes to characterize these cross-couplings to gain individual control over the qubits. For this we model the flux seen by each by each qubit in the following way: each distinct flux generating element j is controlled by a voltage V_j, which is linearly related to the flux seen by the individual qubits through a generalized form of mutual inductance M_{ij} as previously discussed in the context of flux noise in chapter 3. Note that in addition to the user generated flux the model should also allow for a potential environmental offset Φ_{ei}, so that $\Phi_i = \sum_j M_{ij} V_j + \Phi_{ei}$. For our system of three qubits and three flux generating elements this can be written as

$$\begin{pmatrix} \Phi_1 \\ \Phi_2 \\ \Phi_3 \end{pmatrix} = \begin{pmatrix} M_{11} & M_{12} & M_{13} \\ M_{21} & M_{22} & M_{23} \\ M_{31} & M_{32} & M_{33} \end{pmatrix} \begin{pmatrix} V_1 \\ V_2 \\ V_3 \end{pmatrix} + \begin{pmatrix} \Phi_{e1} \\ \Phi_{e2} \\ \Phi_{e3} \end{pmatrix} \tag{5.4}$$

Combining this with the two level approximation for the Transmon from chapter 2 the transition frequency of the ith qubit is then given by

$$\omega_i \approx \sqrt{8 E_{Ci} E_{Ji} \left| \cos\left(\frac{\pi}{\Phi_0} m_{i*} \cdot \vec{V} + \Phi_i \right) \right|} - E_{Ci} \tag{5.5}$$

where m_{i*} denotes the ith row of the mutual inductance matrix $\underline{\text{M}}$ and $\vec{V}$ is the aforementioned voltage vector.

Given the above dependence on the flux, we vary each of the flux sources individually and perform spectroscopy of the qubit resonances as a function of the voltage applied. By fitting how the qubit frequencies respond to the magnetic flux we can determine the values of $\underline{\mathrm{M}}$, and in turn it gives us an estimate of the Hamiltonian parameters.

Figure 5.7 shows such a spectroscopic measurement through the transmission line, with a coherent microwave signal input into the transmission line at port 1 and output at port 2. By changing the voltage applied to the coil (and thereby the flux seen by each qubit) we can identify three distinct trajectories that each follow equation 5.5. We then subsequently fit these curves with the eigenvalues of equation 5.3 to determine the parameters; these fits are the green semitransparent lines. Note that the spectrum of qubit 3 is difficult to determine in this measurement. It is only visible when it is close to resonance with qubits 1 and 2 as only they couple to the transmission line. In order to follow qubit 3 all the way up to its maximal frequency (the sweet spot) we measure its spectrum through the resonator in reflection instead (port 4 functions as both input and output), in which case qubits 1 and 2 are difficult to measure.

While such a general flux sweep is a good starting point to obtain estimates for all of the parameters, more accurate determination requires a tailored approach. For example, M_{11} and Φ_{e1} are uniquely determined by measuring the first and the second sweet spot of qubit 1 due to the periodicity of the Josephson energy, and in a similar way one can accurately determine the entire matrix $\underline{\mathrm{M}}$ element by element. The determined matrix is given in table 5.2. It is in line with expectations, apart from the fact that the first flux bias line (port 3, closest to qubit 1) has significant cross coupling to qubit 3, whereas the second flux line (port 5, closest to qubit 2) has much weaker cross coupling. Quantitatively, $\frac{M_{32}}{M_{12}} = -0.20$ whereas $\frac{M_{33}}{M_{23}} = -0.06$; flux line 1 couples to qubit 3 more than three times as strongly as flux line 2 to qubit 3. The cause of this asymmetry is not understood as of yet, and while when it comes to biasing the qubits it can be compensated for with the other flux sources, the same does not hold for applying noise. As derived in chapter 2, the noise applied to flux source j seen by qubit i is proportional to M_{ij}^2; applying noise to flux line 1 will thus also affect qubit 3 to a non-negligible degree. Future designs of the base chip (the B chips of mask 61) should aim to investigate the cause of the cross coupling and improve on this.

Having determined $\underline{\mathrm{M}}$ offers a new tool: it allows for individual control of the qubits. Numerically inverting equation 5.5, we can numerically map out qubit trajectories in flux space to create virtually any scenario. An example of such a numerically generated trajectory is shown in figure 5.8, where we performed spectroscopy through the transmission line for settings of $\vec{V}$ (and thus of $\vec{\Phi}$) for which the bare frequencies of qubits 1 and 2 would

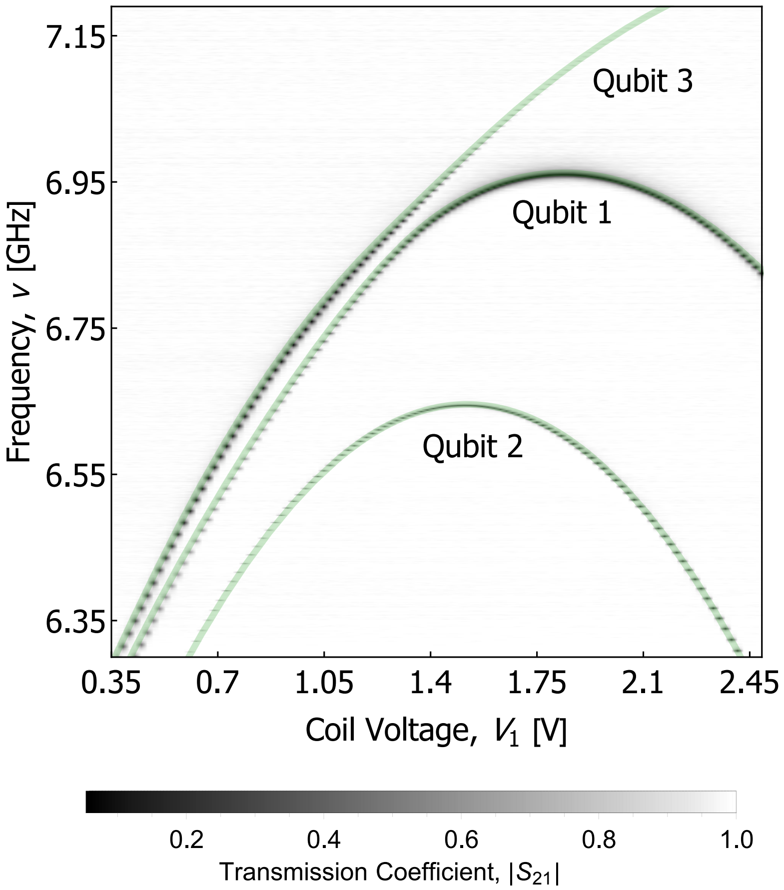

Figure 5.7: Magnetic flux dependence of the three qubits measured through the transmission line. The applied coil voltage V_1 is linearly proportional to the magnetic flux received by each qubit. The green lines indicate a fit with the eigenvalues of the Hamiltonian of the system.

$M_{ij}/\Phi_0[V^{-1}]$	$i1$	$i2$	$i3$
$1j$	0.135	0.159	0.023
$2j$	0.158	-0.058	-0.191
$3j$	0.093	-0.032	0.012

Table 5.2: Mutual inductance parameters in terms of number of flux quanta for all three voltage sources (columns) and qubits (rows).

intersect each other while keeping qubit 3 far detuned. These trajectories are indicated by white dashed lines. Due to the presence of finite qubit-qubit coupling J_{12} the trajectories anticross; they hybridize into the bright and the dark mode derived in chapter 2, with the bright mode being much more pronounced than the dark mode that almost completely vanishes from the measurement. Not only does this allow us to study the hybridization in more detail as discussed at the end of this chapter, it also allow us to determine J_{12} with the highest possible accuracy. We find it to be 94 MHz when qubits 1 and 2 are at their maximal frequencies. By performing similar measurements we then determine all of the coupling parameters.

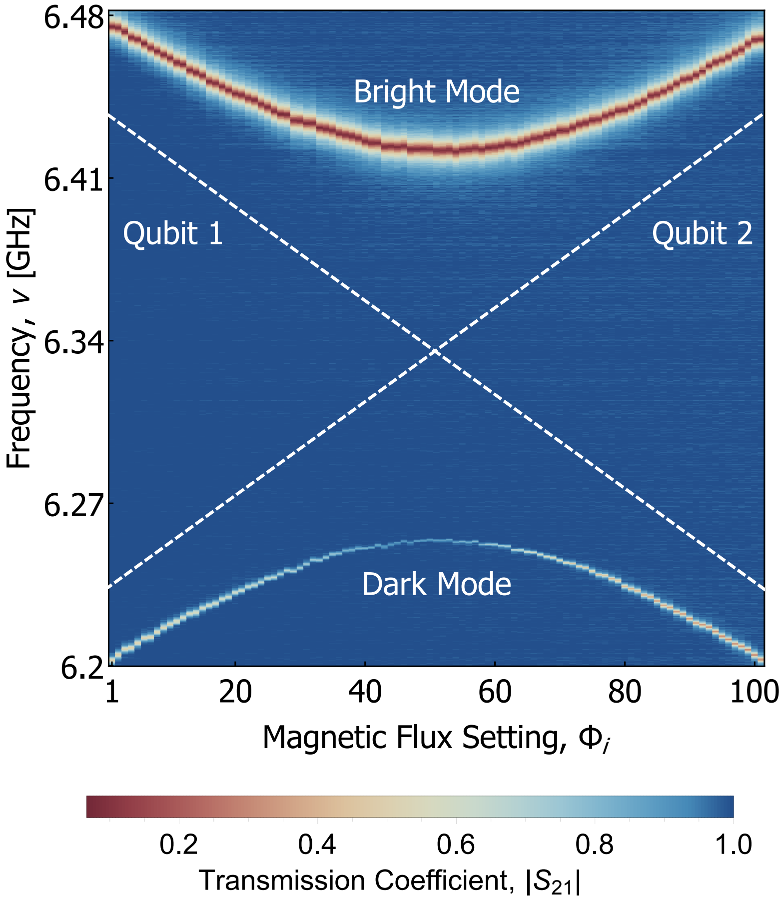

Figure 5.8: Anticrossing between qubits 1 and 2 which hybridize into the bright dark modes, measured through the transmission line. The dashed lines indicate the uncoupled frequencies of the qubits.

Special attention should be given to the determination of the resonator frequency ω_r. It cannot be measured directly using the magnetic flux dependence as its resonance frequency is independent of flux, and as previously measured at 4 K it has a substantial loss rate κ_r which means that measuring its absolute lineshape in reflection does not lead to any discernable signature in our setup. Instead we measure its resonance frequency in phase using a phase reference; as discussed in chapter 4 we split the signal input into the resonator into two, the first branch of which enters the cryostat and then the resonator, while the other does not. We then compare the phase of the signal output by the resonator to the second branch and from this we restore the phase information of the spectroscopy measurement, which is much less sensitive to having a large κ_r and allows us to determine ω_r.

Table 5.3 lists all of the determined parameters of the Hamiltonian (equation 5.3) at their maximal value, along with their designed or simulated values which were discussed in chapter 3. The resonator frequency is the exception here: we instead list the value determined during the dipstick measurements discussed in the previous section. The listed values are all determined with an accuracy of around 1 MHz, with the exception of g_{2r} which has an accuracy of 100 kHz and g_{1r} of which no signature was found with a resolution of 200 kHz. Most parameters are in line with the designed parameters, with especially J_{12} and g_{3r} lower than simulated. In addition to this ω_r has decreased compared to what was measured at 4 K. This can be attributed to an increased effective effective permitivity ε_{eff} of the CPW due to the lower temperature.

Parameter	Measured value/2π	Designed value/2π
ω_1	6.948 GHz	6.8 GHz
ω_2	6.694 GHz	6.8 GHz
ω_3	7.271 GHz	6.8 GHz
ω_r	5.985 GHz	6.017 GHz
J_{12}	94 MHz	120 MHz
J_{13}	6 MHz	3.7 MHz
J_{23}	37 MHz	38 MHz
g_{1r}	$\leq$ 200 kHz	200 kHz
g_{2r}	1 MHz	1.4 MHz
g_{3r}	77 MHz	110 MHz

Table 5.3: Measured and designed Hamiltonian parameters for all three qubits and the resonator.

The qubit frequencies ω_i require further analysis in order to fully characterize them: they are determined by the charging energy E_C and the maximal Josephson energy E_J. These can be determined by using that the transmon is not a pure two-level system; as discussed in chapter 2 there are other energy states than the g and e states used to define the two level system and the first of these is the f level. For this level one can show that $\omega_{fe} \approx \omega_{eg} - E_C$ [39] and this level can be made visible in spectroscopy by using relatively strong driving rates: the ground state transmon can undergo a so called $(g \rightarrow f)/2$

transition in which two photons of energy $\omega_{fg}/2 = \omega_{eg} - E_C/2$ excite the g state into the f state. Comparing this transition frequency to the standard $g \to e$ transition then allows one to determine E_C and through equation 5.5 E_J is then known as well. One can also determine the relative anharmonicity α_r by comparing the two transition frequencies, repeated here for convenience.

Table 5.4 lists all of these parameters for the three qubits at their maximal frequencies, in which we observe that the charging energies are very close together albeit somewhat offset from their simulated value, and that there is a spread of around 10% between the Josephson energies which is in line with expectations [63].

Qubit	Measured E_C	Designed E_C	Measured E_J	Designed E_J	α_r
1	140 MHz	121 MHz	44.9 GHz	50 GHz	-0.020
2	142 MHz	120 MHz	41.1 GHz	50 GHz	-0.021
3	137 MHz	121 MHz	50.1 GHz	50 GHz	-0.019

Table 5.4: Transmon parameters for all three qubits.

5.2.2 Driving Rate

Having determined the qubit and resonator parameters as well as their couplings, we now turn to the relation between the microwave signal input into the transmission line at port 1 and the driving rate experienced by qubits 1 and 2, $\Omega_{1,2}$. In chapter 2 we discussed two measurement scenarios in which the driving rate showed up: in the lineshape of a driven qubit (equation 2.69), and in its resonance fluorescence, in the form of the Mollow triplet (equation 2.72. These equations were derived in the context of a single qubit coupled to the transmission line, which is rather different than our coupled system. However, using the flux sources available in the system we can tune our qubits into a regime where this is effectively the case: detuning the qubits from each other by several GHz essentially decouples them, allowing us to use the formalism developed for single qubits, similar to how we studied the bright and dark mode in the absence of qubit 3 in figure 5.8.

The above scenario thus allows us to study the lineshape and the resonance fluorescence of the individual qubits. However, in the lineshape Ω and $\gamma_r = \Gamma - \gamma_{nr}$ act in a rather similar way, essentially broadening the lineshape and influencing its amplitude. The simultaneous determination of these parameters is therefore troublesome. Moreover, at higher input powers the qubit saturates, reducing the contrast of the lineshape significantly. The resonance fluorescence does not suffer from these effects; the positions of the side peaks of the Mollow triplet are determined predominantly by Ω. It thus serves as a strong tool for characterizing the driving rate. Conversely, it is not very suitable for determining parameters such as γ_r, γ_{nr} and γ_ϕ as these rely on the height of the center peak of the triplet, the measured amplitude of which depends sensitively on the gain profile of our output; we will thus characterize these parameters in a different way.

Returning to the driving rate, we begin by isolating qubits 1 and 2 at the frequencies of interest using $\underline{\mathrm{M}}$. In our main experiments (discussed in chapter 6) qubits 1 and 2 are hybridized into the bright and dark mode, with their bare frequencies around 6.35 GHz. We therefore characterize their driving rate at this frequency. This is done by first measuring the qubit lineshape in spectroscopy (through the transmission line) and then measuring its power spectral density, by driving the qubit on resonance and measuring its power spectral density, also through the transmission line. We then measures the resulting resonance fluorescence as a function of power and simultaniously fit them with an analytic expression of the Mollow triplet (see [28]).

The resulting fits are shown in figure 5.9a, where the position of the side peaks is governed by Ω. Note that in these figures we used some knowledge about parameters yet to be characterized: the amplitude of the triplets is reduced from its maximal value of 0.5, set by the fact that we look at a single output of the transmission line, due to finite γ_ϕ and γ_{nr}. While needed for the correct vertical scaling of the spectrum, they do not influence the position of the side peaks.

The determined values of Ω can then subsequently be fit to the input microwave power set on the signal generator $\Omega_j \propto \sqrt{P}$. As shown in figure 5.9b such proportionality is well reproduced, allowing us to tune Ω_1. Similar measurements were performed for qubit 2, and we find that the relevant constants of proportionality are given by $a_1 = 36.9\ \mathrm{GHz}/\sqrt{\mathrm{Watt}}$ and $a_2 = 32.0\ \mathrm{GHz}/\sqrt{\mathrm{Watt}}$. Note that these constants of proportionality are a function of the attenuation in the input line and the loss rates of the qubits, where the former is identical for both. The discrepancy between the two values is thus due to a difference in their loss rates, which we determine in the next section.

5.2.3 Loss Rate

The next parameter we wish to determine is the loss rate $\Gamma = \gamma_r + \gamma_{nr}$. Having characterized Ω we are free to use the lineshape to determine γ_r, but determining γ_{nr} in this way is again problematic: it is almost indistuingishable from γ_ϕ. In order to circumvent this problem we follow the method of [52] and use that γ_ϕ is expected to be dominated by its flux noise contribution, for which we derived in chapter 2 that $\gamma_\phi \propto \left(\frac{\partial \omega_{eg}}{\partial \Phi}\right)^2$. If we thus measure

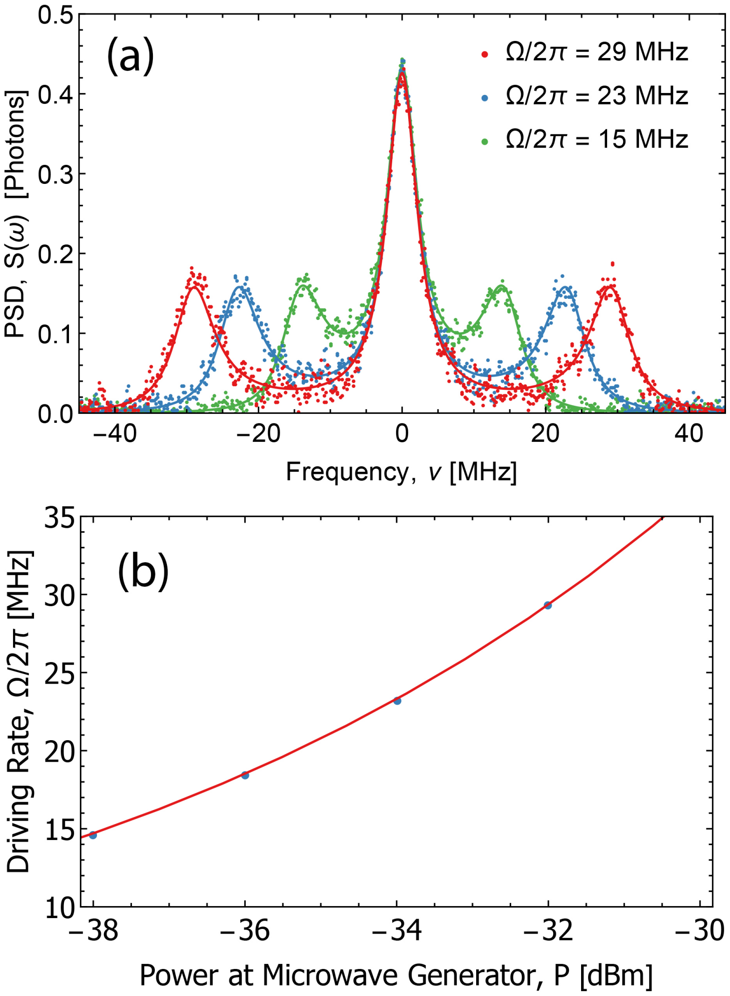

Figure 5.9: Resonance fluorescence measured through the transmission line in the scenario where qubit 1 is at 6.35 GHz and the other two qubits are far detuned. The solid curves denote fits with an analytic expression for the Mollow triplet.

the qubit lineshape at its sweet spot we can approximate that $\gamma_\phi = 0$ and determine γ_{nr}. Subsequent determination of γ_ϕ at some other frequency can then be done by fixing γ_{nr} to that determined value; this is covered in the next section.

When determining γ_{nr} at the maximal qubit frequency it is important to consider that γ_r (and by extension Ω) are frequency dependent. While from basic theoretical considerations one can find that $\gamma_r \propto \omega_{eg}^2$, the fact that the transmission line does not have a flat density of states means that one cannot assume this relationship to hold [52]. In order to properly determine γ_{nr} one thus has to recalibrate Ω at the maximal qubit transition frequency.

Having done so, figure 5.10 shows a measurement of the lineshape of qubit 2 at its sweet spot for various powers along with their fits. We observe that the lineshapes saturate for higher driving powers as is expected; a two level system can absorb only one photon at a time. Moreover we find that $\gamma_r = 5.48$ MHz and that $\gamma_{nr} = 210$ kHz. Table 5.5 lists these parameters for all three of the qubits determined in the same way, where the measurements for qubit 3 were done in reflection via the resonator. We find that qubits 1 and 2 have similar radiative loss rates, indicative of the fact that they couple to the transmission line with similar strengths.

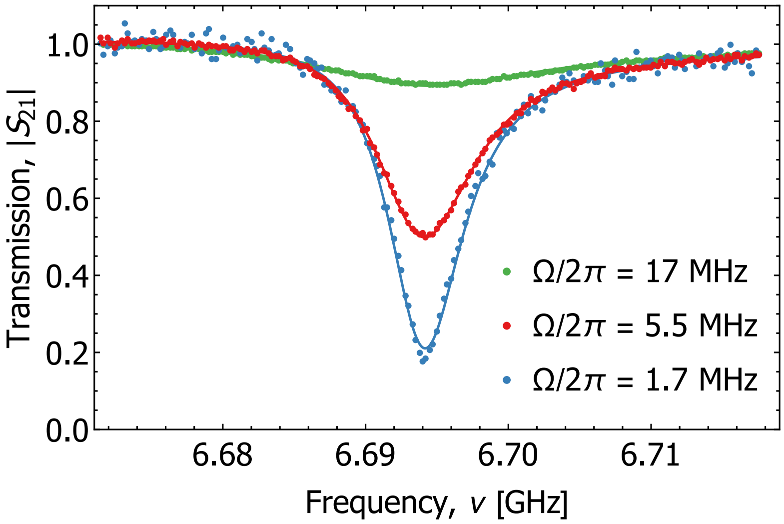

Figure 5.10: Lineshapes for qubit 2 at its sweet spot as a function of driving rate.

Qubit	$\gamma_r/2\pi$	$\gamma_{nr}/2\pi$
1	5.83 MHz	390 kHz
2	5.48 MHz	210 kHz
3	325 kHz	120 kHz

Table 5.5: The radiative and nonradiative loss rates for all three qubits as measured at their maximal frequencies.

However, in table 5.5 we see that qubit 3 has a much lower loss rate than the other two qubits. This is as expected; as discussed in chapter 2 the mechanism governing its radiative losses is not the coupling to the transmission line but the coupling to the resonator, via the Purcell effect. We discussed that when the two elements are on resonance the loss rate of qubit 3 is equal to half the loss rate of the resonator κ, while at large detunings it decreases like $\frac{1}{\Delta^2}$, explaining the low value measured at the sweet spot of qubit 3. Given the above, we measured γ_{r3} as a function of detuning in order to get an estimate of κ at cryogenic temperatures, the results of which are shown in figure 5.11. By fitting the loss rates with the analytic expression for the Purcell effect (equation 2.39) and keeping ω_r and g_{3r} fixed, we found that $\kappa = 51.2$ MHz, down from 85.5 MHz at 4 K. A significant decrease, we again attribute it to the higher effective permitivity of the CPW at cryogenic temperatures compared to 4 K. Note that ideally one would have more data in the region close to the resonator frequency, the qubit lineshapes become so distorted that the determination becomes troublesome.

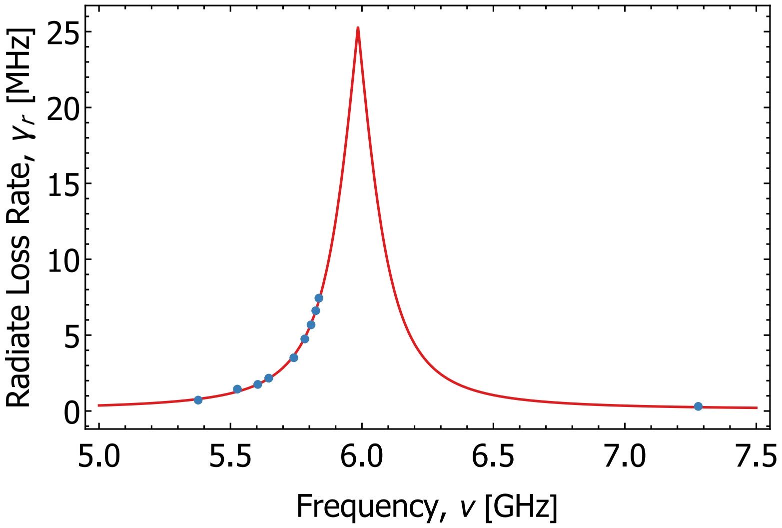

Figure 5.11: The loss rate of qubit 3 as a function of detuning from the resonator, fit with the analytic expression for the Purcell effect.

5.2.4 Pure Dephasing

The last system parameter to be characterized is the pure dephasing rate γ_ϕ. Having fixed all other parameters, it can be found from the single qubit lineshapes used extensively in the previous section. However, we derived that $\gamma_\phi \propto \left(\frac{\partial \omega_{eg}}{\partial \Phi}\right)^2$; its determination is therefore frequency dependent. While the dephasing rate as a function of qubit frequency thus requires measurements at many different bias points, the experiments discussed in the next chapter are done with the qubits confined to a region of about 100 MHz around 6.35 GHz where the variation in γ_ϕ is small. We therefore determine it at 6.35 GHz and assume it to be independent of frequency for the scenario's of interest. However, it is not independent of every factor; as discussed in chapter 3 we intend to control the flux noise environment for the qubits, governed by noise with a specific distribution and power spectral density. Varying the properties of this noise changes γ_ϕ significantly, as we now characterize.

More specifically, we measure the lineshapes of the qubits while applying the white noise designed in chapter 3. Shown and discussed in figure 3.8, it is white up to 300 MHz after which it exponentially decays to 0 at 350 MHz while it has a base amplitude of $S_X = 0.1$ V^2/Hz. In order to vary the noise power this amplitude is varied in small steps with AWG, while larger steps are made by attenuating it with either 3 dB or 8 dB. Moreover, the noise is only applied to flux line 2 and therefore predominantly to qubit 2, the choice for which is motivated by the relatively strong cross coupling between flux line 1 and qubit 3, the consequences of which we expand upon in the next chapter. Note that in order to fit the lineshapes we also had to determine the radiative loss rates of qubits 1 and 2 at 6.34 GHz using the methods introduced in the previous section where we found that $\gamma_{r1} = 3.34$ MHz and $\gamma_{r2} = 3.30$ MHz respectively.

Figure 5.12a shows the measured lineshape of qubit 2 as a function of noise power applied to flux line 2, fit by keeping all parameters other than γ_ϕ fixed to their determined values. The lineshape becomes broader and more shallow as a function of dephasing rate, which can be understood through the fact that the noise essentially causes the qubit frequency to rapidly oscillate. This causes an effective spread in its center frequency, broadening the mode, and making it so so that a fixed microwave drive is never fully on resonance, making it more shallow.

Panel b shows the extracted relationship between the dephasing rate and the applied noise power in terms of its amplitude before it enters the cryostat. As derived in appendix A we find a linear relationship between the noise amplitude and the dephasing rate of the form $\gamma_\phi = a + bS_X$; more specifically we find that $a_2 = 450$ kHz is the dephasing rate of qubit 2 with no noise applied, while $b_2 = 1900$ kHz^2/V^2. In a similar way we characterize the effect of the noise applied to flux line 2 on qubits 1 and 3, as given in table 5.6. It can be seen that the coupling to these qubits is indeed much weaker as was expected; at the highest applied noise power qubit 3 has a dephasing rate of only 1.1 MHz which should not influence the experiments by a significant amount. However, if one were to apply an equal amount of noise to flux line 1 the resulting dephasing would be six times higher as seen from table 5.2. Observing the effect of $\gamma_\phi = 3$ MHz on the lineshape of qubit 2 in 5.12a illustrates that $\gamma_\phi = 6$ MHz would affect qubit 3 significantly, which is why we choose to apply the noise only to flux line 2.

5.2.5 Bright and Dark Basis

In addition to the fact that applying noise on flux line 1 would dephase qubit 3, we now argue that there is also no physical reason for why we

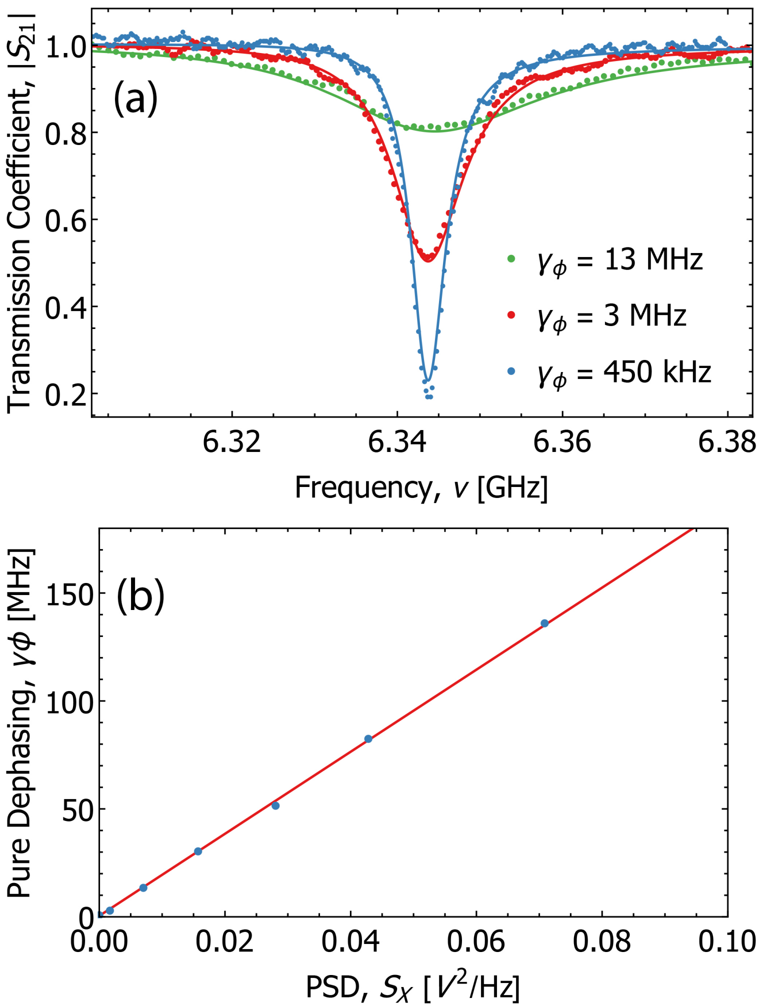

Figure 5.12: Panel (a): Lineshapes for qubit 2 isolated at 6.34 GHz as a function of applied noise power. Panel (b): Extracted linear dependence of the pure dephasing γ_ϕ of qubit 2 on the applied noise power.

should apply noise to both flux lines. It is evident that in the scenario where one considers the performance of qubits 1 and 2 separately, applying noise to only a single flux line causes a significant asymmetry in the system, essentially leaving qubit 1 unaffected. However, in the experiments discussed in the next section we do not consider such scenarios: we only look at the reduced system of qubit 2 and qubit 3, or at the three qubit system in which qubits 1 and 2 are fully hybridized into the bright and dark mode. Treated in chapter 2, we described how in this basis the bright and dark mode experience a pure dephasing rate equal to the mean of the individual qubit dephasing rates. Disregarding the small cross coupling between flux line 2

Qubit	a	b
1	380 kHz	6.28 kHz^2/V^2
2	450 kHz	1900 kHz^2/V^2
3	710 kHz	5.28 kHz^2/V^2

Table 5.6: The scaling parameters $\gamma_\phi = a + bS_X$ *of the qubits at 6.34 GHz as determined for 300 MHz bandwidth white noise with* $S_X = 0.1\text{V}^2/\text{Hz}$ *applied to flux line 2.*

and qubit 1, the pure dephasing rate of the bright and dark mode is thus given by $\gamma_{\phi\{B,D\}} = \frac{\gamma_\phi}{2}$. Working in this basis there is thus no distinction between applying noise to both qubits or to the individual qubits.

Motivated by the fact that we work in the bright and dark mode basis in the next chapter, we also performed all the above characterization steps for the bright and the dark mode. This was achieved by tuning qubits 1 and 2 on resonance at 6.34 GHz, resulting in the spectrum shown in figure 5.13. In line with expectations, one observes the narrow and shallow dark mode (indicative of its extremely weak coupling to the transmission line) and the much broader and deeper bright mode. Assuming that the bright and dark mode had a nonradiative loss rate $\gamma_{nr\{B,D\}} = \frac{\gamma_{nr1}+\gamma_{nr2}}{2}$ as predicted by the theory discussed in chapter 2 we found that $\gamma_{rB} = 6.09$ MHz, which in line with the $\gamma_{r1} + \gamma_{r2} = 6.6$ MHz expected from theory. For the dark mode we find $\gamma_{rD} = 120$ kHz; its loss rate is thus dominated by γ_{nr}. Note that the reason for the nonzero radiative losses might be that the two qubits do not have identical properties, or that the hybridization is not perfect. Regardless of this we find that $\frac{\Gamma_D}{\Gamma_B} = 0.08$; the loss rate of the dark mode is thus less than 10% of that of the bright mode.

Finally we also characterized the effect of noise applied to flux line 2: for the bright mode we found a base dephasing rate of $a_B = 590$ kHz and a noise scaling parameter of $b_B = 924\ \text{kHz}^2/\text{V}^2$. This is slightly lower than one half of b_2, which might again be explained by the unequal properties of qubits 1 and 2. Such characterization was not possible for the bright mode; due to its marginal γ_r any applied noise makes its lineshape almost impossible to measure. We will thus assume that $\gamma_{\phi B} = \gamma_{\phi D}$, as predicted by theory.

With the above we have determined the last parameters of the sample, fully characterizing all of its relevant properties. What remains now is using the knowledge of these parameters and the degrees of freedom available to us in order to create the scenario's relevant to the biological scenario's discussed in the introduction, which is the subject of the next chapter.

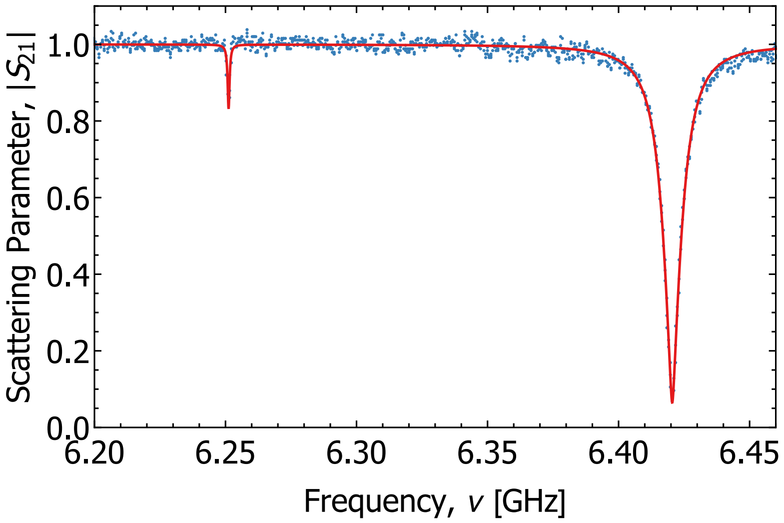

Figure 5.13: Scattering parameter $|S_{21}|$ of the bright and dark mode as measured through the transmission line.

Chapter 6

Results & Discussion

Having fully characterized the system, we are now able to perform several experiments related to noise assisted transport. We do this in two distinct scenarios: in the first we consider only qubits 2 and 3, resulting in the two site model discussed in chapter 1, while in the second scenario we introduce qubit 1 into the picture and fully hybridize qubits 1 and 2 into the bright and dark mode. In both of these scenario's we then expose qubit 2 to noise of a certain power spectral density and explore how the energy transported from the transmission line to the resonator evolves.

Experimentally we set up the scenario's as follows: we first pick a suitable flux bias point in order to obtain a certain hierarchy of energy levels in the system, of which we then coherently excite the highest energy mode via the transmission line. Simultaneously we apply a noise signal with a specific amplitude to flux line 2 and measure the system's incoherent emission spectrum in the form of a power spectral density through the resonator output. This power spectral density is integrated to obtain a power, which is our figure of merit for how well radiation is transported. The above is then repeated for different noise amplitudes and power spectral densities as designed in chapter 3.

6.1 White Noise Environment

We begin our experiments in the setting of a white noise environment, a scenario well studied in literature and also experimentally explored in the classical setups discussed in chapter 1. While research has shown that the environment of FMO consists of highly structured noise, such investigations are still important in order to establish the general effect of noise on the transport, while potentially giving insight into an underlying mechanism.

6.1.1 Two Qubit Scenario

We start with the discussion of the two qubit scenario, depicted in figure 6.1(a). In this scenario qubit 2 is coherently excited via the transmission line, acting as the pigment site closest to the antenna where the excitation enters the system. At the frequency used in this setup it has a loss rate of $\Gamma_2/2\pi = 3.5$ MHz and it couples to qubit 3 with $J_{23}/2\pi = 33$ MHz, where qubit 3 acts as the site closest to the reaction center. Its excitations are then transfered into the reaction center via the Purcell effect mediated by their coupling $g_{3r}/2\pi = 71$ MHz. In addition to this white noise is applied to flux line 2, playing the role of a memoryless environment.

Aside from the system parameters fixed by design, the dynamics of the scenario are governed by a number of variables. First one has the drive strength Ω_2, the rate at which qubit 2 is excited, which sets the excitations incoming from the antenna complex per unit time. One also has the detuning between qubits 2 and 3 Δ_{23}, essentially governing how effective their coupling is. The detuning between qubit 3 and the resonator Δ_{3r} then sets the loss rate of qubit 3, governing how many excitations can be transferred to the reaction center per unit time. Finally, one has the noise PSD amplitude $S_\Phi(f)$, governing the effective coupling between the environment and qubit 2. In order to simplify the situation we fix two of these parameters: $\Omega_2/2\pi = 10$ MHz and $\Delta_{3r} = 250$ MHz, resulting in $\Gamma_3/2\pi = 3.4$ MHz. We then study the power spectral density and the power output at the resonator as a function of noise PSD amplitude S_Φ for several different detunings Δ_{23}.

Figure 6.1(b) shows the measured PSD for $\Delta_{23} = 0$ as a function of dephasing rate of qubit 2. Note that at this detuning qubits 2 and 3 fully hybridize into two new modes that couple equally to the resonator and the transmission line and are energetically separated by $2J_{23}$; we refer to them as H1 and H2. We observe that at no noise power applied all of the resonance fluorescence is located at the frequency of H2, which is where the coherent excitation is applied. This can be understood through the quantum localization effect introduced in chapter 1; the energy level mismatch between the two sites leads to a negligible overlap with H1. However, with increased noise power we observe that some of the excitations are transferred to H1; the noise effectively opens a channel between the two states. At even higher noise powers we observe that the fluorescence at both modes keeps decreasing, which can be understood through the quantum Zeno effect (QZE).

Figure 6.1(c) shows the same measurements for the scenario in which the two qubits are detuned: $\Delta_{23} = 50$ MHz. At this detuning the qubits are less hybridized and behave more like the individual qubits, which is also reflected in the measurements. At no applied noise power all of the fluorescence is again localized at the frequency of qubit 2, but the overall amplitude is smaller than in the zero detuning case. This is because at this detuning

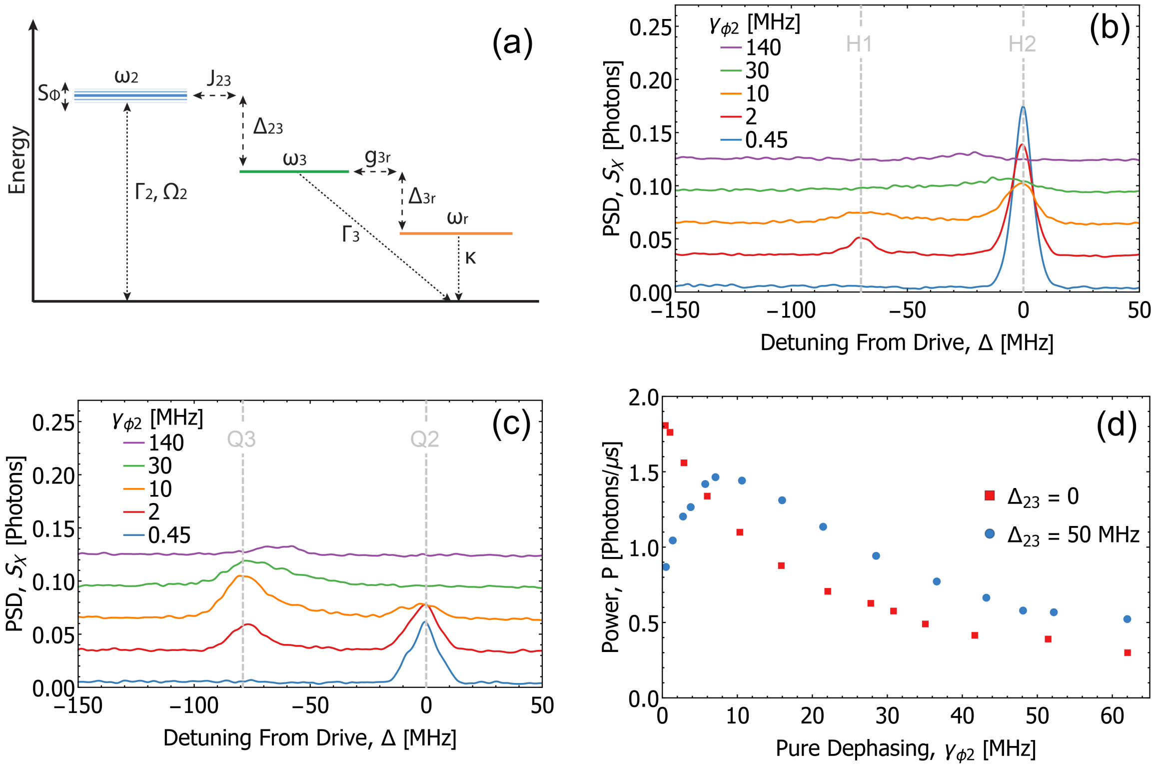

Figure 6.1: (a) Energy level diagram of the two qubit scenario, indicating the relevant parameters and variables. Qubit 2 is driven via the transmission line (port 1) and the output of the system is measured through the resonator (port 4). (b) Power spectral density measurements of in the $\Delta_{23} = 0$ *as a function dephasing rate. The gray lines indicate the positions of hybridized modes H1 and H2. (c) Power spectral density measurements of in the* $\Delta_{23} = 50$ *MHz case as a function dephasing rate. The gray lines indicate the positions of qubits Q2 and Q3. (d) Integrated power spectral densities of both* Δ_{23} *cases as a function of noise power applied.*

the effective coupling between qubits 2 and 3 is weaker, and by extension so is the coupling from qubit 2 to the resonator. This behaviour again changes at higher noise powers: we observe more fluorescence at qubit 3 with increasing S_Φ, indicative of the noise opening a channel facilitating transport between the two modes. At even higher noise powers we then once more observe that all of the amplitudes again go down due to the QZE.

In order to quantify the above trends we subsequently integrated the measured power spectral densities for each applied noise power, as depicted in figure 6.1d. Here we observe an interesting difference between the two cases: for $\Delta_{23} = 0$ the output power starts from a maximum and smoothly decreases as a function of noise power, despite excitations being transported from H2 to H1 in the phase between the initial localization and the QZE. This is because such transport leads to no benefits: H2 and H1 couple to the resonator equally. For the $\Delta_{23} = 50$ MHz case the observed trend is different: the transported power starts off lower than the other scenario due to the localization at qubit 2, but for moderate noise powers the output power increases and even overtakes the first scenario. We thus observe noise assisted transport. At higher noise powers the output power again decreases, in line with the expected QZE effect.

6.1.2 Three Qubit Scenario

The above has been our first experimental verification of noise assisted transport as seen in the simple two site system. We now move on to the three qubit scenario, depicted in figure 6.2(a). In this scenario qubits 1 and 2 are fully hybridized into the bright and dark modes, whose transition frequencies are split by $2J_{12}/2\pi = 175$ MHz. As discussed before the bright mode functions as a superradiant absorber and is thus essentially the site closest to the antenna, while the dark mode is close to uncoupled from the transmission line. It functions as an intermediate site between the initial and the final site to which it couples with $J_{D3}/2\pi = 19$ MHz, the role of which is again played by qubit 3. In addition to the above noise of amplitude S_Φ is again applied to flux line 2, playing the role of the fluctuating environment for both the bright and the dark mode which couple to it with half the strength of the individual qubits.

The dynamics of this scenario are governed by similar parameters as the previous one: the bright mode is excited with Ω_B, the detuning between the dark mode and qubit 3 is given by Δ_{D3}, the detuning between the resonator and qubit 3 is given by Δ_{3r} and the noise amplitude is given by S_Φ, where its effect on the bright and dark mode is approximately half of its effect on qubit 2 alone. We again fix two of these parameters: $\Omega_B/2\pi = 15$ MHz (chosen by using the same input power as in the two qubit experiment) and $\Delta_{3r} = 200$ MHz, resulting in a slightly increased $\Gamma_3/2\pi = 4.6$ MHz. We then again study the power spectral density and the power output at the resonator as a function of noise PSD amplitude S_Φ for several different detunings Δ_{23}. However, it is important to note that we do not study this scenario for explicit comparison to the two qubit case: we study it due to its cascading energy level structure, a reduced version of what is experimentally observed for FMO.

Similar to the two qubit scenario, figure 6.2(b) shows measurements of the PSD as a function of dephasing rate for $\Delta_{D3} = 0$. At this detuning the dark mode and qubit 3 fully hybridize into two new modes that couple equally to the resonator, and they are energetically separated by $2J_{D3}$. We

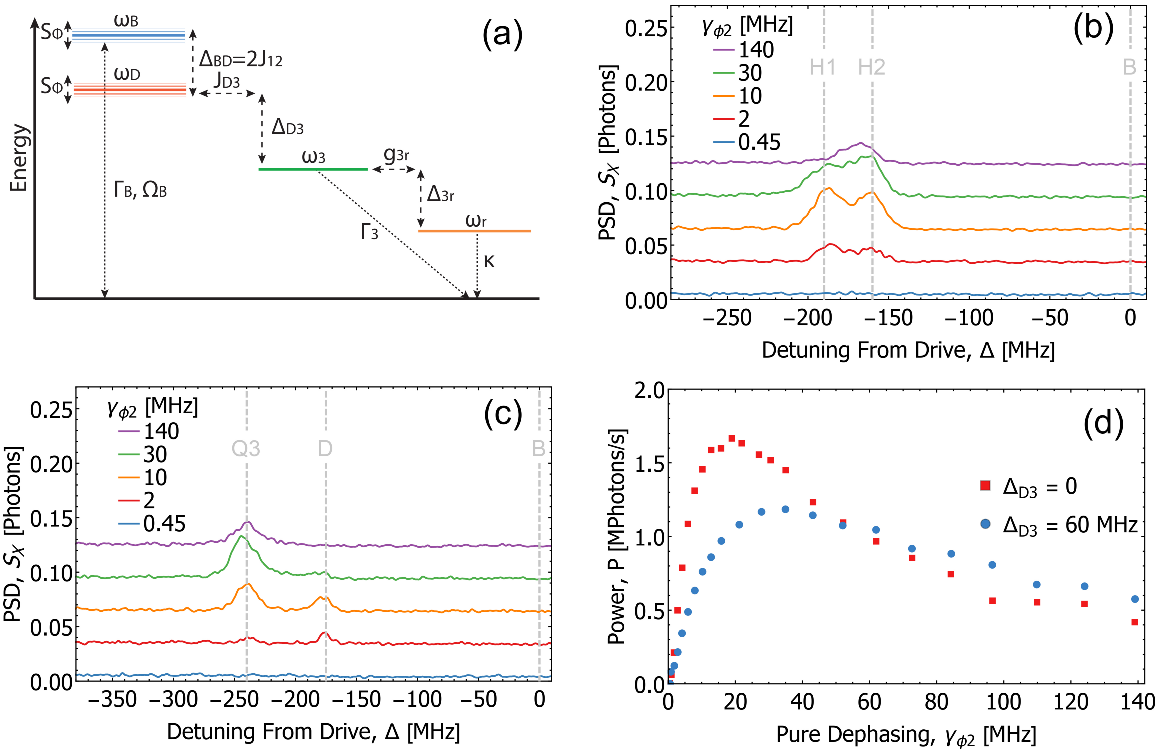

Figure 6.2: (a) Energy level diagram of the three qubit scenario, indicating the relevant parameters and variables. The bright mode is driven via the transmission line (port 1) and the output of the system is measured through the resonator (port 4). (b) Power spectral density measurements of in the $\Delta_{D3} = 0$ *case as a function dephasing rate. The gray lines indicate the positions of hybridized modes H1 and H2 as well as the bright mode B. (c) Power spectral density measurements of in the* $\Delta_{D3} = 60$ *MHz case s a function dephasing rate. The gray lines indicate the positions of qubit 3 Q3, dark mode D, and bright mode B. (d) Integrated power spectral densities of both* Δ_{D3} *cases as a function of noise power applied.*

again refer to them as H1 and H2. We observe that at no noise power applied no fluorescence is detected at all; only the bright mode is excited and at this large detuning it is effectively uncoupled from the resonator. The excitations are thus again localized away from the reaction center. With increased noise power we observe fluorescence at the frequencies of both hybridized modes; the noise thus again opens a channel between the bright mode and the two hybridized modes, not unlike the $\Delta_{23} = 50$ MHz scenario. The noise thus successfully assists transport through this cascaded network. At higher noise powers we observe that the amplitude of the fluorescence again decreases, in line with the QZE. However, it also appears to be located more in the upper hybridized mode H2; this might be attributed to a slightly imperfect hybridization between the dark mode and qubit 3.

6.2(c) shows similar measurements for the scenario in which the dark mode and qubit 3 are are detuned: $\Delta_{D3} = 60$ MHz. At this detuning the modes are again much less hybridized and behave more like the individual qubits. At no applied noise power we once more observe no fluorescence, in line with localization at the bright mode. For increased noise powers we initially observe fluorescence mostly at the dark mode, then at both at the dark mode and qubit 3, and for higher noise powers only at qubit 3. The noise thus successfully assists transport from the bright mode to qubit 3, potentially with the dark mode as an intermediate site. At even higher noise powers we then once more observe the QZE.

We again integrated the measured power spectral densities for each applied noise power, as depicted in figure 6.2(d). Here we observe that the $\Delta_{D3} = 0$ case behaves not unlike the $\Delta_{23} = 50$ MHz case. It starts from no output power and increasing to a maximum at moderate noise powers, before smoothly decreasing due to the QZE. It is another instance of noise assisted transport. Interesting is the comparison to the $\Delta_{D3} = 60$ MHz case: it exhibits the same overall trend, with a maximum at higher noise powers. This can be explained by the larger energy gap that needs to be bridged between the bright state and qubit 3. Moreover, while its maximal power is lower than for the $\Delta_{D3} = 0$ case it does eventually overtake it, leading to slightly higher powers. These results are interesting for two reasons: first it shows that a relatively large energy gap Δ_{B3} can be bridged with the assistance of noise, and in addition to that it shows that the energy level of the intermediate stage could theoretically be tuned to optimize the transport at a fixed noise power.

6.2 Phonon Antenna Mechanism

In the previous section we observed noise assisted transport both in the two qubit and the three qubit scenario. At this stage it is however not clear how the noise facilitates this transport; from the measurements it appears as if it induces transitions between detuned states, but such a mechanism is not obvious from the interaction with a white noise bath. Moreover, the phononic bath of FMO is also not white, but highly structured: its PSD consists of a number of Lorentzian peaks at different frequencies. As discussed in chapter 1 these peaks are one of the proposed mechanisms behind the transport, described in a framework known as the phonon antenna mechanism. The concept is that sites detuned by Δ are sensitive to features in the power spectral density at this frequency, and that the energy level structure of FMO might have evolved to benefit from these peaks.

In order to experimentally investigate this mechanism we do the opposite of the above: we fix the frequencies of the qubits and vary the center frequency Lorentzian power spectral density while measuring the energy transported through the system.

6.2.1 Two Qubit Scenario

We begin by studying this in the two qubit scenario depicted in figure 6.1(a), using the same parameters as in the white noise experiment. Figure 6.3(a) shows the result of such a measurement for $\Delta_{23} = 195$ MHz, where we varied the center frequency of fixed amplitude Lorentzian PSD noise with a full width at half maximum (FWHM) of 10 MHz, applied to flux line 2. We observe exactly what is predicted by the phonon antenna mechanism: the transport is maximal when the center frequency of the noise corresponds to Δ_{23}. This offers a possible explanation for how the white noise bath facilitates the transport, as it also has frequency components at Δ_{23}.

We subsequently investigated the dependence of the transport on the amplitude of a Lorentzian PSD centered at Δ_{23}, shown in figure 6.3(b) for $\delta_{23} = 85$ and 195 MHz. Here we observe similar behaviour as for the white noise measurements, with the three regimes of quantum localization, noise assisted transport and the quantum Zeno effect. Interesting is the comparison between the two detunings: we find that in order to bridge the larger energy gap stronger noise amplitudes are required, but that ultimately even higher transport powers can be achieved while also maintaining powers close to its maximum value for a much larger range of noise amplitudes. Further measurements could give insight into this mechanism.

The comparison with the powers measured for the white noise scenario (figure 6.1) is also of interest: we find that even for this high detuning between the qubits equivalent if not better transport powers can be achieved. This can be understood through the fact that the Lorentzian power spectral density only contains components at a beneficial frequency, whereas the white noise contains a large bandwidth of noise that only leads to detrimental dephasing of the system. Note however that we cannot quantify if the maximum is achieved at a similar noise power, as two different metrics are used.

6.2.2 Three Qubit Scenario

We subsequently study the same concepts in the three qubit setup depicted in figure 6.2(a). We again begin by studying the transport as a function of the Lorentzian noise power spectral density center frequency, shown in figure 6.4(a) for $\Delta_{DT} = 70$ MHz. In line with the two qubit experiment, we observe maxima in the transport when the power spectral density is centered at the frequency of one of the modes. Specifically, we observe a local maximum at

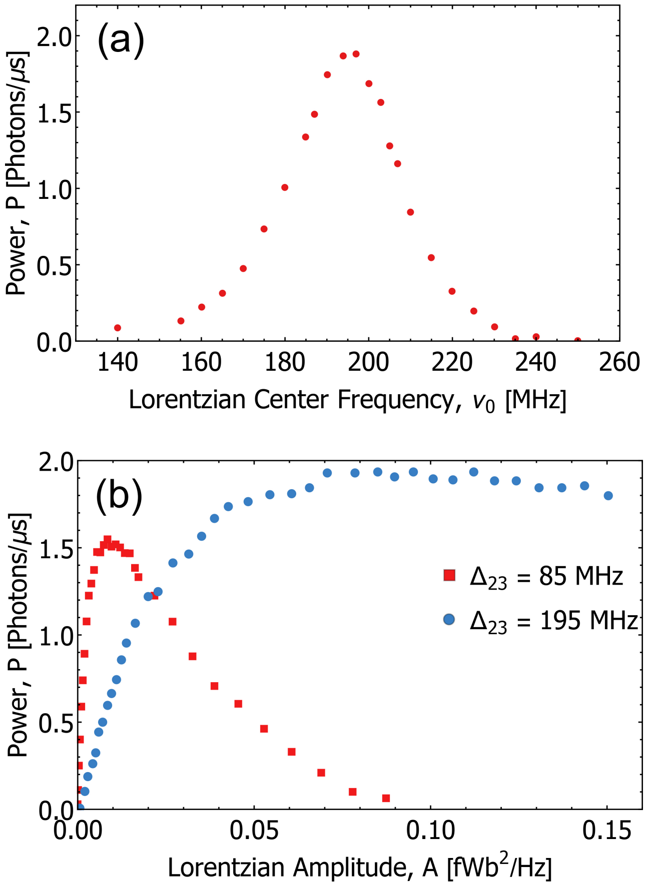

Figure 6.3: (a) Energy transport in the two site system for $\Delta_{23} = 195$ *MHz as a function of the center frequency of the Lorentzian power spectral density of the applied noise. (b) Energy transport for the two site system for two different detunings* Δ_{23} *as a function of the amplitude of the Lorentzian power spectral density noise, centered at* Δ_{23}*.*

the detuning between the bright mode and the dark mode $2J_{12} = 175$ MHz, while we find a global maximum at the detuning between the bright mode and qubit 3: $\Delta_{B3} = 245$ MHz. It is not surprising that this transport channel is more efficient than through the dark mode; as Δ_{D3} is significant compared to $J_{D3} = 19$ MHz the dark mode is essentially uncoupled from the resonator and without any frequency components around Δ_{D3} the noise cannot assist transport from the dark mode to qubit 3 in order to bridge this energy gap. These measurements thus provide a strong indication of how sensitive the transport is to the structure of the enviroment.

In figure 6.4(b) we subsequently study the Lorentzian amplitude dependence of the transport for a noise PSD centered at Δ_{B3}, where we once again observe all three phases of noise assisted transport. Moreover, its comparison to figure 6.2 shows that the Lorentzian noise power spectral density leads to a maximal transport that is more than twice as high as what is achieved with white noise, verifying that a structured noise environment can lead to significant improvements in transport.

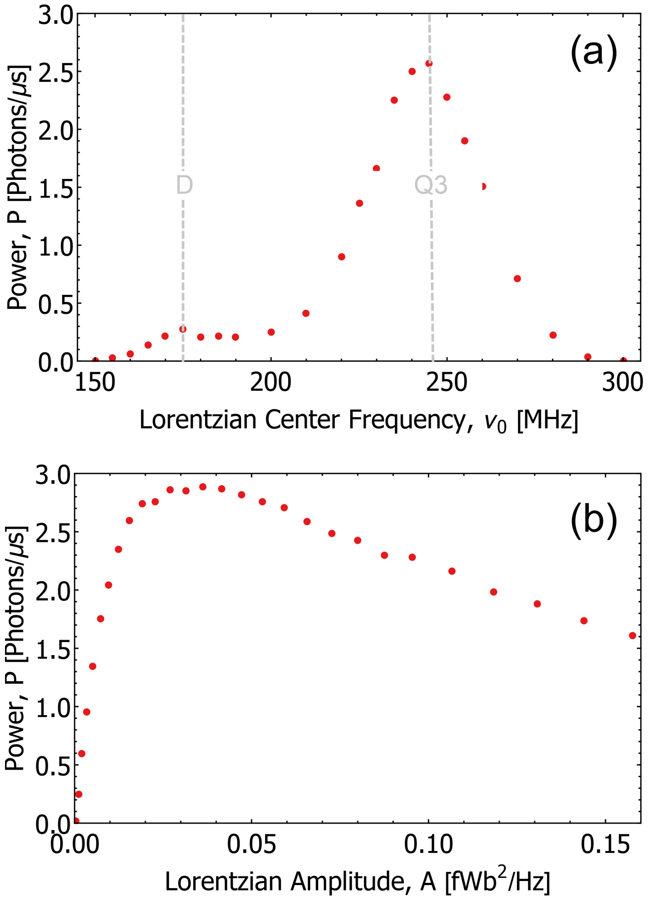

Figure 6.4: (a) Energy transport in the three site system for $\Delta_{D3} = 75$ MHz as a function of the center frequency of the Lorentzian power spectral density of the applied noise. (b) Energy transport for the three site system as a function of the amplitude of the Lorentzian power spectral density noise, centered at Δ_{B3}. The dark mode and qubit 3 are indicated with gray dashed lines.

6.3 Remaining Measurements

At this stage we have covered the experiments performed during this thesis. However, it should be noted that the project itself has not been concluded: there are still several measurements of interest remaining that can be done without any adjustments to the setup. The simplest of these is performing the above experiments at a number of other detunings Δ_{jk} in order to observe trends in the dependence of the transport on this disorder. In addition to this we intend to explicitly compare our results to theoretical simulations of the system.

A more involved measurement we aim to do is to study the three qubit network in the presence of even more structured noise, in the form of a power spectral density of multiple Lorentzian peaks centered at more than a single transition. An example of this would be a three peaked structure, with Lorentzians at Δ_{BD}, Δ_{D3} and Δ_{B3}. As this is reminiscent of what is observed in the environment of FMO, it could provide insight into whether a cascading network of site levels can be used to optimize transport in such an environment, making use of all frequency components available.

Furthermore, at this stage we have only studied the energy successfully transported through the system, neglecting any photons re-emitted into the transmission line by qubits 1 and 2. In a subsequent set of measurements we aim to characterize these losses so that one can define an actual efficiency for our system, given in terms of photons successfully transported from the transmission line to the resonator per photon absorbed by the qubits. This is equivalent to the internal quantum efficiency of solar cells and it is essentially the figure of merit for the performance of an FMO-type structure.

In the near future a number of more complicated measurements could also be performed with this setup or a slight variation of it, however these will be discussed in the outlook of the next chapter.

Chapter 7

Conclusions & Outlook

In this thesis we have studied a number of concepts. We began with a general treatment of the literature surrounding light-harvesting structures found in nature, focusing on the protein-pigment complex of green sulfur bacteria known as the Fenna-Matthews-Olson complex (FMO). A topic of much recent interest, it is able to transport excitations from its antenna complex to its reaction center with near 100% efficiency. In 2007 research by Fleming *et al.* found evidence for quantum coherences in this transport, indicating that it might be quantum mechanics that underlies these high efficiencies. Subsequent work has focused on researching how such quantum coherences might persist even in room temperature conditions, and they found that the highly structured noise environment of FMO might hold the key to explaining these phenomena.

However, dealing with such open quantum systems of many interacting degrees of freedom has proven intractable on modern classical computers, inspiring Mostame *et al.* to propose exploring such a system in an analog quantum simulator. They proposed to do so in the superconducting architecture due to its high degree of parameter control, using a number of qubits coupled to an environment of quantum harmonic oscillators to recreate the structure of FMO.

In this thesis we have explored a variant of such a system, using the superconducting architecture to create a network of three transmon qubits coupled to coplanar waveguides in order to mimic the transport of excitations from an antenna complex to a reaction center in the presence of a noise environment. Importantly this noise environment was not formed by a collection of harmonic oscillators but instead by a time varying magnetic flux. This allowed us to study the system in the classical noise approximation known as the Haken-Strobl-Reinker model, a high temperature variant of the quantum bath proposed.

We began the thesis with a treatment of the theory governing the superconducting architecture in chapter 2, after which we discussed the design and fabrication considerations considered in making such a system in chapter 3. This system was then studied in the experimental setup detailed in chapter 4 and fully characterized as discussed in chapter 5. We found that the designed Hamiltonian parameters were successfully achieved with a high degree of precision, and that many of the variable parameters could be accurately tuned to explore different scenarios.

The first of these scenarios was a two site model consisting of qubits 2 and 3. Here we studied the transport from the transmission line to the resonator through the qubits as a function of dephasing induced by a white noise environment, in which we showed the first experimental verification of noise assisted transport in a network of quantum mechanical elements. This phenomena was then also observed in the more complicated geometry of three different sites.

However, the noise environment of FMO has been found to be highly structured, in contrast to the explored white noise environment. Following the concept of the theoretical phonon antenna mechanism we subsequently explored transport through the system in the presence of a noise environment that had a Lorentzian power spectral density, reminiscent of the peaked features of the FMO environment. Here we showed that such peaked power spectral densities indeed lead to an increased transport efficiency when they are centered at the energy mismatch between two sites, experimentally verifying the validity of the phonon antenna mechanism. Furthermore it illustrates a mechanism for understanding how a typically detrimental noise environment can instead lead to enhanced transport, giving insight into how FMO might be able to achieve its remarkable efficiencies.

As discussed at the end of chapter 6 we have not yet exhausted all scenarios of interest that can be studied with the current setup, as several more white noise and Lorentzian power spectral density scenarios can be explored in order to gain further insight into the system. However, we also propose a number of follow up experiments that can be explored in such a system in the near future. A major open question in the literature is whether such noise assisted transport can also occur in the presence of incoherent excitations, such as those that drive actual photosynthesis. Up to now we have not explored such physics as we excited our qubits with a coherent microwave drive. However, it is well within the capabilities of the experimental setup to instead drive the qubits incoherently, giving insight into such physics.

Furthermore we have not touched upon coherences in the system or their role in the transport itself. Although we known the system studied in this thesis is fundamentally capable of hosting such coherences, their quantification at different stages of transport is not obvious. One way to look into this would be by studying photon statistics at the output of the resonator, providing a way to quantify the non-classical properties of the output as a function of noise environment. These measurements are also well established in this group and could be performed in the same setup.

Yet another such scenario would be exploring the single photon regime of our system. As of now we have looked at the transport for $\Omega_j \approx \Gamma_j$, where the driving rate was roughly equal to the loss rate of the qubits, but one can instead imagine lowering the driving rate such that only a single excitation is present in the system at a time, which is thought to be the case for FMO due to the low light environment green sulfur bacteria live in. Such a measurement is also readily explored in this setup by introducing parametric amplifiers to increase the signal strength measured at the resonator output

Finally one can think about adjusting the topology of the system, introducing the proposed harmonic oscillators to simulate the effect of a quantum bath and eventually scaling up the system to all eight sites of FMO, replicating the full system. While experimentally challenging, the superconducting architecture used in this thesis forms no obstacles in doing so due to its scalability and high degree of parameter control.

Appendix A

The Relationship Between a Phononic Bath and Classical noise

In chapter 1 we introduced how the Hamiltonian of the FMO complex is typically described by the independent boson model:

$$\hat{\mathcal{H}}_{Tot} = \frac{1}{2}\sum_{j=1}^{N}\left[\varepsilon_j \hat{\sigma}_{z,j} + \sum_{k>j} V_{jk}\left(\hat{\sigma}_j^{+}\hat{\sigma}_k + \hat{\sigma}_k^{+}\hat{\sigma}_j\right)\right] + \sum_{j=i}^{N}\sum_{l}\hbar\omega_l^j\left(\hat{a}_l^{\dagger,j} + \hat{a}_l^j + 1/2\right)$$
$$+ \sum_{j=1}^{N}\hat{\sigma}_{z,j}\left[\sum_l \chi_{jl}\left(\hat{a}_l^{\dagger,j} + \hat{a}_l^j\right)\right] \quad \text{(A.1)}$$

We then went on to motivate that we do not study a system of this form in this thesis due to several experimental considerations, such as the physical size of the harmonic resonators proposed to simulate the above bath. The suggested alternative was studying the system in the classical noise approximation, where the quantum environment is replaced by time-dependent fluctuations of transition energies in the Haken-Strobl-Reineker (HSR) model. In this model $\hat{\mathcal{H}}_{Tot}$ is replaced by the time dependent Hamiltonian

$$\hat{\mathcal{H}}(t) = \frac{1}{2}\sum_{j=1}^{N}\left[\left(\varepsilon_j + \delta\varepsilon_j(t)\right)\hat{\sigma}_{z,j} + \sum_{k>j} V_{jk}\left(\hat{\sigma}_j^{+}\hat{\sigma}_k + \hat{\sigma}_k^{+}\hat{\sigma}_j\right)\right] \quad \text{(A.2)}$$

where all of the bath dynamics are now contained in the (classical) fluctuating transition energy term $\delta\varepsilon_j(t)$.

As noted in the main text, at first sight this Hamiltonian appears to contain much less complexity than the originally proposed quantum bath. However, in this appendix we now derive that these two models can be seen as equivalent in the high temperature limit $k_B T \gg \omega_l$ by choice of the proper time varying signal governing $\delta\varepsilon_j(t)$. To do so we will illustrate how this is done with the reduced system of a single site in terms of a qubit, which can then be extended to N sites as found in the above Hamiltonian.

A.1 Classical Noise Approximation

In this section we will follow the derivation described in [64], for which we will set $\hbar = 1$. We start from the classical noise approximation known as the HSR model, where the Hamiltonian of a single qubit is given by

$$\hat{\mathcal{H}}(t) = \frac{1}{2}\left[\omega_0 + \delta\omega(t)\right]\hat{\sigma}_z \tag{A.3}$$

where ω_0 is the fixed qubit resonance frequency and $\delta\omega(t)$ describes time dependent fluctuations in the environment. These fluctuations are typically parameterized by some noise environment described by a random variable X generating events $x(t)$: $\delta\omega(t) = f(x(t))$. Essential to our description of the effect of $\delta\omega(t)$ is that X has a specific probability distribution governing the amplitudes of the events $x(t)$, as well as a power spectral density governing the correlations between subsequent events. It is therefore instructive to briefly introduce these concepts, which we do in the next section.

A.1.1 Statistical Properties of X

The amplitude distribution of the events $x(t)$ of the random variable X is fully characterized by either defining all of the statistical moments $E\left[X^m\right]$, or by specifying the probability density function $f_X(x)$. It is defined as

$$\text{Probability}\left[a \leq x \leq b\right] = \int_a^b f_X(x)dx \tag{A.4}$$

An example of this is the ubiquitous Gaussian distribution function given by

$$f_X(x|\mu,\sigma) = \frac{1}{\sqrt{2\sigma^2\pi}}\exp\left(-\frac{(x-\mu)^2}{2\sigma^2}\right) \tag{A.5}$$

where $\mu = E\left[X\right]$ is its mean and $\sigma^2 = E\left[(X-\mu)^2\right]$ is the variance. It is important to note that for a generic random variable this probability distribution can vary with time. However, as motivated in the section on the phononic bath, the random variables studied in this thesis do not have such time dependence so that $f_X(x)$ is fixed.

Such random variables are said to be wide-sense stationary (WSS), a property of random variables that satisfy two requirements: its mean function $\mu(t) = E\left[X\right]$ is constant for all times, and its autocovariance function $C_X\left(t,t'\right)$ defined as

$$C_X(t,t') = E\left[(x(t)-\mu(t))(x(t')-\mu(t'))\right] \tag{A.6}$$

does not depend on the specific times t and t', but only on the time lag $\tau = t - t'$. It can therefore be written as

$$\gamma_X(\tau) = E\left[(x(t)-\mu)(x(t+\tau)-\mu)\right] \tag{A.7}$$

The autocavariance function is a measure of how correlated terms of the random variable are at different times. It is these correlations that contain the information of interest for quantifying the temporal properties of noise; they can for example be used to define the textbook example of noise, white noise [65]:

Definition A.1 *The events $x(t)$ produced by a random variable X are white if X is wide sense stationary, has zero mean, nonzero variance σ^2, and autocovariance function $\gamma_X(\tau) = \sigma^2\delta_{0\tau}$.*

In the above, δ_{ij} is the Kronecker delta. White noise is often taken as the definition of uncorrelated: the values of $X(t)$ do not follow any trends at any time lags τ, making it a memory-less, uncorrelated process.

However in literature noise is typically quantified by its power spectral density $S_X(\omega)$ rather than through the autocovariance. It is a distribution that describes how the power of a time series is distributed in frequency space rather than in time. Note that this name is mostly based on convention; while the distribution can be an actual physical power, it is often simply identified with the squared value of the quantity in question. If it is indeed a power it typically has units of dBm/s/Hz, or simply power, and its integral over a certain frequency range gives how much energy is contained in that bandwidth.

In order to connect the autocovariance to the power spectral density the stochastic process generally has to meet several conditions. Most of these are trivially met for WSS processes, and the quantities can then related through the Wiener-Khinchin theorem [66]:

Definition A.2 *If X is a WSS process with zero mean and an absolutely integrable autocovariance function $\gamma_X(\tau)$, its power spectral density is given by*

$$S_X(\omega) = \mathcal{F}\left[\gamma_X(\tau)\right] = \frac{1}{2\pi}\int_{-\infty}^{\infty} d\tau\, e^{-i\omega\tau}\gamma_X(\tau) \tag{A.8}$$

where $\mathcal{F}[\dots]$ is the Fourier transform. The theorem thus states that the two quantities of interested are a Fourier pair, given that the necessary conditions for inversion are met.

If we now apply the definition of white noise (definition A.1) to that of the power spectral density (definition A.2), we see that for white noise $S_X(\omega) = \mathcal{F}[\sigma^2\delta_{0\tau}] = \sigma^2$. The power spectral density is thus independent of frequency, which is why white noise is referred to as having a flat power spectral density. Note that its integral would be infinite; true white noise therefore does not exist in nature.

A.1.2 HSR Model

With the above definition of the probability density function and the power spectral density we have quantified the amplitude distribution and the temporal properties of the noise of interest. We can now return to the description of the HSR model, governed by the Hamiltonian

$$\hat{\mathcal{H}}(t) = \frac{1}{2}\left[\omega_0 + \delta\omega(t)\right]\hat{\sigma}_z \tag{A.9}$$

The time evolution operator of this Hamiltonian is given by

$$\hat{U}(t) = \exp\left(-i\int_0^t ds\hat{\mathcal{H}}(s)\right) = \exp\left(-\frac{i}{2}\left[\omega_0 t + \phi(t)\right]\hat{\sigma}_z\right) \tag{A.10}$$

where we defined the new random variable $\phi(t) = \int_0^t ds\delta\omega(s)$.

For the sake of generality we now look at the evolution of this system in terms of its density matrix; an alternative picture in terms of evolution on the Bloch sphere can be found in [67]. Given some fixed initial condition $\rho(0)$ its evolution is given by $\hat{\rho}(t) = \hat{U}(t)\rho(0)\hat{U}^\dagger(t)$. Since $[H, \hat{\sigma}_z] = 0$ one finds that the populations of $\hat{\rho}(t)$ in the eigenbasis of $\hat{\sigma}_z$ are constant, while the off-diagonal elements $\hat{\rho}_{01}(t) = \hat{\rho}^*_{10}(t)$ are given by

$$\hat{\rho}_{01}(t) = e^{i\omega_0 t}e^{i\phi(t)}\rho_{01}(0) \tag{A.11}$$

Given a single realization of $\delta\omega(t)$ we can then compute the value of $\hat{\rho}_{01}(t)$ given the above. However, in an experiment one does not observe a single one of these realizations. Instead one averages over many identically prepared copies of the system. What we are thus interested in is

$$\left\langle e^{i\phi(t)}\right\rangle = e^{-\Gamma(t)} \tag{A.12}$$

where the angular brackets denote averaging over many iterations of the noise and $\Gamma(t)$ is known as the decoherence function.

From this one can derive the exact (non-Markovian) master equation of $\rho(t) = \langle\hat{\rho}(t)\rangle$ to be given by

$$\dot{\rho} = -\frac{i}{2}\left(\omega_0 - \Sigma(t)\right)\left[\hat{\sigma}_z, \rho\right] + \frac{\gamma_\phi(t)}{2}\left(\hat{\sigma}_z\rho\hat{\sigma}_z - \rho\right) \tag{A.13}$$

where $\Sigma(t) = \mathrm{Im}\left[\dot{\Gamma}\right]$ is an energy shift and $\gamma_\phi(t) = \mathrm{Re}\left[\dot{\Gamma}\right]$ is the pure dephasing rate. The time dependence of the noise is thus fully absorbed into $\Sigma(t)$ and $\gamma_\phi(t)$.

In order to continue the derivation we note that the decoherence function is essentially equal to the cumulant-generating function $K(t)$ [68]

$$K(t) = \log\left(\left\langle e^{tX}\right\rangle\right) \tag{A.14}$$

where X is the probability distribution of the relevant random variable. For example, if X is a Gaussian random variable with a vanishing mean $\mu = 0$ and variance σ^2, one can use equation A.5 to find that $K(t) = t^2\sigma^2/2$ by writing out the Taylor expansion of $K(t)$.

We can now relate this to the decoherence function of equation A.12 by noting that it is a cumulant-generating function with tX given by $i\phi(t) = i\int_0^t ds\delta\omega(s)$. If we thus assume the random variable X parametrizing $\delta\omega(t)$ to be a Gaussian process (the choice for which is motivated in the next section), we find that the decoherence function is given by the autocovariance function of $\delta\omega(t)$:

$$\Gamma(t) = \frac{1}{2}\int_0^t ds \int_0^t ds' \, \langle \delta\omega(s)\delta\omega(s')\rangle \tag{A.15}$$

If we then further assume that $\delta\omega(t)$ is WSS we can write $\langle \delta\omega(s)\delta\omega(s')\rangle = \gamma_X(s-s')$ so that

$$\Gamma(t) = \frac{1}{2}\int_0^t d\tau \int_{-\tau}^{\tau} d\tau' \gamma_X(\tau') \tag{A.16}$$

where we used a change of variables $\tau = s + s'$ and $\tau' = s - s'$. From this it is clear that $\Sigma(t) = 0$, and from standard calculus it follows that

$$\gamma_\phi(t) = \frac{1}{2}\int_{-t}^{t} d\tau \gamma_X(\tau) = \int_{-\infty}^{\infty} d\omega \, \frac{\sin(\omega t)}{\omega} S_X(\omega) \tag{A.17}$$

where we introduced the power spectral density of $\delta\omega(t)$ parametrized by the random variable $X(t)$. It is interesting to see that low frequency flux noise contributes the most to the magnitude of the pure dephasing rate, due to the $1/\omega$ dependence of equation A.17.

The above gives us an exact expression for the master equation of the system in the presence of a fluctuating transition frequency $\delta\omega(t)$ with an arbitrary power spectral density $S_X(\omega)$. Moreover, while we assumed the noise to be Gaussian, one can perform the same calculation for any probability distribution by calculating the relevant cumulants.

A.2 Independent Boson Model

Now that we have derived how one treats the effect of the classical noise approximation we turn to a treatment of the independent boson model. For this we follow the derivation found in [69] and again simplify our system to a single qubit. However, we make no such assumptions about the bath; it still consists of l harmonic oscillators. The system thus has the Hamiltonian

$$\hat{\mathcal{H}}_{Tot} = \hat{\mathcal{H}}_S + \hat{\mathcal{H}}_B + \hat{\mathcal{H}}_{S-B} = \frac{\omega_0}{2}\hat{\sigma}_z + \sum_k \omega_k a_k^\dagger a_k + \hat{\sigma}_z \sum_k \chi_k (a_k + a_k^\dagger) \tag{A.18}$$

The interaction term can also be written as $\hat{\sigma}_z\hat{X}$, where $\hat{X} = \sum_k \chi_k(a_k + a_k^\dagger)$ is the collective bath coordinate.

At this stage we can already motivate replacing such a bath by a classical noise field, illustrated as follows. We begin by moving into the interaction picture generated by $\hat{\mathcal{H}}_S + \hat{\mathcal{H}}_B$ so that the Hamiltonian becomes time dependent and takes the form

$$\hat{\mathcal{H}}_{SB}(t) = \hat{\sigma}_z\hat{X}(t) \tag{A.19}$$

with

$$\hat{X}(t) = \sum_k \chi_k(e^{-i\omega_k t}a_k + e^{i\omega_k t}a_k^\dagger) \tag{A.20}$$

We now assume that the bath starts in a thermal state

$$\rho_B = e^{-\beta\hat{\mathcal{H}}_B}/\mathcal{Z} \tag{A.21}$$

with $\beta = 1/k_B T$ and $\mathcal{Z} = \mathrm{Tr}[e^{-\beta\hat{\mathcal{H}}_B}]$ being the partition function. From this one can find that $\langle\hat{X}(t)\rangle = \mathrm{Tr}[\hat{X}(t)\rho_B] = 0$; the collective bath coordinate thus has zero mean. However, its fluctuations do not vanish as seen from its autocorrelation function

$$\langle\hat{X}(t)\hat{X}(t')\rangle = \int_{-\infty}^{\infty} d\omega\, e^{-i\omega(t-t')}S(\omega) \tag{A.22}$$

where $S(\omega)$ is now a temperature dependent power spectral density defined by

$$S(\omega) = \begin{cases} J(\omega)[1+n(\omega)] & (\omega > 0) \\ J(|\omega|)n(|\omega|) & (\omega < 0) \end{cases} \tag{A.23}$$

where $n(\omega) = (e^{\beta\omega} - 1)^{-1}$ is the Bose-Einstein distribution governing the temperature dependence and the zero temperature power spectral density is

$$J(\omega) = \sum_k |\chi_k|^2\delta(\omega - \omega_k) \tag{A.24}$$

We have chosen the notation $S(\omega)$ in analogy with the previously introduced $S_X(\omega)$ to make it clear that one should compare these two functions and not $J(\omega)$ itself. In addition to this the thermal state implies that the statistics of $\hat{X}(t)$ is Gaussian, motivating the choice of this distribution made in the previous section.

The above thus motivates how one could imagine replacing $\hat{X}(t)$ in the above Hamiltonian with a classical zero-mean noise field having Gaussian statistics and power spectral density $S(\omega)$. However, in general this ignores the dynamics of the quantum bath itself that is perturbed by the interaction with the system. While this is not negligible for a general quantum bath, we now show that such an assumption does hold for the independent boson model.

In order to do so we attempt to solve the evolution of the qubit's reduced density matrix $\rho_S(t) = \mathrm{Tr}_B[U(t)\rho(0)U^\dagger(t)]$, where we trace out the bath degrees of freedom and again define $U(t)$ to be the time evolution operator, for which we assume that the initial state of the system is $\rho(0) = \rho_S(0) \otimes \rho_B$.

For most quantum systems one would now run into time-ordering complications when dealing with $U(t)$, governed by the time-ordering operator $\mathcal{T}$. For bosons it is defined as

$$\mathcal{T}\left\{A(t)B(t')\right\} = \begin{cases} A(t)B(t') & (t > t') \\ B(t')A(t) & (t < t') \end{cases} \tag{A.25}$$

However, for our system this is not the case: $[\hat{X}(t), \hat{X}(t')]$ commutes with all the other terms in the Hamiltonian so that one can use the Magnus expansion [70] to write that

$$\begin{aligned} U(t) &= \mathcal{T}\left\{\exp\left(-i\int_0^t ds\ \hat{\mathcal{H}}_{SB}(s)\right)\right\} \\ &= \exp\left(-i\int_0^t ds\ \hat{\mathcal{H}}_{SB}(s) - \frac{1}{2}\int_0^t ds \int_0^s ds'\ [\hat{\mathcal{H}}_{SB}(s), \hat{\mathcal{H}}_{SB}(s')]\right) \end{aligned} \tag{A.26}$$

In the above the second term simply leads to a global phase and it can thus simply be dropped, so that we can use equation A.19 to find that

$$U(t) = \exp\left\{\frac{1}{2}\hat{\sigma}_z \sum_k \left[\alpha_k(t)a_k^\dagger - \alpha_k^*(t)a_k\right]\right\} \tag{A.27}$$

where we introduced

$$\alpha_k(t) = \frac{2\chi_k(1 - e^{i\omega_k t})}{\omega_k} \tag{A.28}$$

The above can be made more transparent by introducing the displacement operator

$$\hat{D}(\alpha) = \exp\left(\alpha\hat{a}^\dagger - \alpha^*\hat{a}\right) \tag{A.29}$$

to write our time evolution operator in its final form

$$U(t) = |1\rangle\langle 1| \prod_k D(\alpha_k/2) + |0\rangle\langle 0| \prod_k D(-\alpha_k/2) \tag{A.30}$$

This tells us that $U(t)$ describes a time-dependent displacement of each mode by an amount $\pm\alpha_k(t)/2$ conditional on the state of the qubit.

In terms of the actual time evolution of the system we now again use that $[\hat{\mathcal{H}}, \hat{\sigma}_z] = 0$ to find that the populations in the eigenbasis of $\hat{\sigma}_z$ are constant, while the off-diagonal elements decay as $\rho_{01}(t) = e^{-\Gamma(t)}\rho_{01}(0)$ where we recover the decoherence function. Here it is given by

$$e^{-\Gamma(t)} = \left\langle \prod_k D(\alpha_k) \right\rangle_B \tag{A.31}$$

where the expectation value is with respect to the bath. As in the classical scenario one can now use that $\Gamma(t)$ is essentially the cumulant generating function of the random variable $\sum_k (\alpha_k a_k^\dagger - \alpha_k^* a_k)$, which due to its Gaussian statistics can again be expressed in the form of the correlation function. For the bosonic bath this takes the form

$$\begin{aligned}\Gamma(t) = \sum_k \frac{4|\chi_k|^2}{\omega_k^2}[1 - \cos(\omega_k t)] \coth\left(\beta\omega_k/2\right) \\ = \int_{-\infty}^{\infty} d\omega \, \frac{4[1-\cos(\omega t)]}{\omega^2} S(\omega)\end{aligned} \tag{A.32}$$

where $S(\omega)$ is the previously introduced temperature dependent power spectral density.

This can be used to find that once again $\Sigma(t) = 0$ and

$$\gamma_\phi(t) = \int_{-\infty}^{\infty} d\omega \, \frac{\sin(\omega t)}{\omega} S(\omega) \tag{A.33}$$

so that the final system can be described as

$$\dot{\rho} = -\frac{i}{2}\omega_0[\hat{\sigma}_z, \rho] + \frac{\gamma_\phi(t)}{2}\left(\hat{\sigma}_z \rho \hat{\sigma}_z - \rho\right) \tag{A.34}$$

in complete analogy with the classical noise bath. Explicit comparison of the two scenarios shows that the evolution of the independent boson model is thus equivalent to that produced by a classical noise environment with stationary Gaussian statistics and a power spectral density $S_X(\omega) = S(\omega)$. This last factor is the only remaining complication: as given in equation A.23 the quantum bath has a power spectral density that is asymmetric around $\omega = 0$, which is not possible for a (real) classical noise signal. Based on this we can thus conclude that the classical noise environment is a good approximation only in the high temperature limit, where $n(\omega) \gg 1$ and $S(\omega)$ is approximately even.

Appendix B

Calculating the Hamiltonian Parameters

In chapter 2 we discussed the general derivation of the Hamiltonian of the combined system, consisting of the transmission line, three transmons and the coplanar waveguide resonator. Its circuit representtion is repeated in figure B.1 for convenience. We derived that its Hamiltonian could be written as

$$\mathcal{H} = \frac{1}{2}Q^T\underline{C}^{-1}Q + \frac{1}{2}\Phi^T\underline{L}^{-1}\Phi \tag{B.1}$$

where $\underline{L}$ is a matrix of inductances, $\underline{C}$ a matrix of capacitances,

$$\dot{\Phi}^{\mathrm{T}} = [\phi_1, \phi_2, \cdots, \phi_N, \varphi_1, \varphi_2, \varphi_3, \psi] \tag{B.2}$$

are the fluxes, and

$$Q^{\mathrm{T}} = [p_1, p_2, \cdots, p_N, q_1, q_2, q_3, r] \tag{B.3}$$

are the conjugate momenta. For convenience we repeat that ϕ and p refer to the transmission line, φ and q to the transmons, and ψ and r to the CPW resonator.

We then went on to discuss this Hamiltonian in the second quantization formalism, using factors such as the qubit frequencies ω_j, their couplings J_{jk}, the coupling to the resonator g_{jr} and the coupling to the transmission line b_{jt}. While these quantities have simple closed form expressions in the case of a system consisting of only the two relevant components (see for example [39, 46]) the combined system is more difficult to treat due to the capacitive contributions each element has on one another.

In this appendix we show how one can approximate such a combined system in order to calculate expressions for the relevant Hamiltonian parameters, which can then be used in simulations to accurately design a system

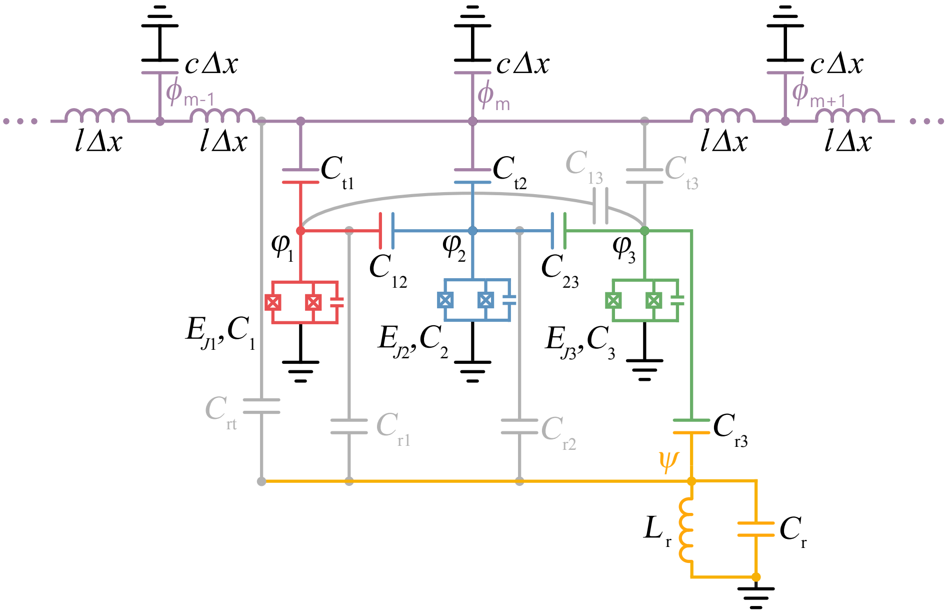

Figure B.1: Circuit diagram of the system studied in this thesis. It consists of a CPW transmission line (purple), three transmon qubits (red, blue, green) and a CPW resonator. Designed couplings are shown in the color of the involved elements, while stray couplings are shown in gray. The flux coordinates of these elements are also denoted, with ϕ_m being the transmission line flux coordinate, φ_j the coordinate of transmon j and Ψ the coordinate of the CPW resonator.

with the desired properties as described in chapter 3. Most notably, we have to make two approximations: we need to treat both the transmission line and the CPW resonator as finite dimensional structures so that we end up with finite dimensional matrices $\underline{C}$ and $\underline{L}$.

For the CPW resonator this is already implicit in the above, where we treat is as an effective LC circuit with $C_r = \frac{cd}{2}$, $L_r = \frac{2ld}{\pi^2}$ and $Z_r = \frac{2}{\pi}\sqrt{\frac{l}{c}}$. For the transmission line the approach is more complex; in principle it has to be treated as a distributed element system, but we will that it is fabricated such that $Z_t = 50\ \Omega$. If we then calculate an approximate C_t based on ANSYS Maxwell simulations we define an effective L_t, reducing our system to the finite dimensional matrices

$$\underline{C} = \begin{pmatrix} C_r + \sum_j C_{rj} & -C_{rt} & -C_{r1} & -C_{r2} & -C_{r3} \\ -C_{rt} & C_t + \sum_j C_{tj} & -C_{t1} & -C_{t1} & -C_{t3} \\ -C_{r1} & -C_{t1} & C_1 + \sum_j C_{1j} & -C_{12} & -C_{13} \\ -C_{r2} & -C_{t2} & -C_{12} & C_2 + \sum_j C_{2j} & -C_{23} \\ -C_{r3} & -C_{t3} & -C_{13} & -C_{23} & C_3 + \sum_j C_{3j} \end{pmatrix} \tag{B.4}$$

$$\underline{L} = \begin{pmatrix} L_r & 0 & 0 & 0 & 0 \\ 0 & L_t & 0 & 0 & 0 \\ 0 & 0 & L_1 & 0 & 0 \\ 0 & 0 & 0 & L_2 & 0 \\ 0 & 0 & 0 & 0 & L_3 \end{pmatrix} \tag{B.5}$$

where the first column describes the resonator, the second column the transmission line and the remaining three columns the three transmons. In the above the summations $\sum_j C_{ij}$ are over the elements $i \neq j$.

Based on the derivations found in [39, 46] and calculations done by Dr. Anton Potočnik we can use the above matrices to calculate all of the second quantization Hamiltonian parameters. To do so we will use m to denote mth transmon and $\underline{C}_{jk}^{-1}$ to indicate the element on the jth row and kth column of the inverted capacitance matrix. From this one finds that

$$E_{Jm} = \left(\frac{\Phi_0}{2\pi}\right)^2 \frac{1}{\underline{L}_{mm}} \tag{B.6}$$

$$E_{Cm} = \frac{e^2 \underline{C}_{jj}^{-1}}{2} \tag{B.7}$$

$$\omega_m = \sqrt{8E_{Cm}E_{Jm}} - E_{Cm} \tag{B.8}$$

$$J_{mn} = \frac{\underline{C}_{mn}^{-1}}{2} \left(\frac{1}{\underline{C}_{mm}^{-1}\underline{L}_{mm}\underline{C}_{nn}^{-1}\underline{L}_{nn}}\right)^{1/4} \tag{B.9}$$

$$b_{mt} = \frac{Z_t}{2} \frac{\left(\underline{C}_{2m}^{-1} C_t\right)^2}{\underline{L}_{mm}} \tag{B.10}$$

$$g_{mr} = \frac{\underline{C}_{1m}^{-1}}{2Z_r} \left(\frac{1}{\underline{C}_{mm}^{-1}\underline{L}_{mm}}\right)^{1/4} \tag{B.11}$$

where we assume that Z_r and Z_t are unaffected by the perturbations caused by the other elements.

With the above one can calculate all of the relevant system parameters, given the systems capacitance and inductance matrix. These can be simulated using ANSYS Maxwell as described in chapter 3.

Appendix C

Designing Flux Noise

As discussed in chapter 3, we digitally design and physically implement flux noise with arbitrary power spectral density functions in our system. In this appendix we quantitatively treat how this is done for flux noise $Phi(t)$ with arbitrary spectral densities $S_\Phi(f)$ and probability distribution $f_\Phi(\phi)$.

Before we begin we should note that while in general the designed noise series can be continuous, this chapter we will only consider series consisting of a finite or countable number of elements: the class of discrete-time time series. This is because the noise of interest in our experiments is ultimately implemented by an arbitrary waveform generator, which has a discrete-time input and output. To make the discretization apparent, we denote the sequence of events as $\Phi[t]$, in contrast to $\Phi(t)$ used for a continuous series of events.

C.1 Digitally Generating Noise

We start with the description of how to generate a digital time series $x[t]$, governed by a random variable X with the desired properties. Generating events with just the desired probability distribution is not challenging; every major mathematical software package has built in features for random number generation with specific distributions, and those that are not included can be defined manually. However, the temporal relationship between the events (captured by $S_X(f)$) is more difficult to construct. While some specific densities can be generated using tailored algorithms [71, 38], we choose instead to construct a recipe that allows one to digitally generate any desired $S(f) = A(f)$. This is done by generating white noise with a unit power spectral density $S_X(f) = 1$ and digitally filtering it into the desired form.

We start by generating the white noise. In appendix A we defined what it is for a general random variable X to be white: it has to be wide sense stationary (WSS), have zero mean, nonzero variance σ^2, and autocovariance function $\gamma_X[h] = \sigma^2 \delta_{0h}$ which means it has to be uncorrelated in time. If this is satisfied, the time series $x[t]$ has power spectral density $S_X(f) = \sigma^2$.

In appendix A we discussed that the WSS property itself is satisfied if $x[t]$ is generated from a random variable X whose probability distribution does not vary in time, which is the case for events generated numerically from a fixed distribution. Moreover, if one chooses to generate the time series $x[t]$ by drawing the events from X independently with a finite second moment $E[X^2]$, one can prove that they are also uncorrelated [72].

Therefore all that is required to generate white noise with $S_X(f) = \sigma^2$ is to draw independent events from a random variable X with zero mean $E[X[t]] = 0$ and finite second moment $E[X[t]^2]$. To obtain a time series $x[t]$ of length n with $S_X(f) = 1$ one could thus independently draw n samples from a Gaussian distribution with zero mean and unit standard deviation, which can be done with every major mathematical computation program. In this thesis we choose to use Wolfram Mathematica.

In order to change the above unit power spectral density to any desired $S_X(f) = A(f)$ we apply a digital filter. Specifically, the white noise is filtered with a linear time-invariant (LTI) digital filter: a filter for which the relationship between input and output is a linear and time invariant map [73]. One can show that such a filter can be fully described by a single function, $h[t]$, called the impulse response function: the image of the Kronecker delta under the linear map of the filter [73]. It quantifies how to relate a signal $x[t]$ of length n input into the filter to its output $y[t]$ through the convolution of the input with the impulse response function:

$$y[t] = (x * h)[t] = \sum_{k=-\infty}^{\infty} x[k]h[t-k] \tag{C.1}$$

where $x[t]$ is taken to be zero for time values outside of its range. This expression takes on a simpler form in frequency space; because a convolution in the time domain corresponds to multiplication in the frequency domain, a frequency space input signal $X(f) = \mathcal{F}[x[t]]$ is related to its output $Y(f)$ through

$$Y(f) = H(f)X(f) \tag{C.2}$$

where $H(f) = \mathcal{F}[h[t]]$ is called the filter's transfer function. If we now combine the linearity of the expectation operator $E[\dots]$, the definition of the power spectral density, and the linearity of the filter, we find that the power spectral density of a time series $x[t]$ filtered with a filter with response function $h[t]$ is given by

$$S_Y(f) = H(f)^2 S_X(f) \tag{C.3}$$

The above tells us how to generate a digital time series $y[t]$ with arbitrary power spectral density $S(f) = A(f)$: we first generate white noise $x[t]$ with unit power spectral density $S(f) = 1$ by independently drawing from the Gaussian distribution with zero mean and unit standard deviation, which we then subsequently subject to the linear mapping of a filter with the transfer function $H(f) = \sqrt{A(f)}$ resulting in $S_Y(f) = A(f)$. Numerically this is done by convolving the white noise $x[t]$ with the impulse response function $h[t]$, which is generated from $\sqrt{A(f)}$ with Mathematica's *FrequencySamplingFilterKernel* function. This function creates a finite impulse response (FIR) filter using a frequency sampling method [74]. Note that the FIR is finite; the sharper the features of $A(f)$ the more values of $h[t]$ are required to produce them faithfully which increases computation time.

C.2 Digital to Analog Conversion

The digitally generated noise discussed above now has to be physically. This is done with an arbitrary waveform generator (AWG): the Tektronix AWG5014C. It is a device that converts the digital time series to an analog voltage signal with a sampling rate of up to 1.2 GSamples/s, where the sampling rate determines several properties of the output. For example the finite sampling rate determines the lowest frequency components contained in the output: the lowest frequency produced by the AWG is given by the sampling rate divided by the number of points n, which is the inverse of the time it takes the AWG to completely output the signal. The AWG5014C has a memory of 16 million points, which corresponds to a lower frequency cutoff of 75 Hz; components below this cutoff frequency will not be captured by output.

Conversely, the sampling rate of 1.2 GSamples/s implies a Nyquist frequency of 600 MHz, which is the highest frequency at which a digital to analog converter (DAC) can output a discrete-time signal before aliasing occurs [73]. It effectively serves as an upper cutoff of the frequency components that can be faithfully produced. While this upper end cutoff it is a feature that is present in any DAC, it can be undesirable in our experiments. We therefore always make sure that whatever power spectral density is used has a cutoff frequency $f_c < f_{Nyquist}$.

In addition to these cutoffs, the frequency response of the AWG is also not flat in the intermediate region as every DAC essentially attenuates the higher frequency components of the signal it produces. To understand the origin of the effect one can consider a simplified model of how a DAC operates. In general, the digital input of the DAC in the time domain is a train of impulses and the output of each of these impulses is set according to a so called zero-order hold: the DAC outputs a constant voltage during the update period given by the sampling rate. One can see this as a type of filter that is being applied to the digital input, with impulse response function $h(t)$ given by a square pulse. The transfer function can then be calculated to be given by $\mathrm{sinc}(\pi f/f_s) = \frac{\sin \pi f/f_s}{\pi f/f_s}$, which drops off with increasing frequency at a rate set by the sampling frequency f_s. It thus effectively attenuates the higher frequency components [73]. Note that this is a simplified picture of how a DAC operates; different implementations exist meaning that the exact form of the transfer function can be more complex.

For many applications such a drop off is not relevant as it occurs over relatively wide frequency ranges, but in the case of white noise it causes significant deviations from the wanted power spectral density and it needs to be compensated. We opt to do so using pre-equalizing. In this approach one treats the DAC as a black box type of filter with transfer function $G(f)$ that is applied to the input time series $x[n]$ upon conversion from digital to analog, so that

$$S_Y(f) = G(f)^2 S_X(f) \tag{C.4}$$

If one is able to quantify the transfer function, the time series can be preprocessed with the inverse filter $F(f) = \frac{1}{G(f)}$ to offset the effect up to an accuracy given by the quality of the quantification and the number of filter amplitudes used. In order to construct the inverse filter we input a signal with known spectral density $S_X(f)$ into the AWG, record the output spectral density $S_Y(f)$ with a spectrum analyzer, and calculate and invert $G(f)$. The mapping the AWG performs on the time series that had a power spectral density $S_X(f)$ prior to pre-processing can then be modeled as

$$S_Y(f) = G(f)^2 F(f)^2 S_X(f) = S_X(f) \tag{C.5}$$

This final step completes the recipe recipe for constructing voltage noise with an arbitrary power spectral density $S(f) = A(f)$. We first digitally generate a time series $x[t]$ of length n with unit power spectral density $S(f) = 1$ by independently drawing from a Gaussian distribution with zero mean and unit standard deviation. This time series is then filtered with two digital filters, with transfer functions $H(f) = \sqrt{A(f)}$ and $F(f) = \frac{1}{G(f)}$. It is then finally converted into an analog voltage signal by the AWG.

Bibliography

[1] G. D. Scholes, G. R. Fleming, A. Olaya-Castro, and R. van Grondelle, "Lessons from nature about solar light harvesting," *Nature Chemistry*, vol. 3, pp. 763–774, Sept. 2011.

[2] Interntional Energy Agency, *Key World Energy Statistics*. Paris: Interntional Energy Agency, 2016.

[3] N. S. Lewis and D. G. Nocera, "Powering the planet: Chemical challenges in solar energy utilization," *Proceedings of the National Academy of Sciences*, vol. 103, pp. 15729–15735, Oct. 2006.

[4] D. Gust, T. A. Moore, and A. L. Moore, "Mimicking Photosynthetic Solar Energy Transduction," *Accounts of Chemical Research*, vol. 34, pp. 40–48, Jan. 2001.

[5] R. E. Blankenship, *Molecular mechanisms of photosynthesis*. Chichester, West Sussex: Wiley/Blackwell, second edition ed., 2014.

[6] N. Lambert, Y.-N. Chen, Y.-C. Cheng, C.-M. Li, G.-Y. Chen, and F. Nori, "Quantum biology," *Nature Physics*, vol. 9, pp. 10–18, Dec. 2012.

[7] R. J. Cogdell, A. T. Gardiner, H. Hashimoto, and T. H. P. Brotosudarmo, "A comparative look at the first few milliseconds of the light reactions of photosynthesis," *Photochemical & Photobiological Sciences*, vol. 7, no. 10, p. 1150, 2008.

[8] J. F. Imhoff, "Biology of Green Sulfur Bacteria," in *eLS* (John Wiley & Sons Ltd, ed.), Chichester, UK: John Wiley & Sons, Ltd, June 2014.

[9] R. E. Fenna and B. W. Matthews, "Chlorophyll arrangement in a bacteriochlorophyll protein from Chlorobium limicola," *Nature*, vol. 258, pp. 573–577, Dec. 1975.

[10] F. Caruso, A. W. Chin, A. Datta, S. F. Huelga, and M. B. Plenio, “Highly efficient energy excitation transfer in light-harvesting complexes: The fundamental role of noise-assisted transport,” *The Journal of Chemical Physics*, vol. 131, no. 10, p. 105106, 2009.

[11] G. S. Engel, T. R. Calhoun, E. L. Read, T.-K. Ahn, T. Mančal, Y.-C. Cheng, R. E. Blankenship, and G. R. Fleming, “Evidence for wavelike energy transfer through quantum coherence in photosynthetic systems,” *Nature*, vol. 446, pp. 782–786, Apr. 2007.

[12] F. Muh, M. E.-A. Madjet, J. Adolphs, A. Abdurahman, B. Rabenstein, H. Ishikita, E.-W. Knapp, and T. Renger, “-Helices direct excitation energy flow in the Fenna Matthews Olson protein,” *Proceedings of the National Academy of Sciences*, vol. 104, pp. 16862–16867, Oct. 2007.

[13] M. Schmidt am Busch, F. Müh, M. El-Amine Madjet, and T. Renger, “The Eighth Bacteriochlorophyll Completes the Excitation Energy Funnel in the FMO Protein,” *The Journal of Physical Chemistry Letters*, vol. 2, pp. 93–98, Jan. 2011.

[14] F. Häse, S. Valleau, E. Pyzer-Knapp, and A. Aspuru-Guzik, “Machine learning exciton dynamics,” *Chem. Sci.*, vol. 7, no. 8, pp. 5139–5147, 2016.

[15] X. Jia, Y. Mei, J. Z. Zhang, and Y. Mo, “Hybrid QM/MM study of FMO complex with polarized protein-specific charge,” *Scientific Reports*, vol. 5, p. 17096, Nov. 2015.

[16] Y.-C. Cheng and G. R. Fleming, “Dynamics of Light Harvesting in Photosynthesis,” *Annual Review of Physical Chemistry*, vol. 60, pp. 241–262, May 2009.

[17] M. B. Plenio and S. F. Huelga, “Dephasing-assisted transport: quantum networks and biomolecules,” *New Journal of Physics*, vol. 10, p. 113019, Nov. 2008.

[18] M. Mohseni, P. Rebentrost, S. Lloyd, and A. Aspuru-Guzik, “Environment-assisted quantum walks in photosynthetic energy transfer,” *The Journal of Chemical Physics*, vol. 129, no. 17, p. 174106, 2008.

[19] M. Wendling, T. Pullerits, M. A. Przyjalgowski, S. I. E. Vulto, T. J. Aartsma, R. van Grondelle, and H. van Amerongen, “Electron−Vibrational Coupling in the Fenna−Matthews−Olson Complex of Prosthecochloris aestuarii Determined by Temperature-Dependent Absorption and Fluorescence Line-Narrowing Measurements,” *The Journal of Physical Chemistry B*, vol. 104, pp. 5825–5831, June 2000.

[20] S. Mostame, P. Rebentrost, A. Eisfeld, A. J. Kerman, D. I. Tsomokos, and A. Aspuru-Guzik, "Quantum simulator of an open quantum system using superconducting qubits: exciton transport in photosynthetic complexes," *New Journal of Physics*, vol. 14, p. 105013, Oct. 2012.

[21] J. Clarke and F. K. Wilhelm, "Superconducting quantum bits," *Nature*, vol. 453, pp. 1031–1042, June 2008.

[22] C. Olbrich, J. Strümpfer, K. Schulten, and U. Kleinekathöfer, "Quest for Spatially Correlated Fluctuations in the FMO Light-Harvesting Complex," *The Journal of Physical Chemistry B*, vol. 115, pp. 758–764, Feb. 2011.

[23] G. D. Mahan, *Many-particle physics*. Physics of solids and liquids, New York: Kluwer Academic/Plenum Publishers, 3rd ed ed., 2000.

[24] M. Göppl, A. Fragner, M. Baur, R. Bianchetti, S. Filipp, J. M. Fink, P. J. Leek, G. Puebla, L. Steffen, and A. Wallraff, "Coplanar waveguide resonators for circuit quantum electrodynamics," *J. Appl. Phys.*, vol. 104, p. 113904, Dec 2008.

[25] H. Haken and P. Reineker, "The coupled coherent and incoherent motion of excitons and its influence on the line shape of optical absorption," *Zeitschrift fur Physik*, vol. 249, pp. 253–268, June 1972.

[26] S. Shim, P. Rebentrost, S. Valleau, and A. Aspuru-Guzik, "Atomistic Study of the Long-Lived Quantum Coherences in the Fenna-Matthews-Olson Complex," *Biophysical Journal*, vol. 102, pp. 649–660, Feb. 2012.

[27] P. Rebentrost, M. Mohseni, I. Kassal, S. Lloyd, and A. Aspuru-Guzik, "Environment-assisted quantum transport," *New Journal of Physics*, vol. 11, p. 033003, Mar. 2009.

[28] M. O. Scully and M. S. Zubairy, *Quantum Optics*. Cambridge University Press, 1997.

[29] A. W. Chin, S. F. Huelga, and M. B. Plenio, "Coherence and decoherence in biological systems: principles of noise-assisted transport and the origin of long-lived coherences," *Philosophical Transactions of the Royal Society A: Mathematical, Physical and Engineering Sciences*, vol. 370, pp. 3638–3657, Aug. 2012.

[30] M. d. Rey, A. W. Chin, S. F. Huelga, and M. B. Plenio, "Exploiting Structured Environments for Efficient Energy Transfer: The Phonon Antenna Mechanism," *The Journal of Physical Chemistry Letters*, vol. 4, pp. 903–907, Mar. 2013.

[31] R. d. J. León-Montiel, M. A. Quiroz-Juárez, R. Quintero-Torres, J. L. Domínguez-Juárez, H. M. Moya-Cessa, J. P. Torres, and J. L. Aragón, "Noise-assisted energy transport in electrical oscillator networks with off-diagonal dynamical disorder," *Scientific Reports*, vol. 5, p. 17339, Nov. 2015.

[32] F. Caruso, A. Crespi, A. G. Ciriolo, F. Sciarrino, and R. Osellame, "Fast escape of a quantum walker from an integrated photonic maze," *Nature Communications*, vol. 7, p. 11682, June 2016.

[33] S. Viciani, M. Lima, M. Bellini, and F. Caruso, "Observation of Noise-Assisted Transport in an All-Optical Cavity-Based Network," *Physical Review Letters*, vol. 115, Aug. 2015.

[34] D. J. Griffiths, *Introduction to Quantum Mechanics*. New Jersey: Prentice Hall, 2nd ed ed., 2004.

[35] A. Wallraff, "Lecture notes on quantum systems for information technology," May 2016.

[36] M. Tinkham, *Introduction to Superconductivity*. New York: Dover Publications, 2nd ed ed., 2004.

[37] B. D. Josephson, "Possible new effects in superconductive tunnelling," *Physics Letters*, vol. 1, pp. 251–253, July 1962.

[38] S. Berger, *Geometric phases and noise in circuit QED*. PhD thesis, ETH Zurich, 2015.

[39] J. Koch, T. M. Yu, J. Gambetta, A. A. Houck, D. I. Schuster, J. Majer, A. Blais, M. H. Devoret, S. M. Girvin, and R. J. Schoelkopf, "Charge-insensitive qubit design derived from the Cooper pair box," *Phys. Rev. A*, vol. 76, no. 4, p. 042319, 2007.

[40] V. Bouchiat, D. Vion, P. Joyez, D. Esteve, and M. H. Devoret, "Quantum coherence with a single Cooper pair," *Phys. Scr.*, vol. T76, pp. 165–170, 1998.

[41] Y. Nakamura, Y. A. Pashkin, and J. S. Tsai, "Coherent control of macroscopic quantum states in a single-Cooper-pair box," *Nature*, vol. 398, pp. 786–788, Apr. 1999.

[42] D. Vion, A. Aassime, A. Cottet, P. Joyez, H. Pothier, C. Urbina, D. Esteve, and M. H. Devoret, "Manipulating the quantum state of an electrical circuit," *Science*, vol. 296, pp. 886–889, 2002.

[43] D. M. Pozar, *Microwave Engineering*. John Wiley & Sons, Inc., 4th ed. ed., 2011.

[44] B. K. Mitchell, "Nonclassical light in waveguide qed: Amplitude and intensity correlations," Master's thesis, ETH Zurich, 2016.

[45] L. S. Bishop, *Circuit Quantum Electrodynamics*. Michigan: Proquest, 1st ed ed., 2011.

[46] K. Lalumière, B. C. Sanders, A. F. van Loo, A. Fedorov, A. Wallraff, and A. Blais, "Input-output theory for waveguide qed with an ensemble of inhomogeneous atoms," *Phys. Rev. A*, vol. 88, p. 043806, Oct 2013.

[47] Y. Wu and X. Yang, "Strong-coupling theory of periodically driven two-level systems," *Physical Review Letters*, vol. 98, no. 1, 2007.

[48] A. Blais, R.-S. Huang, A. Wallraff, S. M. Girvin, and R. J. Schoelkopf, "Cavity quantum electrodynamics for superconducting electrical circuits: An architecture for quantum computation," *Phys. Rev. A*, vol. 69, pp. 062320–14, June 2004.

[49] E. Jaynes and F. Cummings, "Comparison of quantum and semiclassical radiation theories with application to the beam maser," *Proceedings of the IEEE*, vol. 51, no. 1, pp. 89–109, 1963.

[50] E. M. Purcell, "Spontaneous emission probabilties at radio frequencies," *Phys. Rev.*, vol. 69, p. 681, 1946.

[51] E. A. Sete, J. M. Gambetta, and A. N. Korotkov, "Purcell effect with microwave drive: suppression of qubit relaxation rate," *Phys. Rev. B*, vol. 89, p. 104516, 2014.

[52] A. van Loo, A. Fedorov, K. Lalumière, B. Sanders, A. Blais, and A. Wallraff, "Photon-mediated interactions between distant artificial atoms," *Science*, vol. 342, pp. 1494–1496, 12 2013.

[53] M. K. Tey, Z. Chen, S. A. Aljunid, B. Chng, F. Huber, G. Maslennikov, and C. Kurtsiefer, "Strong interaction between light and a single trapped atom without the need for a cavity," *Nat. Phys.*, vol. advanced online publication, pp. –, Oct. 2008.

[54] M. H. Devoret, "Quantum fluctuations in electrical circuits," in *Quantum Fluctuations: Les Houches Session LXIII* (S. Reynaud, E. Giacobino, and J. Zinn-Justin, eds.), pp. 351–386, Elsevier, 1997.

[55] O. Astafiev, A. M. Zagoskin, A. A. Abdumalikov Jr., Y. A. Pashkin, T. Yamamoto, K. Inomata, Y. Nakamura, and J. S. Tsai, "Resonance fluorescence of a single artificial atom," *Science*, vol. 327, no. 5967, pp. 840–843, 2010.

[56] J. Fink, *Quantum nonlinearities in strong coupling circuit QED*. PhD thesis, ETH Zurich, 10 2010.

[57] M. Göppl, *Engineering Quantum Electronic Chips - Realization and Characterization of Circuit Quantum Electrodynamics Systems*. PhD thesis, ETH Zurich, 05 2009.

[58] P. Welch, "The use of fast fourier transform for the estimation of power spectra: A method based on time averaging over short, modified periodograms," *IEEE Transactions on Audio and Electroacoustics*, vol. 15, no. 2, pp. 70–73, 1967.

[59] BlueFors, *BF-LD250 Cryogen Free Dilution Refrigerator System*.

[60] D. Bozyigit, C. Lang, L. Steffen, J. M. Fink, C. Eichler, M. Baur, R. Bianchetti, P. J. Leek, S. Filipp, A. Wallraff, M. P. da Silva, and A. Blais, "Correlation measurements of individual microwave photons emitted from a symmetric cavity," *J. Phys.: Conf. Ser.*, vol. 264, no. 1, pp. 012024–8, 2011.

[61] C. Lang, *Quantum Microwave Radiation and its Interference Characterized by Correlation Function Measurements in Circuit Quantum Electrodynamics*. PhD thesis, ETH Zurich, 02 2014.

[62] M. S. Khalil, M. J. A. Stoutimore, F. C. Wellstood, and K. D. Osborn, "An analysis method for asymmetric resonator transmission applied to superconducting devices," *J. Appl. Phys.*, vol. 111, no. 5, p. 054510, 2012.

[63] S. Gasparinetti. Personal Communication. 2016-08-04.

[64] M. Mitchison, "Pure dephasing γ_ϕ in a master equation and noise power spectral densities." `http://physics.stackexchange.com/q/282909`.

[65] M. Pelagatti, "Lecture notes on stationary processes," October 2013.

[66] P. J. Brockwell and R. A. Davis, *Introduction to Time Series and Forecasting*. New York: Springer, 2nd ed ed., 2002.

[67] J. M. Martinis, S. Nam, J. Aumentado, K. Lang, and U. C., "Decoherence of a superconducting qubit due to bias noise," *Phys. Rev. B*, vol. 67, p. (9):094510, 2003.

[68] A. Stuart and K. Ord, *Kendall's Advanced Theory of Statistics, Distribution Theory*. Chichester, West Sussex: Wiley, volume 1 edition ed., Feb. 2010.

[69] M. Mitchison, "Classical approximation of coupling to a quantum bath." `http://physics.stackexchange.com/q/283981`.

[70] W. Magnus, "On the exponential solution of differential equations for a linear operator," *Communications on Pure and Applied Mathematics*, vol. 7, pp. 649–673, Nov. 1954.

[71] S. O. Rice, "Mathematical analysis of random noise," *Bell System Technical Journal*, vol. 23, no. 23, pp. 282–332, 1944.

[72] R. V. Hogg and E. Tanis, *Probability and Statistical Inference*. London: Pearson, 8th ed ed., 2009.

[73] R. G. Lyons, *Understanding Digital Signal Processing*. New Jersey: Prentice Hall, 3rd ed ed., 2010.

[74] "Frequency Sampling Filter Kernel Documentation." `https://reference.wolfram.com/language/ref/FrequencySamplingFilterKernel.html`. Accessed: 2016-09-02.

Eidgenössische Technische Hochschule Zürich
Swiss Federal Institute of Technology Zurich

Declaration of originality

The signed declaration of originality is a component of every semester paper, Bachelor's thesis, Master's thesis and any other degree paper undertaken during the course of studies, including the respective electronic versions.

Lecturers may also require a declaration of originality for other written papers compiled for their courses.

I hereby confirm that I am the sole author of the written work here enclosed and that I have compiled it in my own words. Parts excepted are corrections of form and content by the supervisor.

Title of work (in block letters):

Analog Quantum Simulation of Noise Assisted Transport in Light Harvesting Structures using Superconducting Circuits

Authored by (in block letters):
For papers written by groups the names of all authors are required.

Name(s):	**First name(s):**
Bargerbos	Arno

With my signature I confirm that

- I have committed none of the forms of plagiarism described in the 'Citation etiquette' information sheet.
- I have documented all methods, data and processes truthfully.
- I have not manipulated any data.
- I have mentioned all persons who were significant facilitators of the work.

I am aware that the work may be screened electronically for plagiarism.

Place, date	**Signature(s)**
Zürich, 06-10-2016	Arno Bargerbos

For papers written by groups the names of all authors are required. Their signatures collectively guarantee the entire content of the written paper.